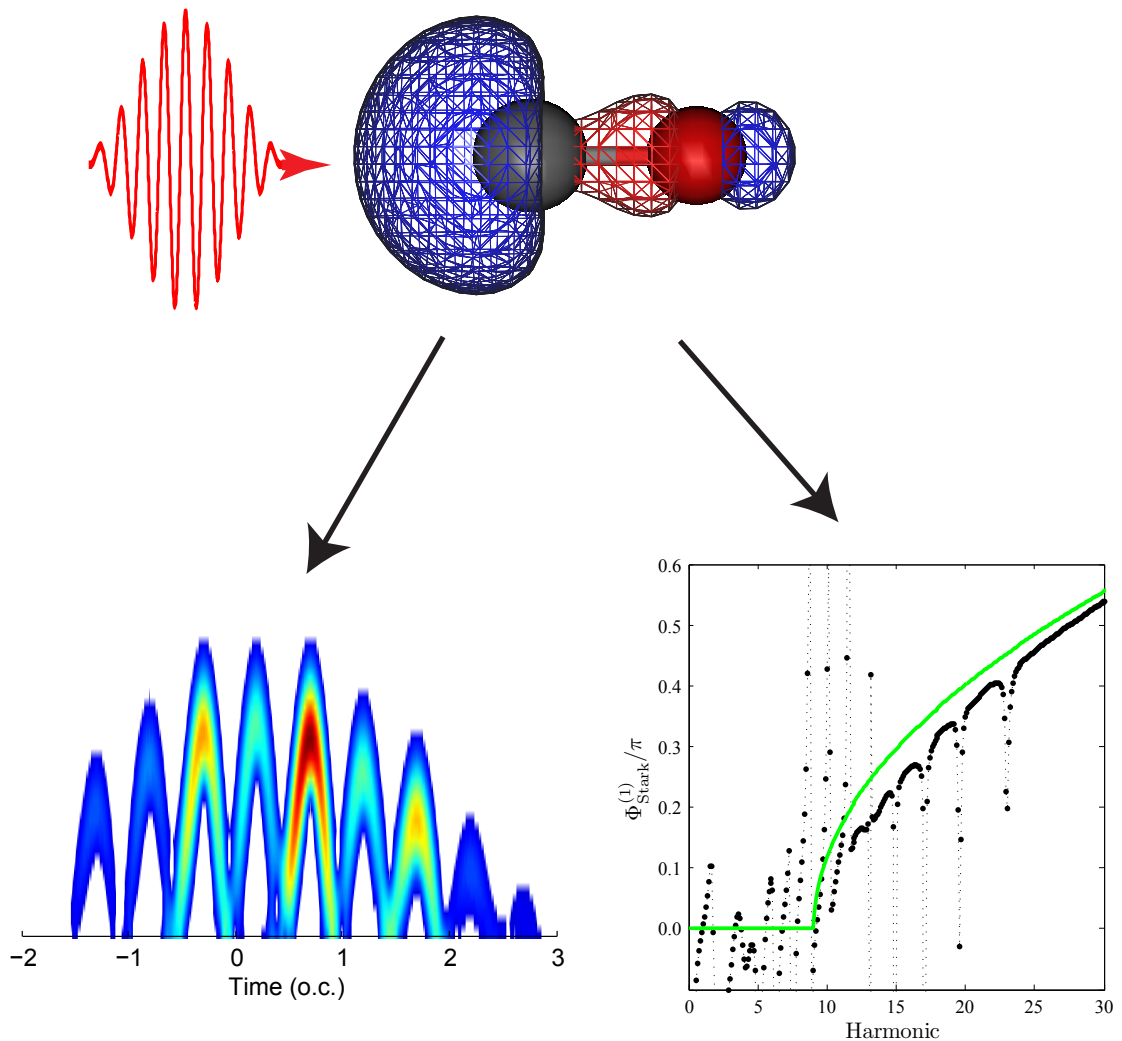


High-order harmonic generation from polar molecules

Adam Etches



AARHUS
UNIVERSITY

DEPARTMENT OF PHYSICS
AND ASTRONOMY

Lundbeck Foundation
Theoretical
Center for
Quantum
System Research

High-order harmonic generation from polar molecules

Adam Etches

...

PhD thesis

Department of Physics and Astronomy
Aarhus University
10th July 2012.

This thesis is submitted to Science and Technology at Aarhus University, Denmark, in order to fulfill the requirements for obtaining the PhD degree in physics. The studies have been carried out under the supervision of Lars Bojer Madsen at the Department of Physics and Astronomy.



Contents

Preface	iv
List of publications	vii
1 Introduction	1
1.1 Motivation	1
1.2 Current state of the field	2
1.3 Thesis outline	5
2 The Lewenstein model	7
2.1 Derivation	8
2.2 Orientation and alignment	13
2.3 The multi-centre stationary-phase method	15
2.4 Short-comings of the Lewenstein model	18
3 Ellipticity of high-harmonics	20
3.1 Ellipticity within the Lewenstein model	21
3.2 Comparison with other models	27

Contents

4	Influence of polar orbitals	31
4.1	Emission times	31
4.2	Odd and even harmonics	36
5	Including Stark shifts	39
5.1	Derivation	40
5.2	Impact on emission times	43
5.3	Stark phases	46
6	Two-centre interference	57
6.1	Basic concepts	58
6.2	Oriented polar molecules	62
6.3	Aligned polar molecules	65
6.4	Importance of Stark phases	71
7	Macroscopic phase-matching	76
7.1	Propagation equations	76
7.2	Phase-matching	79
7.3	Phase-matching for polar molecules	82
7.4	Robustness of Stark phases	84
8	Summary and outlook	90
8.1	Summary	91
8.2	Outlook	94
	Published papers	97
A	Inducing elliptically polarized high-order harmonics from aligned molecules with linearly polarized femtosecond pulses	97
B	Extending the strong-field approximation of high-order harmonic generation to polar molecules: gating mechanisms and extension of the harmonic cutoff	104
C	Two-center minima in harmonic spectra from aligned polar molecules	113
D	Laser-induced bound-state phases in high-order harmonic generation	121

Contents

Bibliography

127



Preface

This thesis summarises work I have done during my PhD studies at the Department of Physics and Astronomy, Aarhus University, Denmark, under the supervision of Lars Bojer Madsen. The main topic is high-order harmonic generation from molecules, with a focus on the modifications that are necessary to describe polar molecules.

Units and abbreviations

Most equations are in atomic units, where the reduced Planck's constant, \hbar , the elementary charge, e , the electron mass, m_e , and the Bohr radius, a_0 , are all equal to one. To conform with the literature, the equations on macroscopic phase-matching in chapter 7 are kept in SI units. Abbreviations that are used in this thesis are listed below:

as attosecond

au atomic units

HHG high-order harmonic generation
HOMO highest occupied molecular orbital
LCAO linear combination of atomic orbitals
QRS quantitative rescattering model
SFA strong-field approximation
TDSE time-dependent Schrödinger equation
XUV extreme ultraviolet

Acknowledgements

First of all I would like to thank my supervisor, Lars Bojer Madsen. I am grateful for his tolerance of my (many) extracurricular activities over the past four years as well as his human touch, which has helped me back on track when it all felt a bit overwhelming.

I would also like to thank Mette Gaarde, who supervised me during my research stay at the Department of Physics & Astronomy, Louisiana State University, USA. I learnt a lot from our collaboration, and appreciate all the practical help that made my stay possible. The same goes to Ken Schafer, who provided much needed distraction during lengthy debugging sessions.

I was very fortunate to work together with Christian Bruun Madsen during the first years of my PhD, and would like to thank him for easing my way into the mysteries of high-order harmonic generation, as well as the template for this thesis. Mahmoud Abu-Samha and Darko Dimitrovski have both given me technical assistance whenever I needed it, and Maciej Spiewanowski has developed a new filter for the selection of short trajectories.

A big thanks to some of my fellow PhD students, who I have had the great pleasure of sharing an office (or at least a supervisor) with: Jan Conrad Baggesen, Henriette Astrup Leth, and

Preface

Christian Per Juul Martiny. Their wonderful company as well as help in everything ranging from Linux commands to the merits of the SFA over ADK rates is much appreciated. Special thanks to Henriette, who graciously disclosed some of the style secrets from her thesis.

Finally, my eight years at Aarhus University would not have been the same without its rich and varied student life. I would like to acknowledge the following groups and organizations for providing me with the opportunity to delve into everything ranging from student politics to bartending: Mat/Fys-Tutorgruppen, Parkkollegierne, TAAGEKAMMERET, Mat/Fys StudenterRåd (MFSR), Fysisk Fredagsbar, and PHAUST (the PhD Association at Aarhus University, Science and Technology).



List of publications

I have published three papers as part of my PhD studies, and a fourth paper has been submitted for review. The contents of all four serve as a part of this thesis, and several passages as well as figures have been adapted from them. For ease of reference, the papers are included as appendices A–D, though they should not be considered a direct part of this thesis.

- A) Adam Etches, Christian Bruun Madsen, and Lars Bojer Madsen, *Inducing elliptically polarized high-order harmonics from aligned molecules with linearly polarized femtosecond pulses*, Physical Review A **81**, 013409 (2010)
- B) Adam Etches, and Lars Bojer Madsen, *Extending the strong-field approximation of high-order harmonic generation to polar molecules: gating mechanisms and extension of the harmonic cutoff*, Journal of Physics B: Atomic, Molecular and Optical Physics **43**, 155602 (2010)
- C) Adam Etches, Mette B. Gaarde, and Lars Bojer Madsen, *Two-center minima in harmonic spectra from aligned polar molecules*, Physical Review A **84**, 023418 (2011)

List of publications

- D) Adam Etches, Mette B. Gaarde, and Lars Bojer Madsen,
*Laser-induced bound-state phases in high-order harmonic
generation*, arXiv:1206.2104v1

Introduction

In this chapter we will give a short introduction to strong-field physics, and motivate the need for new models of high-order harmonic generation. The last section contains an outline of this thesis, putting each chapter into a larger perspective.

1.1 Motivation

Atomic, molecular and optical physics is a very active branch of modern physics. One of its main goals is to improve our understanding of how light and matter interact. At low intensities, light-matter interaction is conveniently described in terms of transitions between discrete energy levels. At the highest intensities, targets get stripped of all their electrons, and we enter the realm of plasma physics where the bound levels play a negligible role. At intermediate intensities of $\sim 10^{13}$ – 10^{16} W/cm² we find the (poorly named) strong-field regime.

In strong-field physics the probing laser exerts a force on the most loosely bound electron, which is comparable in magnitude to that of the confining Coulomb potential. The competition

between these two forces gives rise to several emergent phenomena. A prominent example is the emission of high-frequency light from a gas of atoms or molecules when submitted to a strong infrared laser field [1, 2]. If the driving pulse contains several optical cycles, the spectrum of the emitted light consists of a series of peaks placed at integer multiples of the photon energy of the driving laser. The first few harmonics behave as expected from perturbation theory, in that the intensity of each harmonic is considerably lower than that of the preceding one. However, this behaviour is succeeded by a plateau of harmonics with equal intensities followed by a sharp cutoff. For this reason, the process is known as high-order harmonic generation (HHG). Depending on the target gas and the driving laser, the plateau can contain more than a hundred harmonics, and reach into the extreme ultraviolet (XUV) or even X-ray frequency range [3–5].

The high harmonics have properties that make them promising for applications. Most importantly, they are emitted as a coherent beam that co-propagates with the generating laser [1]. This makes HHG a candidate for an “XUV laser”. The temporal characteristics of the harmonics are also interesting. It turns out that the harmonics are emitted in sub-femtosecond bunches [6]. Using few-cycle drivers, the high-harmonic spectrum becomes continuous, and supports single harmonic bursts as short as 80 as [7, 8] (1 as = 1×10^{-18} s). This is comparable to the atomic unit of time (1 au = 24 as), and smaller than the Bohr orbit time of the electron in hydrogen (150 as). The hope is that HHG and other strong-field phenomena can be used to probe electron dynamics in atomic, molecular and solid state systems on their natural time scales [9].

1.2 Current state of the field

Unfortunately, the HHG conversion efficiency is very low. Traditionally the main goal of HHG research has been to increase the intensity of the generated harmonics, either in the generation pro-

cess [3–5], or through amplification in free-electron lasers [10, 11]. Recent years have seen an increased focus on the detailed structure of the harmonic spectrum itself, and the information that it contains about the target and the strong-field induced electron dynamics [12–14]. As no other method can be used monitor the dynamics leading to high-harmonics, this is done by comparing experimental data and theoretical predictions.

It is very difficult to calculate HHG spectra using the time-dependent Schrödinger equation (TDSE) directly. Titanium-sapphire lasers, the work horse of strong-field physics, typically operate around 800 nm, which corresponds to an optical cycle of 110 au. For typical pulse durations, this means that the TDSE has to be propagated for thousands of atomic units. This would not be a problem if only a few discrete states were populated, but the driving lasers that cause HHG are all strong enough to promote significant population into the electronic continuum. Add to this the curse of dimensionality, and you find that *ab initio* HHG spectra can only be calculated for atomic hydrogen or H_2^+ .

When trying to model HHG instead, the first step is to disentangle the dynamics into parts that depend only on the binding potential or the driving field. This line of enquiry is inspired by the now famous three-step model [15, 16], which is sketched in figure 1.1. The idea of the three-step model is to treat the least bound electron semi-classically: Initially, the electron is bound by the combined Coulomb potential of the nucleus and the other electrons. The interaction with the driving laser serves to lower the potential barrier at the peak of each optical half-cycle. If the intensity is high enough, the electron may tunnel through the barrier, and into the continuum. This is known as step one. Once in the continuum, the electron is treated as a classical particle, and its interaction with the Coulomb potential is ignored. The laser field accelerates the electron away from the parent ion, and back again when the electric field changes its sign in the following half-cycle. By the time the electron returns to the core, it will have gained a significant amount of kinetic energy from the driving laser. This is step two. In step three, the electron recombines

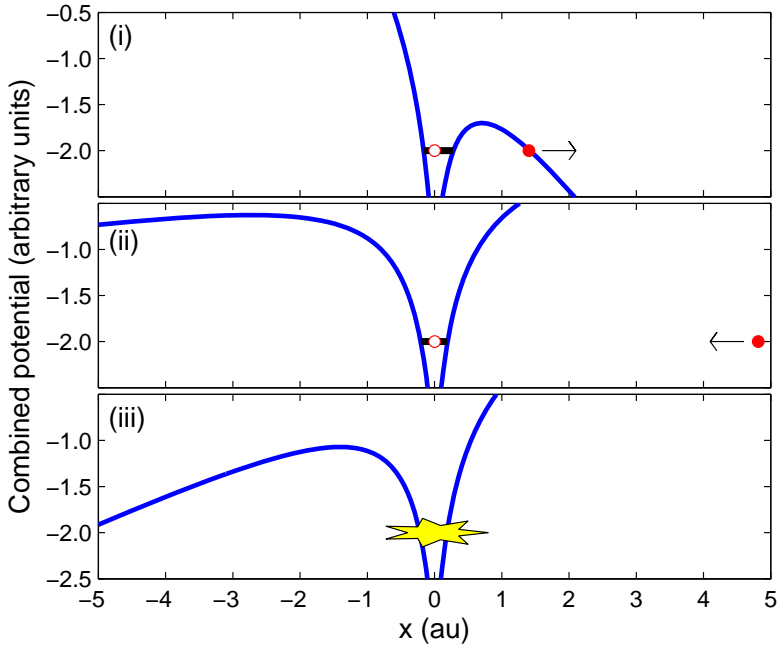


Figure 1.1 | Sketch of the three-step model of HHG. The blue line is the combined Coulomb and laser potential, and the red dot represents the x coordinate of the least bound electron. (i) The electron tunnels away from the nucleus. (ii) The freed electron is accelerated out and back again by the laser field. (iii) The electron recombines, and emits its excess kinetic energy as a high-energy photon.

into the ground state, and emits its excess kinetic energy as a high-energy photon.

The Lewenstein model is the quantum mechanical analogue of the three-step model [17]. It has been hugely successful in describing HHG from atoms, and has also been extended to cover molecular targets. However, experiments have begun uncovering effects that cannot be understood within the Lewenstein model. If we truly hope to use HHG as a probe of ultra fast dynamics, then theory has to be developed that not only reproduces experimental data, but also uncovers the physical mechanisms behind

them.

My main contribution to the field is theoretical modelling of HHG from polar molecules. Polar molecules are particularly challenging to theory because of their large dipole interaction with the driving laser. We include this interaction to lowest order by adiabatically Stark-shifting the bound state energies according to the instantaneous value of the laser field. While such a simplistic model cannot be expected to describe the full dynamics, it does allow us to study some of the unique features of polar molecules, and provides a reference point for the development of new, more sophisticated models.

1.3 Thesis outline

Here follows a brief outline of each chapter:

Chapter 2 reviews the Lewenstein model, providing the background for our extension to polar molecules. Proper implementation of the stationary-phase method for molecules is also discussed.

Chapter 3 shows that the Lewenstein model supports the generation of elliptically polarized harmonics from aligned molecules using linearly polarized driving pulses.

Chapter 4 discusses how nonsymmetric orbitals affect emission times of the emitted harmonics as well as the spectral content of the harmonic spectrum.

Chapter 5 presents a way to include Stark shifts in the Lewenstein model. The impact on emission times and harmonic phases is discussed.

Chapter 6 reviews the two-centre interference model for homonuclear molecules, and extends it to polar molecules. The relation between interference minima from oriented and

Chapter 1. Introduction

aligned polar molecules is analyzed, and the impact of Stark shifts discussed.

Chapter 7 deals with phase-matching in a macroscopic gas of molecules. Propagation equations are reviewed, and the impact of Stark shifts discussed. The laser-induced Stark phase is shown to survive phase-matching.

Chapter 8 summarizes the main results, and provides a brief outlook.

The Lewenstein model

The Lewenstein model is the quantum version of the three-step model. It can be derived from the strong-field approximation (SFA), which formalizes the intuitive steps of the three-step model. The Lewenstein model has been hugely successful. It is simple to understand, and very cheap to evaluate compared to solving the TDSE. This makes the Lewenstein model ideal as a point of departure for testing the influence of new physical effects in HHG. The main contribution of this thesis is to extend the Lewenstein model to polar molecules by including the time-dependent Stark shift felt by each molecular orbital due to the driving field.

In this chapter we will review derivations of the SFA and the Lewenstein model. We then review the multi-centre stationary-phase method, which bridges the gap between a quantum and a semi-classical understanding of HHG from molecules. We end the chapter with a discussion of some of the problems with the Lewenstein model, and a brief overview of research directions attempting to repair its failings.

2.1 Derivation

A full description of HHG requires modelling on two levels. First, the microscopic response of a single molecule to a strong driving field must be solved using the TDSE or a simplified model. Second, the coherent build-up of harmonics in the macroscopic target gas must be described using Maxwell's wave equation with the single-molecule dipole response as a source term [18, 19]. The interplay between the microscopic and macroscopic response complicates the analysis greatly, so we restrict ourselves to the single-molecule response in most of this thesis. We shall return to a discussion of macroscopic effects in chapter 7.

In the limiting case of an infinitely thin gas the full macroscopic spectrum is most closely resembled by the single-molecule dipole velocity spectrum [20]. In the following, we therefore assume that the spectrum of the harmonic component along $\hat{\mathbf{n}}$ is given by

$$S_{\hat{\mathbf{n}}}(\omega) = \left| \hat{\mathbf{n}} \cdot \int_{-\infty}^{\infty} e^{i\omega t} \frac{d}{dt} \langle \hat{\mathbf{d}}_{\text{dip}}(t) \rangle dt \right|^2 \quad (2.1)$$

$$= \left| \hat{\mathbf{n}} \cdot \int_{-\infty}^{\infty} e^{i\omega t} \langle \hat{\mathbf{v}}_{\text{dip}}(t) \rangle dt \right|^2, \quad (2.2)$$

where $\hat{\mathbf{d}}_{\text{dip}} = -\mathbf{r}$ is the dipole operator, and $\hat{\mathbf{v}}_{\text{dip}} = -i\nabla$ the dipole velocity operator. In the single-active electron approximation one assumes that the electrons do not interact during the interaction with the laser pulse. The active electron is expressed as a Slater determinant of occupied states, and the full expectation value splits into a sum over single orbital expectation values [21]

$$\langle \hat{\mathbf{v}}_{\text{dip}}(t) \rangle = \sum_{i=1}^{\infty} P_i \langle \psi_i(t) | \hat{\mathbf{v}}_{\text{dip}} | \psi_i(t) \rangle. \quad (2.3)$$

Derivation

The orbital weights fulfill the normalization condition

$$\sum_{i=1}^{\infty} P_i = 1. \quad (2.4)$$

The single-active electron approximation allows each orbital contribution to be calculated separately in the effective potential $V(\mathbf{r})$ formed by the nuclei and the other (static) electrons.

The Hamiltonian for an electron in a potential \hat{H}_L subject to an electric field $\mathbf{F}(t)$ is

$$\hat{H} = \hat{H}_0 + V_L(t) \quad (2.5)$$

$$= \hat{H}_L + V(\mathbf{r}), \quad (2.6)$$

where

$$\hat{H}_0 = -\frac{1}{2}\nabla^2 + V(\mathbf{r}) \quad (2.7)$$

$$\hat{H}_L = -\frac{1}{2}\nabla^2 + V_L(t) \quad (2.8)$$

$$V_L(t) = -\mathbf{F}(t) \cdot \mathbf{r}. \quad (2.9)$$

While it is difficult to solve the full (time-dependent) Schrödinger equation, \hat{H}_0 has eigenstates $|\psi_i^{(0)}(t)\rangle$ that can be easily found using quantum chemistry codes [22]. The eigenstates of \hat{H}_L are the so-called Volkov waves:

$$\psi_{\mathbf{k}}(\mathbf{r}, t) = \langle \mathbf{r} | \mathbf{k}(t) \rangle \quad (2.10)$$

$$= (2\pi)^{-3/2} \exp\left(i\left[\mathbf{k} + \mathbf{A}(t)\right] \cdot \mathbf{r} - \int_{t_0}^t \frac{1}{2} (\mathbf{k} + \mathbf{A}(t'))^2 dt'\right), \quad (2.11)$$

where $\mathbf{A}(t)$ is a vector potential for the electric field $\mathbf{F}(t) = -\partial_t \mathbf{A}(t)$. The corresponding time-evolution operators are

$$\mathcal{U}_0(t, t_0) = \sum_{i=1}^{\infty} \left| \psi_i^{(0)}(t) \right\rangle \left\langle \psi_i^{(0)}(t_0) \right| \quad (2.12)$$

$$\mathcal{U}_{\text{vol}}(t, t_0) = \int_{\mathbb{R}^3} d\mathbf{k} |\mathbf{k}(t)\rangle \langle \mathbf{k}(t_0)|. \quad (2.13)$$

This gives rise to two equivalent Dyson series for the time-evolution operator of the full Hamiltonian:

$$\mathcal{U}(t, t_0) = \mathcal{U}_0(t, t_0) - i \int_{t_0}^t dt' \mathcal{U}(t, t') V_L(t') \mathcal{U}_0(t', t_0) \quad (2.14)$$

$$\mathcal{U}(t, t_0) = \mathcal{U}_{\text{vol}}(t, t_0) - i \int_{t_0}^t dt' \mathcal{U}(t, t') V \mathcal{U}_{\text{vol}}(t', t_0). \quad (2.15)$$

The physics of the two Dyson series is easily understood if they are applied to an electron in a bound state or a Volkov state respectively. The first equation then describes field-free time-evolution followed by a dressing by the electric field. The second equation describes the Coulomb dressing of a Volkov state. The SFA is obtained by inserting equation (2.15) into (2.14), and keeping only the two lowest-order terms:

$$\mathcal{U}(t, t_0) \approx \mathcal{U}_0(t, t_0) - i \int_{t_0}^t dt' \mathcal{U}_{\text{vol}}(t, t') V_L(t') \mathcal{U}_0(t', t_0). \quad (2.16)$$

Applying the approximate time-evolution operator to an initial field-free state then gives the SFA wave function

$$\begin{aligned} |\psi_i(t)\rangle &\approx |\psi_i^{(0)}(t)\rangle \\ &- i \int_{t_0}^t dt' \int_{\mathbb{R}^3} d\mathbf{k} |\mathbf{k}(t)\rangle \langle \mathbf{k}(t') | V_L(t') | \psi_i^{(0)}(t') \rangle \end{aligned} \quad (2.17)$$

We now obtain the Lewenstein model by using the SFA wave function in equation (2.17) to evaluate the time-dependent dipole velocity. In calculating the expectation value, we throw away

Derivation

terms that contain matrix elements between continuum states:

$$\begin{aligned} \langle \psi_i(t) | \hat{\mathbf{v}}_{\text{dip}} | \psi_i(t) \rangle &\approx -i \int_{t_0}^t dt' \int_{\mathbb{R}^3} d\mathbf{k} \langle \psi_i^{(0)}(t) | \hat{\mathbf{v}}_{\text{dip}} | \mathbf{k}(t) \rangle \\ &\times \langle \mathbf{k}(t') | V_L(t') | \psi_i^{(0)}(t') \rangle \quad (2.18) \\ &+ \text{complex conjugate} \end{aligned}$$

$$\begin{aligned} &= i \int_{t_0}^t dt' \int_{\mathbb{R}^3} d\mathbf{k} \mathbf{v}_{\text{rec}}^*(\mathbf{k} + \mathbf{A}(t)) e^{-iS(\mathbf{k}, t, t')} \\ &\times \mathbf{F}(t') \cdot \mathbf{d}_{\text{ion}}(\mathbf{k} + \mathbf{A}(t')) \quad (2.19) \\ &+ \text{complex conjugate.} \end{aligned}$$

This is justified because of the small matrix elements between continuum states. The terms in equation (2.19) relate directly to the Fourier transform of the bound state $\tilde{\psi}$:

$$\mathbf{d}_{\text{ion}}(\mathbf{k} + \mathbf{A}(t')) = i \nabla_{\mathbf{k} + \mathbf{A}(t')} \tilde{\psi}_i(\mathbf{k} + \mathbf{A}(t')) \quad (2.20)$$

$$S(\mathbf{k}, t, t') = \int_{t'}^t \left(\frac{1}{2} [\mathbf{k} + \mathbf{A}(t'')]^2 - E_0 \right) dt'' \quad (2.21)$$

$$\mathbf{v}_{\text{rec}}(\mathbf{k} + \mathbf{A}(t)) = [\mathbf{k} + \mathbf{A}(t)] \tilde{\psi}_i(\mathbf{k} + \mathbf{A}(t)). \quad (2.22)$$

The term $\mathbf{F}(t') \cdot \mathbf{d}_{\text{ion}}(\mathbf{k} + \mathbf{A}(t'))$ is naturally interpreted as ionization from the ground state into the continuum at the time t' . The semi-classical phase $S(\mathbf{k}, t, t')$ accounts for propagation in the strong laser field. Finally, $\mathbf{v}_{\text{rec}}(\mathbf{k} + \mathbf{A}(t))$ is the recombination matrix element back into the bound state at time t . The Lewenstein model thus immediately relates to the three-step model.

Using Gaussian basis states, all matrix elements have analytical expressions, which considerably speeds up calculations. We obtain our molecular orbitals using the standard quantum chemistry software GAMESS, supplemented by data from the NIST Computational Chemistry Comparison and Benchmark DataBase (<http://cccbdb.nist.gov/>). First the nuclei are frozen in their equilibrium positions, and the nuclei placed such that the centre of mass is located at the origin. Orbitals are then calculated in a

triple zeta valence basis set with additional diffuse s and p orbitals. All orbital energies E_i are then shifted such that the energy of the highest occupied molecular orbital (HOMO) is equal to minus the experimentally determined vertical ionization potential I_p . In the case of N_2 , GAMESS wrongly predicts that the HOMO has π symmetry. We instead choose the highest occupied σ orbital. We will not present calculations that include the HOMO–1 channel in N_2 , so the true energy spacing does not become an issue.

The influence of lower-lying occupied bound states and higher-lying resonances on the harmonic spectrum is a topic of much debate [23–31]. All occupied molecular orbitals are included in equation (2.3), but excited states and channel couplings are completely ignored. Depending on their symmetries, and the geometry of the driving field, typically only the HOMO, HOMO–1 and HOMO–2 contribute. This is due to the initial tunnel ionization step, which is exponentially sensitive to the ionization potential [32]. It would be most consistent to always include all occupied molecular orbitals, but the focus of this thesis is on the peculiarities of polar orbitals. We therefore mostly restrict ourselves to the HOMO contribution, and refer to the HOMO as the ground state $|\psi\rangle$.

Another simplification we make is to limit the dt' integral in equation (2.19) to the interval $[t - T, t]$. This blocks out all but the two dominating trajectories (commonly referred to as the *short* and *long* trajectories) as well as speeding up calculations. Other effects that influence the final harmonic spectrum are nuclear vibration [33], and the orientational distribution of the target molecule [21, 34]. We will completely ignore nuclear vibration, which reduces the harmonic intensity by the square modulus of the nuclear autocorrelation function [33, 35, 36]. This forms the basis of the PACER (probing attosecond dynamics by chirp encoded recollision) technique, which has been used to measure proton rearrangement in H_4 [37], and H_2 [38].

Two competing effects determine the importance of nuclear vibration: the width of the nuclear wave function, and the char-

characteristic vibration time. Light nuclei vibrate faster, so as a rule of thumb only HHG from light isotopes is significantly influenced by nuclear vibration. However, the narrower width of the nuclear wave function of heavy nuclei partially compensates for this [36], so even HHG from heavy isotopes is influenced if the Born-Oppenheimer potential of the cation is sufficiently far from that of the neutral molecule. This has recently been shown to be the case for the HOMO-1 channel of N_2 [24].

2.2 Orientation and alignment

Unlike atoms, molecules are not rotationally symmetric, and their response to a probing laser pulse depends on the orientation of the molecule with respect to the laboratory frame. In this thesis we only consider linearly polarized driving lasers. We fix the laboratory frame such that the laser pulse is linearly polarized in the x direction, and propagates in the z direction. We can then define the orientation of the target molecule in terms of Euler angles (φ, θ, χ) .

The orientation of a linear target molecule relates to the Euler angles as following: First the molecule is oriented with its internuclear axis along the z axis in the molecular frame. If the molecule is polar, a choice must be made regarding the up/down asymmetry. The molecular frame is then placed such that it coincides with the laboratory frame. The molecular frame is rotated by an angle of φ around its internuclear (z) axis. The new molecular frame is subsequently rotated by an angle of θ around its y axis, and finally by χ around the resulting internuclear (z) axis.

The correct way of treating orientational distributions in HHG is to coherently add the harmonic emission from each orientation. Given an orientational distribution $G(\varphi, \theta, \chi)$, the total harmonic

spectrum is given by the Fourier transform of [21, 34]

$$\begin{aligned} \langle \hat{\mathbf{v}}_{\text{dip}}(t) \rangle &= \int_0^{2\pi} d\varphi \int_0^\pi d\theta \int_0^{2\pi} d\chi G(\varphi, \theta, \chi) \\ &\quad \times \sin(\theta) \langle \hat{\mathbf{v}}_{\text{dip}}(\varphi, \theta, \chi; t) \rangle. \end{aligned} \quad (2.23)$$

The field-free Hamiltonian \hat{H}_0 is invariant under rotations, so the natural state of a molecule is an equal superposition of all orientations. In the language of equation (2.23), the molecular response must be calculated for all orientations, and the results added coherently with the weight $G(\varphi, \theta, \chi) \equiv 1/(4\pi^3)$. Such a procedure requires many single-molecule calculations, and therefore becomes very time consuming. More importantly, it effectively washes out spectral features relating to electron dynamics at a particular orientation angle. Fortunately, some degree of orientation can be experimentally obtained [39].

In this thesis we will make a sharp distinction between molecular *orientation*, and molecular *alignment*. A perfectly aligned molecule has its internuclear axis completely fixed in the laboratory frame. If the molecule is symmetric, such as N_2 , O_2 and CO_2 , this corresponds to the maximal amount of control. If the target molecule is not symmetric, as in the case of CO , then perfect alignment corresponds to a coherent superposition of pointing “up” and “down” or “left” and “right”, etc. Only if the up/down asymmetry is broken do we refer to a molecule as being oriented.

The typical way of partially aligning a gas of molecules is to submit it to a moderately intense ($\sim 10^{13}$ W/cm²) infrared pulse. This populates a range of rotational energy levels. The subsequent field-free time-evolution leads to periodic phasing and dephasing, corresponding to alignment and anti-alignment. The achievable degree of alignment is not as high as for static-field or adiabatic laser alignment methods, but has the great advantage that the target molecule can be studied under field-free conditions.

Orienting molecules is more difficult, especially under field-free conditions. The best level of orientation is obtained using

quantum-state selected gases [40–44], but the resulting densities are fairly low. High-order harmonic generation has a low cross section, and spectrometers do not have very high sensitivity in the XUV range, so there are very few HHG experiments on oriented polar molecules. Alternative methods of accessing the molecular frame include partial orientation by two-colour pulses [45], and post-selection methods like COLTRIMS (cold target recoil-ion momentum spectroscopy) [46].

Despite current experimental limitations, we will only consider two idealized orientational distributions: perfectly oriented, and perfectly aligned. This makes direct comparison with experiments more difficult, but has the advantage of reducing the complexity, allowing us to focus on the unique aspects of HHG from polar molecules. In the oriented case, equation (2.23) simplifies to

$$\langle \hat{\mathbf{v}}_{\text{dip}}(t) \rangle = \langle \hat{\mathbf{v}}_{\text{dip}}(\varphi, \theta, \chi; t) \rangle, \quad (2.24)$$

and in the aligned case to

$$\langle \hat{\mathbf{v}}_{\text{dip}}(t) \rangle = \frac{1}{2} \langle \hat{\mathbf{v}}_{\text{dip}}(\varphi, \theta, \chi; t) \rangle + \frac{1}{2} \langle \hat{\mathbf{v}}_{\text{dip}}(\varphi + \pi, \theta, \chi; t) \rangle. \quad (2.25)$$

An alternative treatment that focuses explicitly on the influence of molecular rotations on HHG is given in references [47–50].

2.3 The multi-centre stationary-phase method

The Lewenstein model (2.19) is numerically much cheaper than solving the TDSE. However, there is a certain amount of redundancy in performing the full \mathbf{k} integral. Physically, only a few continuum trajectories contribute significantly to the harmonic generation. Mathematically, the integrand can be expressed as a slowly varying function of \mathbf{k} times a quickly varying phase [51]. The full integral is dominated by contributions from those \mathbf{k} values that correspond to stationary points of the phase.

In atomic HHG the only \mathbf{k} -dependent phase is the semi-classical action $S(\mathbf{k}, t, t')$, so the stationary phase is determined by

$$0 = \nabla_{\mathbf{k}} S(\mathbf{k}, t, t')|_{\mathbf{k}=\mathbf{k}_s}, \quad (2.26)$$

leading to the stationary momentum

$$\mathbf{k}_s(t, t') = -\frac{1}{t-t'} \int_{t'}^t \mathbf{A}(t'') dt''. \quad (2.27)$$

The physical picture is that only electrons that return to the nucleus contribute to HHG. This can be seen from the fact that the integral of the kinetic momentum, $\mathbf{q}(t'') = \mathbf{k}_{st}(t, t') + \mathbf{A}(t'')$, from time t' to t is zero.

Extra phase factors appear when we consider molecular targets with N_a nuclei. This is most easily seen if the wave function is expanded around the atomic centres \mathbf{R}_n :

$$\psi(\mathbf{r}) = \sum_{n=1}^{N_a} c_n \phi_n(\mathbf{r} - \mathbf{R}_n). \quad (2.28)$$

Taking the Fourier transform gives us

$$\tilde{\psi}(\mathbf{q}) = (2\pi)^{-3/2} \int_{\mathbb{R}^3} e^{-i\mathbf{q}\cdot\mathbf{r}} \sum_{n=1}^{N_a} c_n \phi_n(\mathbf{r} - \mathbf{R}_n) d\mathbf{r} \quad (2.29)$$

$$= \sum_{n=1}^{N_a} (2\pi)^{-3/2} \int_{\mathbb{R}^3} e^{-i\mathbf{q}\cdot\mathbf{r}} c_n \phi_n(\mathbf{r} - \mathbf{R}_n) d\mathbf{r} \quad (2.30)$$

$$= \sum_{n=1}^{N_a} (2\pi)^{-3/2} \int_{\mathbb{R}^3} e^{-i\mathbf{q}\cdot(\mathbf{r}+\mathbf{R}_n)} c_n \phi_n(\mathbf{r}) d\mathbf{r} \quad (2.31)$$

$$= \sum_{n=1}^{N_a} e^{-i\mathbf{q}\cdot\mathbf{R}_n} (2\pi)^{-3/2} \int_{\mathbb{R}^3} e^{-i\mathbf{q}\cdot\mathbf{r}} c_n \phi_n(\mathbf{r}) d\mathbf{r} \quad (2.32)$$

$$= \sum_{n=1}^{N_a} e^{-i\mathbf{q}\cdot\mathbf{R}_n} c_n \tilde{\phi}_n(\mathbf{q}), \quad (2.33)$$

The multi-centre stationary-phase method

so

$$\mathbf{d}_{\text{ion}}(\mathbf{q}) = i\nabla_{\mathbf{q}}\tilde{\psi}(\mathbf{q}) \quad (2.34)$$

$$= \sum_{n=1}^{N_a} e^{-i\mathbf{q}\cdot\mathbf{R}_n} (\mathbf{R}_n + i\nabla_{\mathbf{q}}) c_n \tilde{\phi}_n(\mathbf{q}), \quad (2.35)$$

and

$$\mathbf{v}_{\text{rec}}(\mathbf{q}) = \mathbf{q}\tilde{\psi}(\mathbf{q}) \quad (2.36)$$

$$= \sum_{n=1}^{N_a} e^{-i\mathbf{q}\cdot\mathbf{R}_n} \mathbf{q} c_n \tilde{\phi}_n(\mathbf{q}). \quad (2.37)$$

The ionization and recombination matrix elements thus split into sums over single-atom contributions

$$\mathbf{d}_{\text{ion}}(\mathbf{k} + \mathbf{A}(t')) = \sum_{n_i=1}^{N_a} \mathbf{d}_{\text{ion}}^{(n_i)}(\mathbf{k} + \mathbf{A}(t')) \quad (2.38)$$

$$\mathbf{v}_{\text{rec}}(\mathbf{k} + \mathbf{A}(t)) = \sum_{n_f=1}^{N_a} \mathbf{v}_{\text{rec}}^{(n_f)}(\mathbf{k} + \mathbf{A}(t)), \quad (2.39)$$

each having a phase factor of $e^{-i[\mathbf{k}+\mathbf{A}(t')]\cdot\mathbf{R}_{n_i}}$ or $e^{-i[\mathbf{k}+\mathbf{A}(t)]\cdot\mathbf{R}_{n_f}}$. Combining all the phases in equation (2.19), the stationary phase is determined by

$$0 = \nabla_{\mathbf{k}} \left(-iS(\mathbf{k}, t, t') + i[\mathbf{k} + \mathbf{A}(t)] \cdot \mathbf{R}_{n_f} - i[\mathbf{k} + \mathbf{A}(t')] \cdot \mathbf{R}_{n_i} \right) \Big|_{\mathbf{k}=\mathbf{k}_s} \quad (2.40)$$

for each combination of ionization site \mathbf{R}_{n_i} and recombination site \mathbf{R}_{n_f} . The resulting stationary momentum is

$$\begin{aligned} \mathbf{k}_s(t, t', n_f, n_i) &= -\frac{1}{t-t'} \int_{t'}^t \mathbf{A}(t'') dt'' \\ &+ \frac{1}{t-t'} (\mathbf{R}_{n_f} - \mathbf{R}_{n_i}). \end{aligned} \quad (2.41)$$

The interpretation of equation (2.41) is that the dominating electron trajectories are those that start at a nuclear centre at some time t' , and end up at a nuclear centre at a later time t . This can be formalized in terms of the Feynman path-interpretation of quantum mechanics [52]. Due to the strong laser field, the semi-classical phase varies so quickly that only the stationary (classical) trajectories contribute. This interpretation bridges the gap between a classical and quantum description of HHG.

Applying the multi-centre stationary-phase method to equation (2.19), we get

$$\begin{aligned}
 \langle \psi(t) | \hat{\mathbf{v}}_{\text{dip}} | \psi(t) \rangle &\approx i \sum_{n_i, n_f} \int_{t_0}^t dt' \left(\frac{2\pi}{\epsilon + i(t-t')} \right)^{3/2} \\
 &\times \left(\mathbf{v}_{\text{rec}}^{(n_f)}(\mathbf{k}_s + \mathbf{A}(t)) \right)^* e^{-iS(\mathbf{k}_s, t, t')} \\
 &\times \mathbf{F}(t') \cdot \mathbf{d}_{\text{ion}}^{(n_i)}(\mathbf{k}_s + \mathbf{A}(t')) \quad (2.42) \\
 &+ \text{complex conjugate,}
 \end{aligned}$$

where \mathbf{k}_s is calculated using equation (2.41). The ϵ in the denominator comes from performing an integral in the complex plane. The final spectra depend weakly on the exact value, especially at high harmonic orders. We always set ϵ equal to 1.

2.4 Short-comings of the Lewenstein model

The Lewenstein model is hugely successful. It qualitatively describes most experiments, and it bridges the gap between quantum mechanics and the semi-classical three-step model. Having said that, there are plenty of physical effects that the Lewenstein model does not include. A major simplification in the Lewenstein model is that all electron-electron interactions are ignored. This is true of any single-active electron model. Recently, several papers have questioned the validity of such an approach [53–58]

Another problem with the Lewenstein model is that it completely neglects the effect of the Coulomb potential on the continuum wave packet. This problem has been addressed in many ways, and we shall only mention a few here. The simplest is to replace the Volkov waves for the electron continuum with basis states that include the Coulomb potential in some way. This has been done using for example Coulomb waves [59, 60], Coulomb-Volkov states [59, 61], and Coulomb-eikonal Volkov states [62, 63].

In the quantitative rescattering (QRS) model, the harmonic process is factored into two parts: one describing ionization and propagation, and a second describing recombination [64, 65]. By using full scattering states in the recombination step, the QRS includes the Coulomb potential fully in the final step, but not in the preceding steps. A conceptually similar approach uses classical trajectory Monte Carlo to build up the returning returning continuum wave packet, and scattering theory to describe the recombination step [66]. Due to the simplicity of propagating a classical particle, this allows the Coulomb potential to be included fully in the propagation step.

The final problem we shall touch upon is the description of the bound state. The SFA, and thus also the Lewenstein model, totally ignores the influence of the strong driving laser on the bound state. There have been a few steps towards repairing this fault, most notably by taking into account depletion of the ground state [17]. Ground state depletion is important when the driving pulse is sufficiently intense to completely ionize the target molecule. Another effect is the adiabatic energy shift of each molecular orbital in response to the laser field. As we shall show in chapter 5, such Stark shifts can easily be incorporated into the Lewenstein model.

Ellipticity of high-harmonics

A gas of atoms submitted to a linearly polarized driving laser will emit harmonics that have the same polarization axis. This can easily be understood classically, where a charged particle emits radiation when accelerated. The continuum electron is only accelerated parallel to the polarization axis of the driving laser, and therefore emits radiation with the same polarizability. If the target is anisotropic, however, the symmetry is broken, and the electron can have a nonvanishing acceleration perpendicular to the laser polarization. This is exactly the case for aligned molecules, where experiments have shown a nonvanishing perpendicular component in HHG from N_2 , O_2 and CO_2 [67, 68]. In this chapter we will show why elliptically polarized harmonics appear naturally within the Lewenstein model, and compare to experiment and other theoretical models.

3.1 Ellipticity within the Lewenstein model

The setup is sketched in figure 3.1(a), where an N_2 molecule has been aligned at an angle of φ to the polarization axis of a linearly polarized driving laser that is propagating in the z direction. The molecule emits high harmonics that have a component $F_x(\omega)$ parallel to the laser polarization, and a component $F_y(\omega)$ perpendicular to the laser polarization. We shall refer to these as the parallel and perpendicular components. Depending on the ratio and relative phase of the two components, certain harmonics may be elliptically polarized. These harmonics will then trace out a polarization ellipse in time.

Figure 3.2 shows HHG spectra calculated for N_2 at three different alignment angles using a 20 cycle driving pulse at 800 nm with a cosine squared envelope, and a peak intensity of 2×10^{14} W/cm². As expected, the parallel component dominates the spectrum. In fact, the weaker perpendicular component disappears completely if we use the atomic stationary-phase method rather than the multi-centre stationary-phase method.

The dependence of the perpendicular component on the stationary momentum, \mathbf{k}_s , can easily be understood from the multi-centre stationary-phase version of the Lewenstein model (2.42). We start by noting that the vector character of the integrand is determined solely by \mathbf{v}_{rec} . According to equation (2.22), \mathbf{v}_{rec} is proportional to \mathbf{k}_s , which is given by

$$\begin{aligned} \mathbf{k}_s(t, t', n_f, n_i) = & -\frac{1}{t-t'} \int_{t'}^t \mathbf{A}(t'') dt'' \\ & + \frac{1}{t-t'} (\mathbf{R}_{n_f} - \mathbf{R}_{n_i}). \end{aligned} \quad (3.1)$$

In other words, trajectories that start at one nuclear centre and end up at another gain a drift momentum, which can cause a perpendicular component of the harmonic signal if the molecule is aligned at an angle to the laser polarization axis.

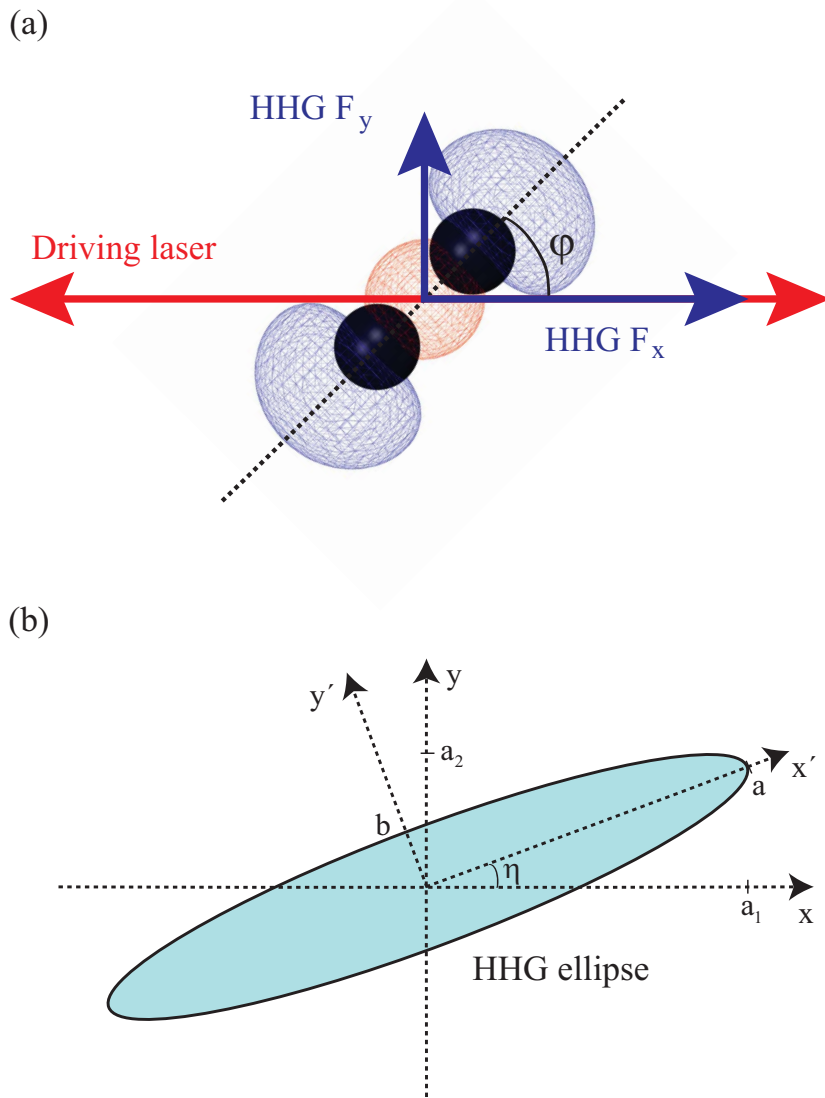


Figure 3.1 | (a) The HOMO of N_2 is oriented at an angle of φ to the polarization axis of the driving laser. The emitted harmonics have a non-vanishing perpendicular component due to the broken symmetry. (b) Sketch of the polarization ellipse of an emitted harmonic.

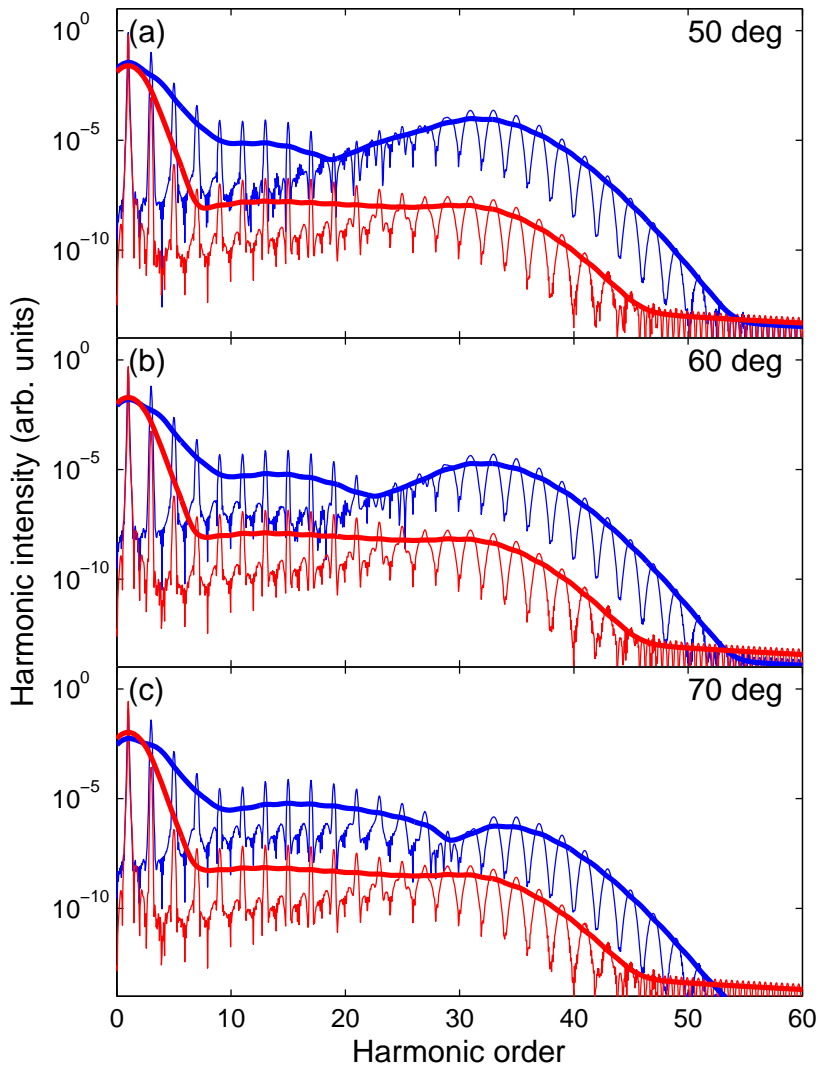


Figure 3.2 | Parallel (blue) and perpendicular (red) components of HHG spectra from aligned N_2 at three different alignment angles. Short trajectories have been selected using a filter. Thick lines indicate smoothed spectra.

The plateau of the perpendicular component in figure 3.2 is very flat. The ratio between the parallel and perpendicular components is thus determined by the minimum in the parallel component, which moves to higher energies when the alignment angle is increased. This is the so-called two-centre interference minimum [69], which we will treat at length in chapter 6. Unlike the perpendicular component, the parallel component hardly changes if the drift momentum is not included in \mathbf{k}_s .

The associated ellipticity is calculated following the treatment of Born and Wolf [70] in terms of the (complex) spectral amplitudes $A^{\parallel}(\omega)$ and $A^{\perp}(\omega)$. The amplitudes relate to the electric fields through $\text{Re}[A^{\parallel}(\omega)] = F_x(\omega)$, and $\text{Re}[A^{\perp}(\omega)] = F_y(\omega)$. We define

$$a_1(\omega) = |A^{\parallel}(\omega)| \quad (3.2)$$

$$\delta_1(\omega) = \text{Arg}(A^{\parallel}(\omega)) \quad (3.3)$$

$$a_2(\omega) = |A^{\perp}(\omega)| \quad (3.4)$$

$$\delta_2(\omega) = \text{Arg}(A^{\perp}(\omega)). \quad (3.5)$$

The ellipticity ϵ , and the angle η between the major axis of the polarization ellipse and the polarization axis of the driving laser are then given by

$$\epsilon = \tan \left(\frac{1}{2} \text{asin} [\sin (2 \text{atan} (a_2/a_1)) \sin(\delta_2 - \delta_1)] \right) \quad (3.6)$$

$$\eta = \frac{1}{2} \text{atan} \left(\frac{2a_1a_2}{a_1^2 - a_2^2} \cos(\delta_2 - \delta_1) \right), \quad (3.7)$$

where the omegas have been dropped to ease notation. The major axis angle η is sketched in figure 3.1(b). In terms of the minor and major axis of the polarization ellipse, $|\epsilon| = b/a$.

Applying the above equations, we get the absolute ellipticities plotted in figure 3.3. The ellipticity is seen to peak around the 19th harmonic at $\varphi = 40^\circ$, and move out towards the 25th harmonic at $\varphi = 60^\circ$. The sudden dip at 60° is caused by a rapid sign change, not a change in the relative intensities of the parallel

Ellipticity within the Lewenstein model

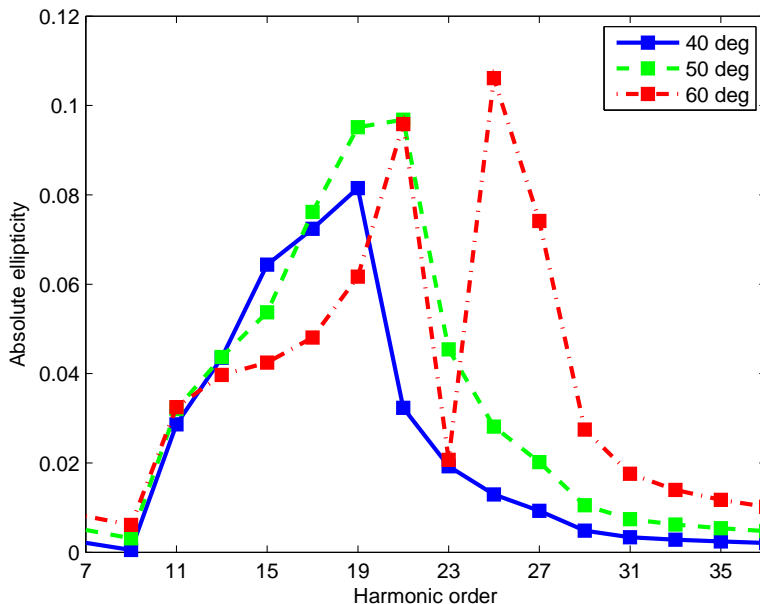


Figure 3.3 | Ellipticities for three alignment angles of N_2 . Short trajectories have been selected using a smooth window function.

and perpendicular components. The shift to higher harmonics at larger φ is a signature of a two-centre interference in the parallel component. Such a shift is not seen in experiment [68], which is consistent with other experiments showing that the interference minimum in N_2 in fact hardly moves with alignment angle [71]. It has been suggested that the interference minimum in N_2 is similar to the so-called Cooper minimum in Ar [72, 73], which cannot be described using plane waves [72].

The dependence on alignment angle in figure 3.3 is the same as that published in our earlier work [74]. The magnitude, however, differs significantly. Where the old results gave ellipticities that were more than an order of magnitude smaller than the experimental value, the new results only differ by about a factor

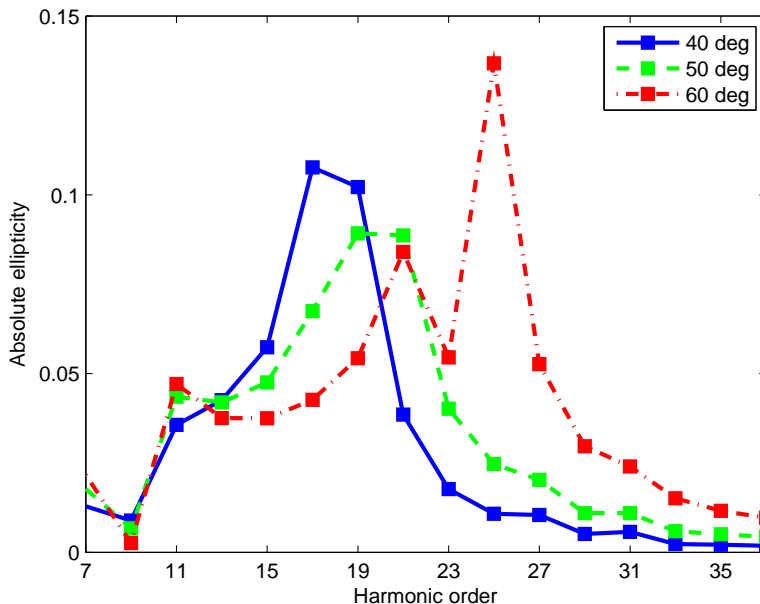


Figure 3.4 | Ellipticities for three alignment angles of N_2 . Short and long trajectories are both included.

of 3. The reason given in reference [74] was that the artificial trapezoidal pulse envelope gave numerical noise in the transition between the linear ramp-up and the central part of the envelope. This noise was visible in the perpendicular component, where it was large enough to drown out individual harmonics unless the intensity was raised to $6 \times 10^{14} \text{ W/cm}^2$.

Another source of noise arose from the way that short trajectories were selected. For a fixed time t , each t' gives rise to some contribution to $\langle \hat{v}_{\text{dip}}(t) \rangle$. When $t - t'$ is larger than roughly $2T/3$, this contribution is from the long trajectory. In reference [74] we selected short trajectories by limiting the t' integral in equation (2.42) to $0.67T$, which introduces noise when the Fourier transform is performed afterwards. In the new cal-

ulation we multiply the contribution at each t' with a smooth window function based on the Fermi-Dirac distribution

$$w(t') = 1 - \left[\exp \left(\frac{(t - t') - 0.95 \cdot 2T/3}{0.03T} \right) + 1 \right]^{-1}. \quad (3.8)$$

The exact form is *ad hoc*. The position and width is chosen so as to allow part of the long trajectory to contribute near the harmonic cutoff, rather than removing any of the short trajectory contribution. The reason we want to avoid the long trajectory contribution is that it causes additional interferences, which are not seen under normal experimental conditions [18]. However, for completeness we plot the ellipticities for a calculation that includes both sets of trajectories in figure 3.4. The addition of the long trajectories does not significantly change our results.

3.2 Comparison with other models

The ellipticity of high-order harmonics has also been investigated using the T -matrix formalism [75], which is similar to the Lewenstein model in many ways. Very large ellipticities were obtained due to the perpendicular component being stronger than the parallel component at certain angles and harmonic energies [75, 76]. Also, the perpendicular component was much more structured than is the case in our Lewenstein calculations. One possible explanation is found in the recombination step. We use the dipole velocity operator for the recombination step, whereas the dipole operator was used in references [75, 76].

Figure 3.5 shows spectra calculated using the Lewenstein model under the same conditions as in Figure 3.5, except that we now use the dipole operator for the recombination step. The spectra have been multiplied by a factor of ω^2 to get the right scaling. Figure 3.5 shows that the length form weights the perpendicular component much more strongly than the velocity form. This is not too surprising given our discussion in section 3.1. In the velocity form, the vector character of the emitted radiation is

completely determined by the wave vector of the recombining electron. This is restricted to be predominantly parallel to the polarization axis of the driving laser due to the use of the multi-centre stationary phase method. In the length form, the vector character is determined by the recombination dipole matrix element, which can have a perpendicular component even when the returning electron is moving strictly parallel to the laser polarization. In our calculation, the perpendicular component can even dominate over the parallel component at high energies, as seen in figure 3.5. The corresponding ellipticities are shown in figure 3.6. The length form calculation seems to be in better agreement with experiment between the 11th and the 29th harmonic, but differs substantially outside this range.

It is difficult to directly compare our results to those in reference [75], but there are a few more differences in the methods that might influence the final ellipticities. Firstly, reference [75] uses Slater-type orbitals for the ground state rather than our (unphysical) Gaussian orbitals. The asymptotic behaviour has been shown to be important in for example photoelectron angular distributions of CO₂ [77, 78]. Secondly, reference [75] employs a field dressing of the initial state, which we do not. Smaller differences include the restriction to infinitely long driving pulses, and use of the atomic stationary-phase method.

Although comparisons between the Lewenstein model and T -matrix formalism are interesting, they do not necessarily give an added insight into the discrepancies between the experiment and our Lewenstein results. As mentioned in section 3.1, it is likely that the interference minimum in N₂ is Cooper-like in origin, rather than a result of two-centre interference. If the interference minimum really is Cooper-like in origin, then the electron continuum must be described in a basis that allows different partial waves to interfere [72]. This might be done using the formalism in references [47–49], where the electron continuum is expanded in partial waves. No direct comparison to ellipticity experiments have been made using this theory, however. By far the best agreement has been reached using the QRS [79, 80], which depends on

Comparison with other models

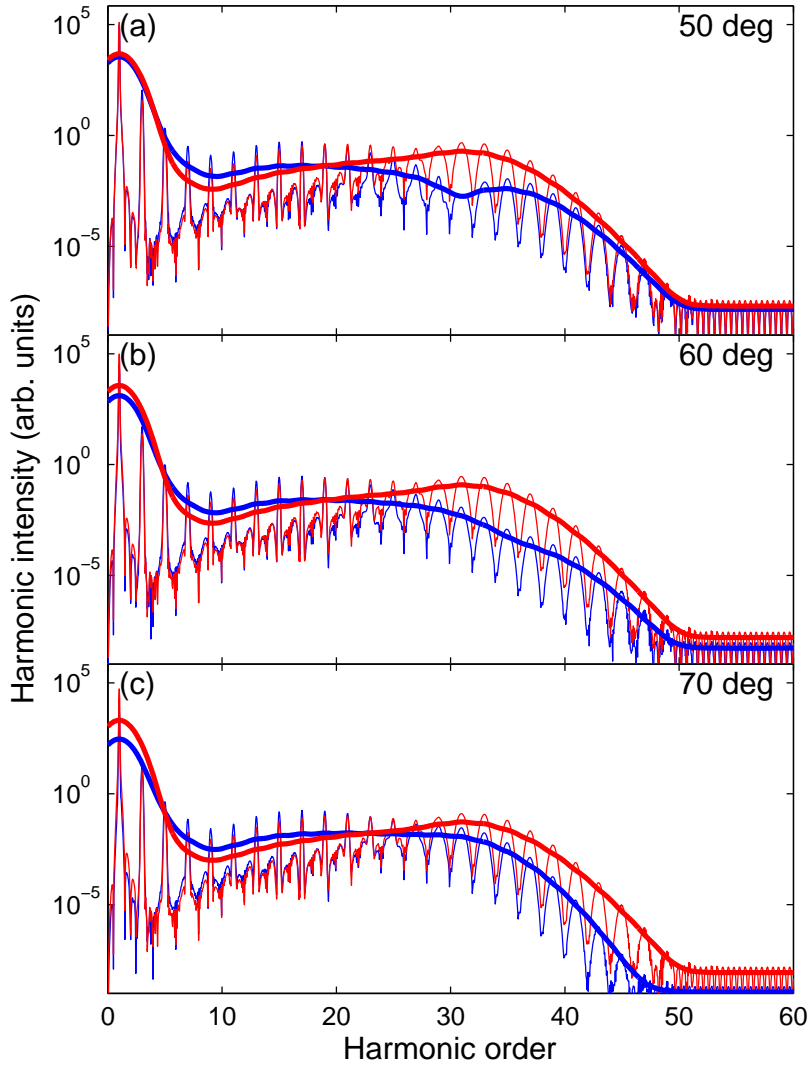


Figure 3.5 | Parallel (blue) and perpendicular (red) components of HHG spectra from aligned N_2 at three different alignment angles. The calculation is performed using the length form for the recombination step. Short trajectories have been selected using a filter. Thick lines indicate smoothed spectra.

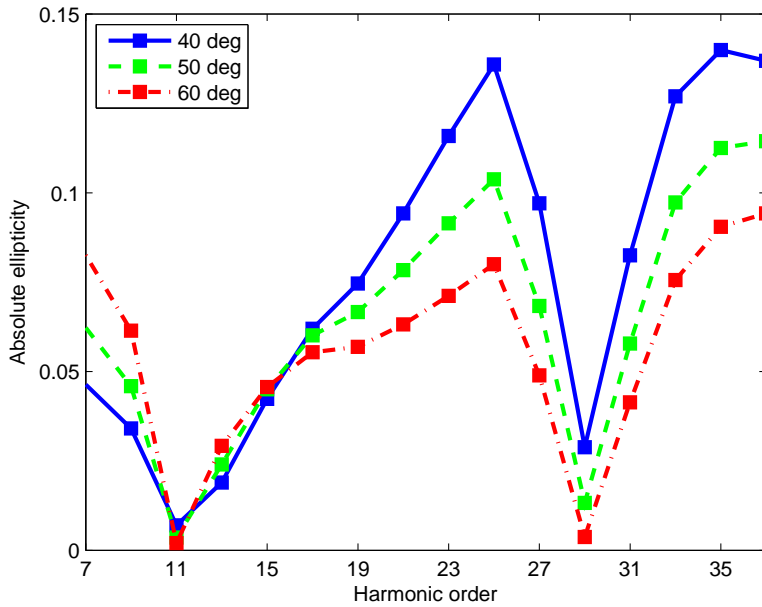


Figure 3.6 | Ellipticities for three alignment angles of N_2 . The calculation is performed using the length form for the recombination step. Short trajectories have been selected using a smooth window function.

a factorization of the harmonic process, and uses full field-free scattering states for the recombination step.

Influence of polar orbitals

The most common target in HHG experiments are the noble gas atoms, but advances in laser alignment techniques have caused an increased interest in molecules like N₂, O₂, and CO₂. The differences between HHG from atoms and molecules are often due to the broken rotational symmetry of the target. Moving to polar molecules we also break the inversion symmetry along the internuclear axis. In this chapter we will discuss two major effects this has on HHG: gating of the high-harmonic emission times, and the appearance of even harmonics. Our goal is to highlight some of the differences between HHG from polar and nonpolar molecules, but also to establish a base line with which to compare our Stark-extended Lewenstein model in the remainder of the thesis.

4.1 Emission times

Although HHG is most often described in the frequency domain, a lot can be learnt by applying a time-frequency analysis on the time-dependent dipole velocity [81]. We use the Gabor transform,

which is a Fourier transform with a sliding Gaussian window:

$$\langle \hat{\mathbf{v}}_{\text{dip}}(\omega, t) \rangle = \int_{-\infty}^{\infty} e^{-i\omega t'} \langle \hat{\mathbf{v}}_{\text{dip}}(t) \rangle e^{-4 \log(2)(t'-t)^2/\text{FWHM}^2} dt'. \quad (4.1)$$

The Gabor transform gives the frequency content of the time-dependent dipole in a window around time t . The longer the window, the higher the precision in frequency space but lower precision in time. A good compromise for HHG is $\text{FWHM} = 0.1T$, where T is one optical cycle of the driving laser. The phase of the Gabor transform is never relevant for our purposes, so we will always plot the norm.

To illustrate the principle, we orient a CO molecule parallel to the polarization axis of a linearly polarized laser pulse, which has a central wave length of 800 nm, a cosine-squared envelope, a total duration of 20 optical cycles, and a peak intensity of 2×10^{14} W/cm². We only include the HOMO contribution, so the geometry is as sketched in figure 4.1. The time-dependent expectation value of the dipole velocity is calculated using the Lewenstein model, and the Gabor transform applied. The result is shown in figure 4.2(a).

The harmonics are seen to come in bursts each half-cycle. Each harmonic burst consists of two branches, known as the short and long trajectories. There is a clear difference in the strength of harmonic bursts in neighbouring half-cycles. The dominating bursts shift by one half-cycle when the molecule is flipped in figure 4.2(b). This difference between neighbouring half-cycles is due to the shape of the HOMO, which favours ionization when the electric field points from C to O. We refer to this as geometric gating. Figure 4.2(c) shows the aligned case for comparison. When the CO molecule is aligned, there is nothing to break the symmetry between neighbouring half-cycles. We will return to the implications of this in section 4.2.

The gating in the ionization step does not follow from the ionization matrix element in isolation, as we shall now show. To simplify the argument we consider the case of an infinitely long driving pulse that is polarized parallel to the internuclear axis.

Emission times

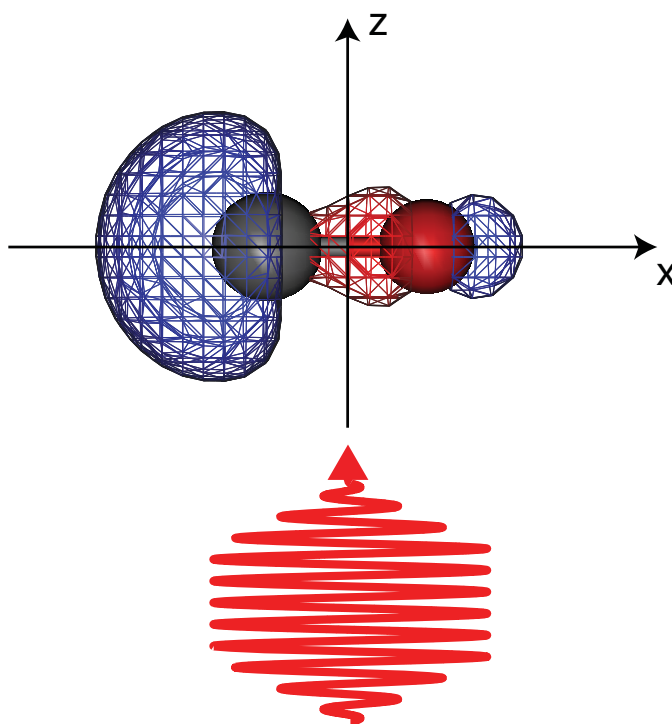


Figure 4.1 | A CO molecule oriented at $\varphi = 0^\circ$ is submitted to a strong laser pulse, which is linearly polarized in the x direction and propagating in the z direction. The carbon atom is to the left, and the oxygen is to the right. Also shown is the HOMO, which has a permanent dipole pointing from C to O.

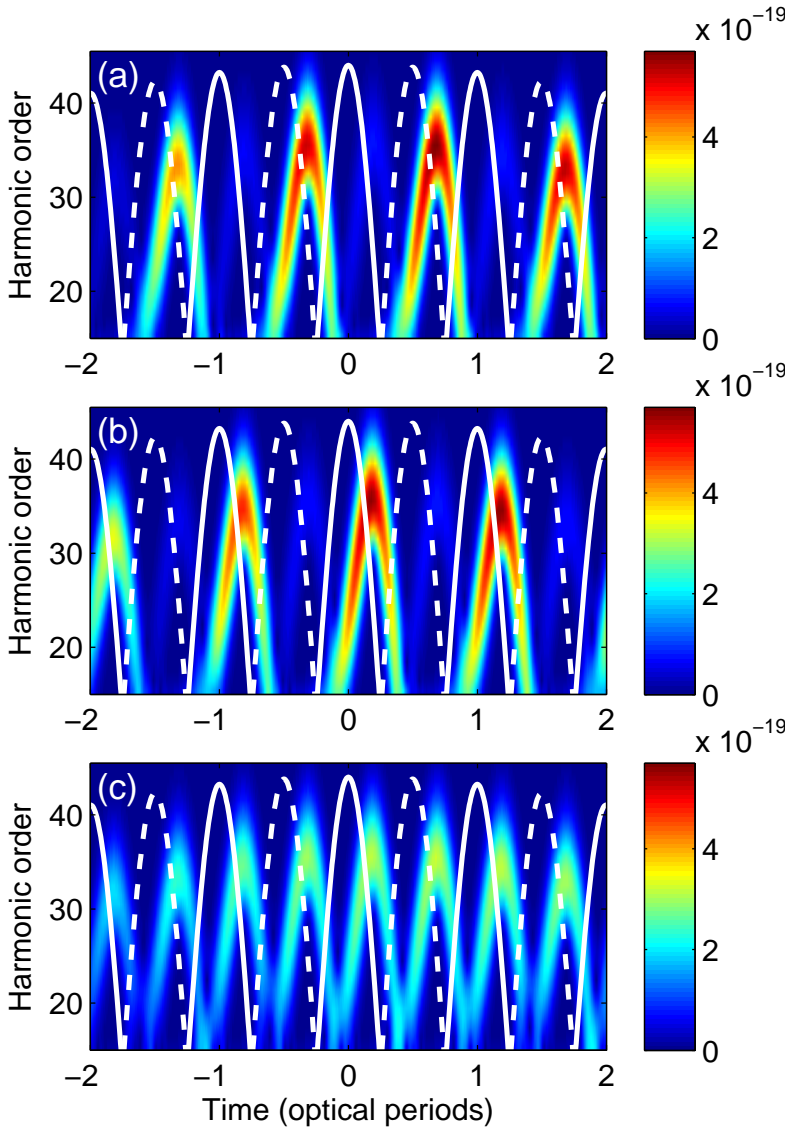


Figure 4.2 | Emission times of CO (a) oriented at $\varphi = 0^\circ$, (b) oriented at $\varphi = 180^\circ$, and (c) aligned at $\varphi = 0^\circ$. The driving pulse is indicated with a white line. The solid white line indicates that the electric field is positive, the dashed white line that the electric field is negative.

Emission times

Applying the atomic stationary-phase approximation leads to the stationary momentum

$$\mathbf{k}_s(t, t') = -\frac{1}{t - t'} \int_{t'}^t \mathbf{A}(t'') dt''. \quad (4.2)$$

In the limit of infinitely long pulses, changing the half-cycle is just the same as changing the sign of \mathbf{A} . This shows that \mathbf{k}_s changes sign when going from one half-cycle to the next. According to equation (2.20), ionization is initiated via the matrix element

$$\mathbf{d}_{\text{ion}}(\mathbf{k}_s) = \langle \mathbf{k}_s | \mathbf{r} | \psi \rangle \quad (4.3)$$

$$= i \nabla_{\mathbf{k}_s} \tilde{\psi}(\mathbf{k}_s). \quad (4.4)$$

Using general properties of the Fourier transform we see that

$$\tilde{\psi}(-\mathbf{k}_s) = \tilde{\psi}^*(\mathbf{k}_s), \quad (4.5)$$

so

$$i \nabla_{-\mathbf{k}_s} \tilde{\psi}(-\mathbf{k}_s) = -i \nabla_{\mathbf{k}_s} \tilde{\psi}^*(\mathbf{k}_s). \quad (4.6)$$

If the norm of the ionization matrix element is used as a measure of ionization probability, then equations (4.4) and (4.6) say that ionization is equally probable in both directions. This is clearly not the case in figure 4.2.

Gating in the Lewenstein model is caused by an interplay of all three steps in HHG. Based on the above, we can conclude that changing half-cycle is the same as making the replacement

$$\mathbf{F}(t') \cdot \mathbf{d}_{\text{ion}}(\mathbf{k}_s, t') \rightarrow -\mathbf{F}(t') \cdot \mathbf{d}_{\text{ion}}^*(\mathbf{k}_s, t'). \quad (4.7)$$

Comparing equations (2.22) and (4.5) for the recombination step, we conclude that changing half-cycle is the same as making the replacement

$$\mathbf{v}_{\text{rec}}^*(\mathbf{k}_s, t) \rightarrow -\mathbf{v}_{\text{rec}}(\mathbf{k}_s, t). \quad (4.8)$$

The semi-classical phase $S(\mathbf{k}_s, t, t')$ only depends on the kinetic energy of the continuum electron and the energy of the bound state, neither of which changes between half-cycles. The total impact of changing half-cycle is thus to replace the integrand in the Lewenstein integral (2.42)

$$i\mathbf{v}_{\text{rec}}^*(\mathbf{k}_s, t)e^{-iS(\mathbf{k}_s, t, t')} \mathbf{F}(t') \cdot \mathbf{d}_{\text{ion}}(\mathbf{k}_s, t') \quad (4.9)$$

with

$$i\mathbf{v}_{\text{rec}}(\mathbf{k}_s, t)e^{-iS(\mathbf{k}_s, t, t')} \mathbf{F}(t') \cdot \mathbf{d}_{\text{ion}}^*(\mathbf{k}_s, t'). \quad (4.10)$$

The contribution to the dipole velocity from either half-cycle is then obtained from equation (2.42) by taking the real part of equation (4.9) or (4.10) and integrating from t' to t . Taking the cutoff harmonics as an example, this corresponds to integrating two thirds of an optical cycle, starting at the peak of an optical half-cycle. This will give different results as

$$\text{Re} [i\mathbf{v}_{\text{rec}}^* e^{-iS} \mathbf{F} \cdot \mathbf{d}_{\text{ion}}] \neq \text{Re} [i\mathbf{v}_{\text{rec}} e^{-iS} \mathbf{F} \cdot \mathbf{d}_{\text{ion}}^*] \quad (4.11)$$

when the molecular orbital is not symmetric along the polarization axis of the laser. This is exactly the case for polar orbitals.

The above argument does not take into account the exchange harmonics, nor does it predict *which* half-cycle is the dominating one. A more intuitive explanation is that most of the electron density is centred on C, so most of the ionization has to happen from C. When the electric field points from O to C, the (small) charge on O forms a barrier that prevents the charge on C from tunnelling out. Polar orbitals thus tend to have higher ionization rates when the electric field points opposite to their permanent dipole.

4.2 Odd and even harmonics

The HHG spectra we have looked at so far only contain peaks at an odd integer times the frequency ω_0 of the driving laser. This

is a very general feature of HHG from symmetric targets, and is a consequence of the periodicity of HHG [82]. In the limit of infinitely long driving pulses, the expectation value of the dipole velocity is periodic with a period of one optical cycle T . The Fourier transform only picks out the frequency components that correspond to an integer times ω_0 . If the target is symmetric under inversion along the polarization axis of the laser, then the dipole velocity changes sign every half-cycle

$$\langle \hat{\mathbf{v}}(t + T/2) \rangle = - \langle \hat{\mathbf{v}}(t) \rangle. \quad (4.12)$$

Taking the Fourier transform, this means that only the odd multiples of ω_0 survive. Equation (4.12) is fulfilled for all atoms and symmetric molecules.

It is clear from figure 4.2(a) and (b) that equation (4.12) is far from being fulfilled for oriented CO. Breaking this symmetry means that also even Fourier components get picked out, so HHG spectra from polar molecules are characterized by a set of peaks at all integer values of ω_0 . This is illustrated in figure 4.3, where spectra from oriented and aligned CO are compared. The aligned spectrum is calculated by adding opposite orientations coherently using equation (2.25).

The nice sharp peaks in figure 4.3 disappear if the driving pulse is sufficiently short only a few harmonic bursts contribute to the total spectrum. In the limit of just one harmonic burst, the HHG spectrum turns into a continuum. The spectrum also becomes less smooth if the short and long trajectories are allowed to interfere with each other.

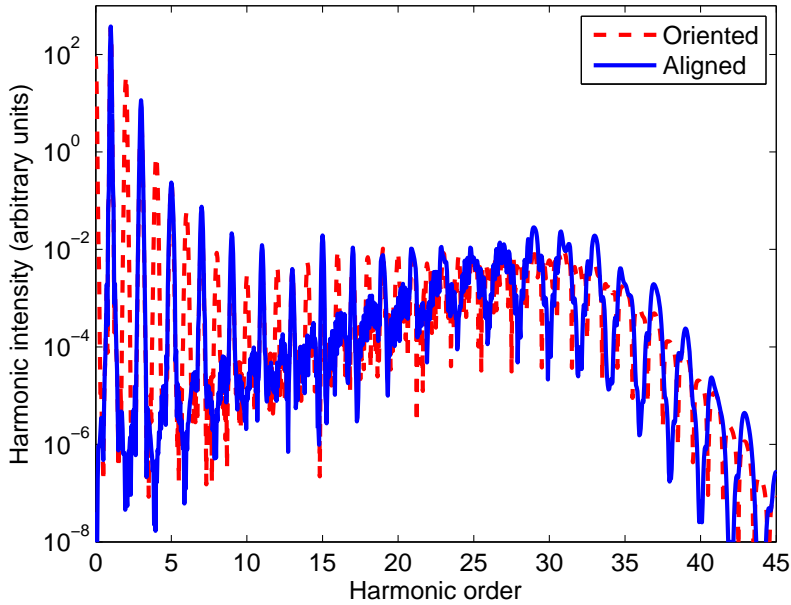


Figure 4.3 | Harmonic spectra from oriented and aligned CO. Even harmonics appear when CO is oriented, which breaks the symmetry between neighbouring half-cycles. Short trajectories have been selected using a smooth filter.

Including Stark shifts

When deriving the SFA, which underlies the Lewenstein model, the target state is assumed to be completely unaffected by the strong laser field until a time when it promotes an electron wave packet into the continuum. The continuum electron is then assumed to propagate independently of the Coulomb potential while the residual ground state wave packet continues to be unaffected by the laser. When the two wave packets overlap at a later time the resulting charge density modulations lead to the emission of high-order harmonics. As mentioned in section 2.4, this approach neglects several physical effects. One such effect is the time-dependent Stark shift of the bound state caused by the laser, which will be the topic of this chapter.

5.1 Derivation

In section 2.1 we derived the SFA wave function

$$|\psi(t)\rangle \approx |\psi^{(0)}(t)\rangle - i \int_{t_0}^t dt' \int_{\mathbb{R}^3} d\mathbf{k} |\mathbf{k}(t)\rangle \langle \mathbf{k}(t') | V_L(t') | \psi^{(0)}(t')\rangle, \quad (5.1)$$

where

$$|\psi^{(0)}(t)\rangle = \exp\left(-i \int_{t_0}^t \hat{H}_0 dt'\right) |\psi^{(0)}(t_0)\rangle \quad (5.2)$$

$$= \exp(-iE_0(t-t_0)) |\psi^{(0)}(t_0)\rangle. \quad (5.3)$$

This approach is expected to work well if the field-free time-evolution operator gives roughly the same result as the full time-evolution operator when applied to the ground state. This is the case for atoms as well as many symmetric molecules. If, however, the target state is polar (or very polarizable), then the instantaneous energy is expected to shift due to the laser-induced Stark shift:

$$E(\mathbf{F}(t)) = E_0 - \mu^i F_i(t) - \frac{1}{2} \alpha^{ij} F_i(t) F_j(t) - \frac{1}{3!} \beta^{ijk} F_i(t) F_j(t) F_k(t) - \dots \quad (5.4)$$

$$\approx E_0 - \boldsymbol{\mu} \cdot \mathbf{F}(t) - \frac{1}{2} \mathbf{F}^T(t) \underline{\underline{\boldsymbol{\alpha}}} \mathbf{F}(t). \quad (5.5)$$

Einstein summation is used in the upper equation, whereas vector notation is used in the lower. Typical intensities of 2×10^{14} W/cm² translate to field strengths of $\sqrt{2 \times 10^{14}/3.51 \times 10^{16}} = 0.075$ au, so it is usually enough to include the first- and second-order Stark shifts. The field-free vertical ionization potential is $I_p = |E_0|$, the permanent dipole of the orbital is $\boldsymbol{\mu}$, and the polarizability matrix of the orbital is $\underline{\underline{\boldsymbol{\alpha}}}$. The polarizability tensor $\underline{\underline{\boldsymbol{\alpha}}}$ is a diagonal matrix with elements α_{\parallel} and α_{\perp} in the special case of linear molecules. In practice we use equation (5.5) to define

Derivation

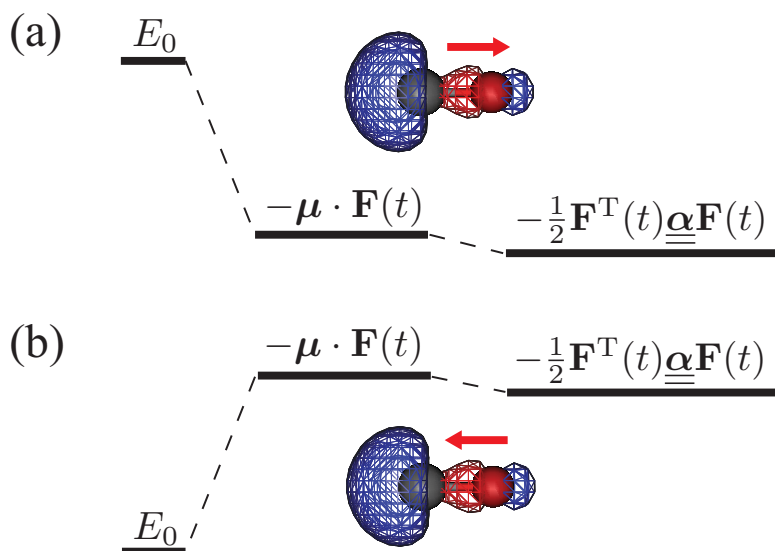


Figure 5.1 | Sketch of the Stark shift felt by the HOMO of CO when subject to an electric field. The relative size of the first- and second-order Stark shift is drawn to scale for an electric field $F_0 = 0.075$ au, corresponding to a laser intensity of 2×10^{14} W/cm². (a) The electric field is parallel to the permanent dipole of the orbital, and the effective ionization potential is raised. (b) The electric field is antiparallel to the permanent dipole, and the effective ionization potential is lowered.

$\underline{\boldsymbol{\mu}}$ and $\underline{\underline{\boldsymbol{\alpha}}}$ by calculating the ground state orbitals for the target molecule at a range of field strengths, and fitting the energies to a second-order polynomial. The exact values of the dipole and polarizability tensor depend on the choice of basis set. The sign and order of magnitude does not change, however, so all our results agree qualitatively if another basis set is used. The relative size of the first- and second-order Stark shifts is illustrated in figure 5.1 for the HOMO of CO obtained using a triple zeta valence basis set.

Returning to the time-evolution of the bound state, we now assume that the driving laser varies so slowly that the ground state adiabatically shifts its energy according to equation (5.5) [40–44, 83]. This is not unreasonable when comparing the atomic unit of time with that of a single infrared optical cycle. Equation (5.3) then takes the form

$$|\psi^{(0)}(t)\rangle = \exp\left(-i \int_{t_0}^t E(\mathbf{F}(t')) dt'\right) |\psi^{(0)}(t_0)\rangle. \quad (5.6)$$

The Lewenstein model is completely unaffected by this, except that the semi-classical phase has to be changed to

$$S(\mathbf{k}, t, t') = \int_{t'}^t \left(\frac{1}{2} [\mathbf{k} + \mathbf{A}(t'')]^2 - E(\mathbf{F}(t'')) \right) dt''. \quad (5.7)$$

The above model assumes that the dynamics of the continuum electron is perfectly described by a Volkov wave. As discussed in section 2.4, this is of course not the case. The Coulomb potential of the residual ion is long-range, and can change the continuum trajectories in some cases. The Coulomb potential is the first term in a multi-pole expansion of the full potential caused by the molecular ion. In the case of polar molecules, the next-to-leading term is also nonvanishing due to a permanent dipole of the residual ion. Shorter in range than the Coulomb interaction, the dipole interaction influences the active electron if it tunnels into the continuum sufficiently close to the origin. This has a major impact on photoelectron angular distributions from small polar molecules such as HF and LiF [84]. In larger molecules like CO and OCS, the active electron tunnels into the continuum sufficiently far from the origin for the dipole potential to be negligible [84]. This still leaves the Coulomb potential unaccounted for, but that was the case for nonpolar molecules anyway.

The remainder of this chapter is dedicated to the consequences of including the Stark effect in the Lewenstein model via equation (5.7).

5.2 Impact on emission times

It is plausible from figure 5.1 that the Stark shift should make it easier or harder for the electron to tunnel out of the bound state depending on whether the effective ionization potential

$$I_p(\mathbf{F}(t)) = |E_0| + \boldsymbol{\mu} \cdot \mathbf{F}(t) + \frac{1}{2} \mathbf{F}^T(t) \underline{\underline{\boldsymbol{\alpha}}} \mathbf{F}(t) \quad (5.8)$$

is raised or lowered. This is indeed the case in ionization experiments on oriented OCS molecules, where the time-dependent Stark shift dominates the ionization dynamics due to the HOMO's exceptionally large dipole [41]. As ionization is the first step in HHG, we also expect HHG to be sensitive to Stark shifts.

We use the Gabor transform described in section 4.1 to analyze the impact of including Stark shifts. Figure 5.2(a) shows the emission times of high harmonics generated from the HOMO of CO without inclusion of the Stark effect. We orient the CO molecule such that the permanent dipole of the HOMO points in the positive x direction. The driving pulse is linearly polarized along the x axis, has a central wave length of 800 nm, a cosine-squared envelope, a total duration of 10 optical cycles, and a peak intensity of 2×10^{14} W/cm². As in section 4.1, we clearly see the asymmetry between neighbouring half-cycles, which is caused by geometric gating.

Figure 5.2(b) shows the same calculation, but this time including the Stark shift in the semi-classical phase (5.7). The Stark effect suppresses the dominating harmonic bursts (note the different scale on the false-colour plot), and slightly increases the others. Referring to figure 5.1, it is obvious that the linear Stark shift will counteract geometric gating because the ionization potential is raised when the field points parallel to the permanent dipole. As mentioned, this is the dominating effect in ionization from OCS [41]. In our calculation, the Stark shift reduces the effectiveness of geometric gating in CO rather than reversing the preferred direction of ionization. This is in agreement

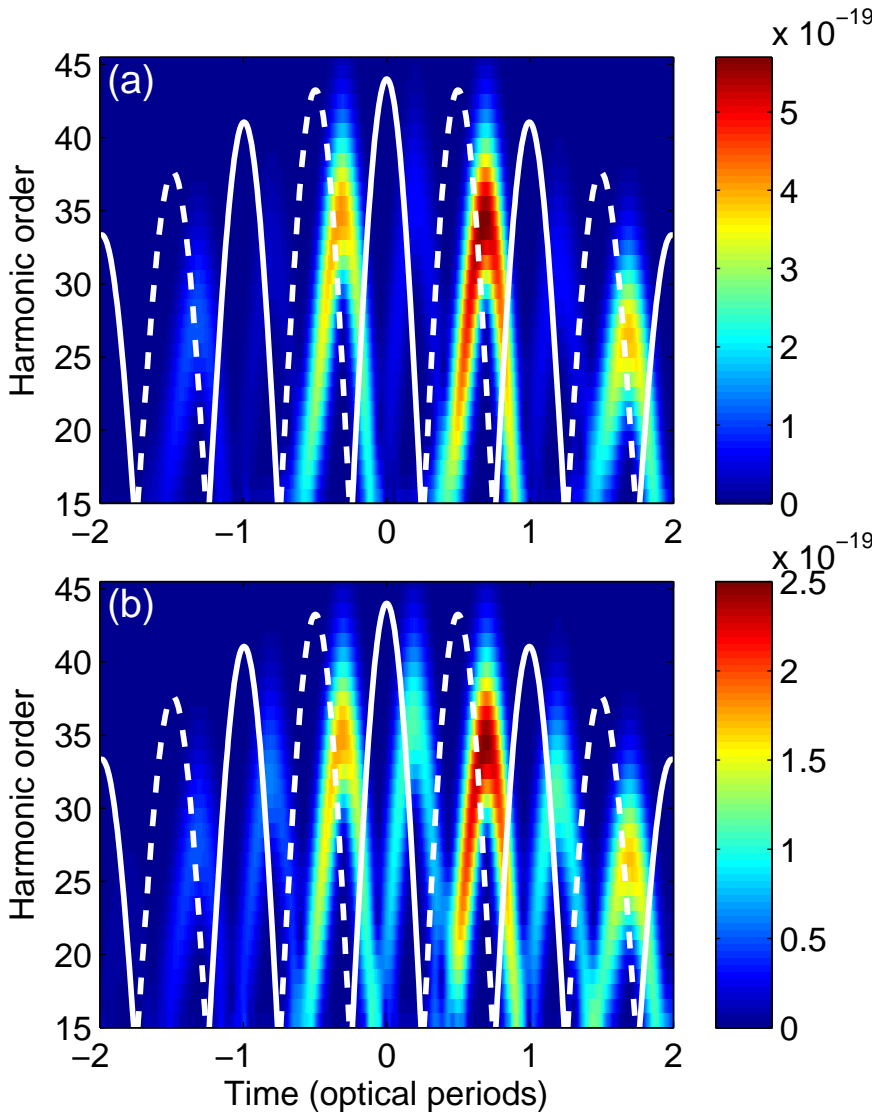


Figure 5.2 | Emission times for CO (a) without, and (b) with the Stark shift included. The white line indicates the driving field, with the solid line indicating that $F_x(t) > 0$, and the dashed line that $F_x(t) < 0$. The CO molecule is oriented parallel to the polarization axis of the laser, with the permanent dipole pointing upwards in the figure. Note the different colour-scales in the two panels.

Impact on emission times

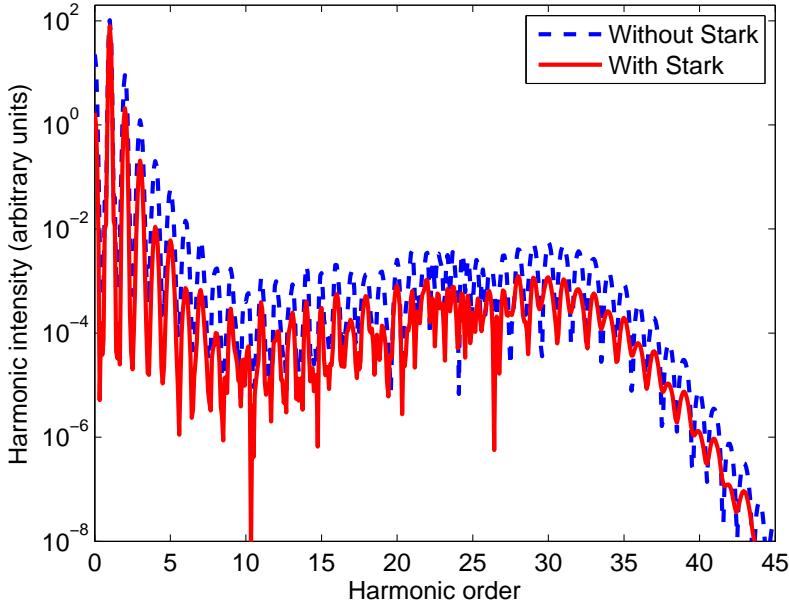


Figure 5.3 | Power spectra for oriented CO with and without including the Stark effect. Short trajectories have been selected using a smooth window function.

with recent experiments [85, 86], as well as theoretical results on above-threshold ionization (ATI) [87].

As figure 5.2 shows, the Stark effect has a big influence on HHG emission times within our Stark-corrected Lewenstein model. However, it is experimentally very hard to break the head-to-tail symmetry in molecular gasses. The highest level of orientation is obtained with state-selected gasses, but the state-selection process results in very low gas densities. The cross section for HHG is already quite low, so higher densities are required given current detector efficiencies. An alternative is to use multi-colour pulses, but that results in a low degree of head-to-tail symmetry breaking. Add to this that time-domain characterization of HHG pulse trains in itself is challenging, and the question arises whether it

is at all possible to experimentally verify or falsify the Stark-corrected Lewenstein model. The power spectra are shown in figure 5.3. The Stark effect lowers the harmonic intensity slightly, which is consistent with the observations we made in connection with the time-profile analysis in figure 5.2. However, there is no experimental way of accessing this decrease in harmonic intensity, as there is no available reference system. Apart from this, there seems to be no systematic change in the power spectrum associated with the Stark effect. This leaves one observable, namely the harmonic phase.

5.3 Stark phases

As the bound state evolves in time from t' to t , it accumulates the phase $\int_{t'}^t E(\mathbf{F}(t''))dt''$. According to equation (5.5) the accumulated phase differs from the field-free time-evolution by a Stark phase

$$\Phi_{\text{Stark}}(t, t') = \Phi_{\text{Stark}}^{(1)}(t, t') + \Phi_{\text{Stark}}^{(2)}(t, t'), \quad (5.9)$$

where the first- and second-order Stark phases read

$$\Phi_{\text{Stark}}^{(1)}(t, t') = - \int_{t'}^t \boldsymbol{\mu} \cdot \mathbf{F}(t'') dt'' \quad (5.10)$$

$$\Phi_{\text{Stark}}^{(2)}(t, t') = - \frac{1}{2} \int_{t'}^t \mathbf{F}^T(t'') \underline{\underline{\boldsymbol{\alpha}}} \mathbf{F}(t'') dt''. \quad (5.11)$$

The first-order Stark phase can be extracted by subtracting harmonic phases calculated with and without inclusion of the first-order Stark shift in the Lewenstein model. The result is plotted as connected black dots in figure 5.4(a), where the HOMO of CO has been submitted to an ultra short pulse. The second-order Stark phase, plotted in figure 5.4(b), is extracted by including the first and second-order Stark shifts in the Lewenstein model, calculating the harmonic phases, and then subtracting the phase obtained when only the first-order Stark shift is included. Both

Stark phases

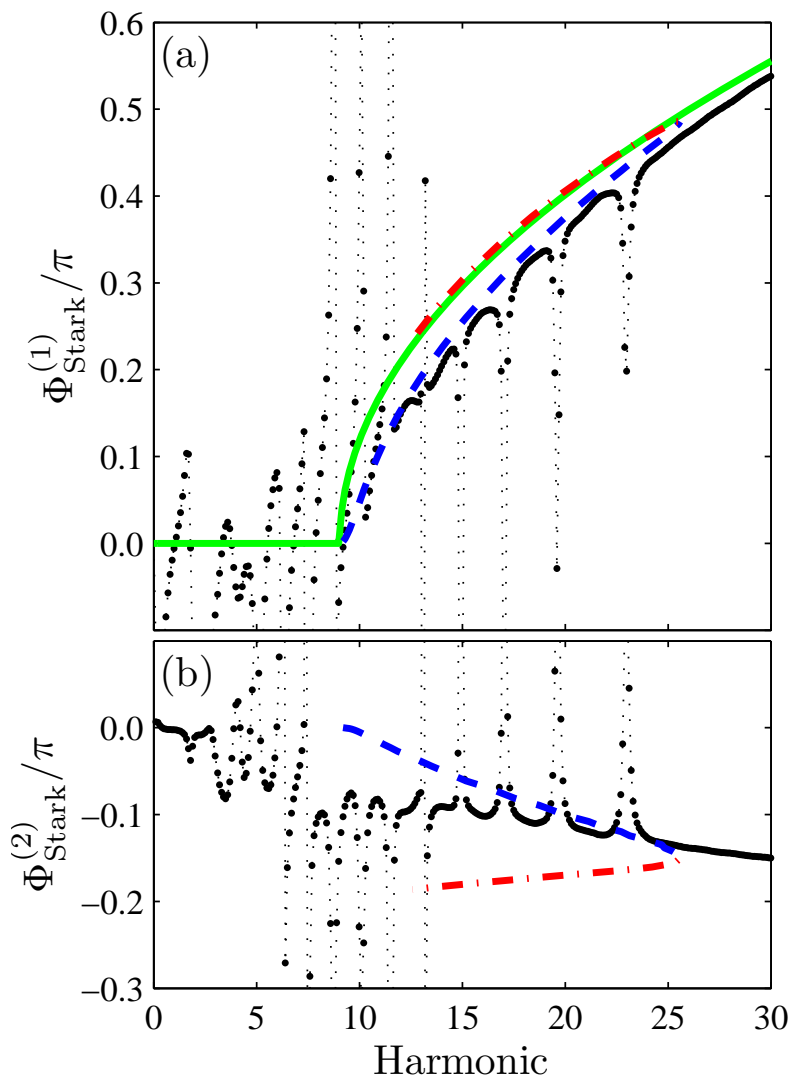


Figure 5.4 | (a) Accumulated first-order Stark phase of CO subject to an ultra short laser pulse. The connected black dots indicate the phase obtained from the Stark-corrected Lewenstein model. The dashed blue curve is the phase predicted from short classical trajectories, and the dash-dotted red curve the phase from long trajectories. The smooth green curve is the analytical model of equation (5.15), with the phase defined to be zero for harmonics below I_p . (b) Accumulated second-order Stark phase. Dashed and dash-dotted curves indicate short and long classical trajectories.

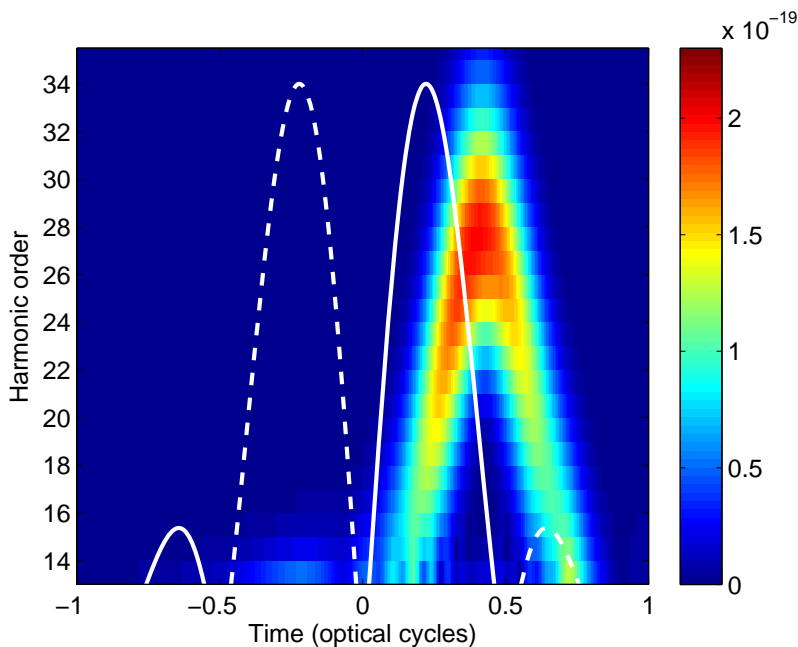


Figure 5.5 | High-harmonic emission times for the HOMO of CO subject to an ultra short laser pulse. The white line indicates the driving field, with the solid line indicating that $F_x(t) > 0$, and the dashed line that $F_x(t) < 0$. The permanent dipole of the HOMO points in the negative x direction.

first- and second-order Stark phases are fairly large, although the first-order Stark phase clearly dominates.

The electric field of the driving pulse has a cosine-squared envelope, and an 800 nm sine carrier wave. The full width at half maximum is only 0.72 times one optical cycle T , corresponding to a full duration of $2T$. The maximum of the electric field is 0.071 au, corresponding to a peak intensity of 2×10^{14} W/cm² of the envelope. The use of such a short driving pulse ensures that there is only one harmonic burst, as seen from the time-profile in figure 5.5.

The phases in figure 5.4 are plotted as a function of harmonic order, while equations (5.9)–(5.11) are formulated in the time-

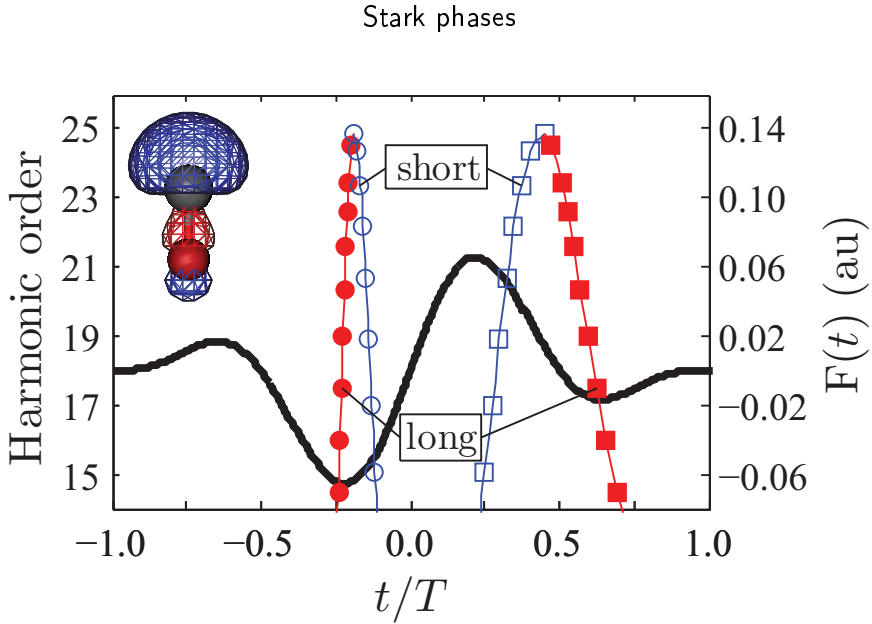


Figure 5.6 | Classical trajectories for CO subject to an ultra short laser pulse, indicated by the solid black curve. Instants of ionization are marked by circles, and instants of recombination by squares. The vertical offset of a trajectory, consisting of a circle and a square, indicates the photon energy of the emitted harmonic, calculated using equation (5.12). Open blue markers indicate short trajectories, and full red markers indicate long trajectories.

domain. We use classical electron trajectories to translate the (t, t') dependence into an ω dependence. Following the three-step model, we assume that a continuum electron is born at the origin with zero velocity at each time t' . We then assume that only the laser field exerts force on the electron, and propagate it forward in time using Newton's second law. If the electron returns to the origin at a later time t , we use energy conservation to calculate the energy of the emitted photon:

$$\omega(t, t') = \frac{1}{2} \dot{\mathbf{r}}^2(t, t') + I_p(\mathbf{F}(t)). \quad (5.12)$$

Here $\dot{\mathbf{r}}(t, t')$ is the velocity at time t of an electron that is detached at the origin with zero velocity at time t' . The result of a classical trajectory calculation is shown in figure 5.6 for the ul-

tra short laser pulse used in figure 5.4. The classical calculation predicts that only one half-cycle contributes to the harmonics, in agreement with the Gabor transform in figure 5.5. The absence of other harmonic bursts ensures that the sign of the first-order Stark phase in equation (5.10) is fixed. Furthermore, it ensures that there are no interferences that have to be dealt with. Together, equation (5.12) and the calculation leading to figure 5.6 provide a map between (t, t') and harmonic frequency.

Figure 5.4(a) shows that short trajectories account for the first-order Stark phase within the limits set by the classical model, which does not account for harmonics below the ionization threshold, nor beyond the harmonic cutoff. The phase spikes coincide with minima in the harmonic plateau, shown in figure 5.7. The minima are caused by the interference between short and long trajectories, and each is associated with a sharp variation in the harmonic phase. The exact position of each minimum changes when the Stark shift is included, which explains the phase spikes.

The first-order Stark phase in equation (5.10) can be interpreted in terms of the integral of the force felt by the continuum electron, showing that it is directly proportional to the return velocity

$$\Phi_{\text{Stark}}^{(1)}(t, t') = \boldsymbol{\mu} \cdot \dot{\mathbf{r}}(t, t'). \quad (5.13)$$

Equation (5.13) reveals that the first-order Stark phase only depends on the return velocity, and the angle φ between the internuclear axis and the laser polarization axis. This surprising result shows that the first-order Stark phase is almost independent of the shape and intensity of the driving pulse that caused it. Insertion into equation (5.12) gives

$$\begin{aligned} \Phi_{\text{Stark}}^{(1)}(t, t') = & \text{sgn}(\boldsymbol{\mu} \cdot \dot{\mathbf{r}}(t, t')) \mu |\cos(\varphi)| \\ & \times \sqrt{2(\omega(t, t') - I_p(\mathbf{F}(t)))}, \end{aligned} \quad (5.14)$$

where $\text{sgn}(\boldsymbol{\mu} \cdot \dot{\mathbf{r}}(t, t'))$ keeps track of the direction with which the returning electron probes the bound state. The return velocity

Stark phases

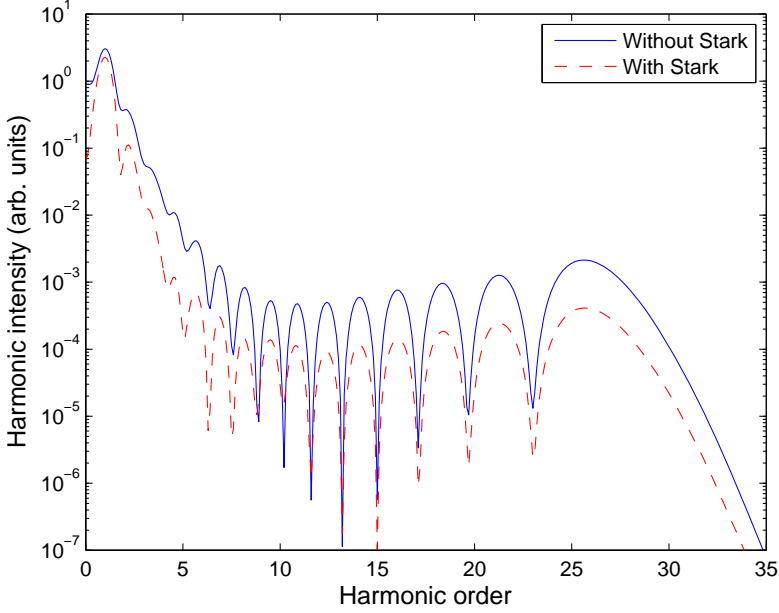


Figure 5.7 | Harmonic spectra for oriented CO subject to an ultra short pulse. Inclusion of the Stark effect lowers the harmonic intensity due to the gating effect illustrated in figure 5.2. The spectrum is smooth because only one half-cycle contributes to the spectrum. The sharp minima are caused by interference between the short and long trajectories. The interference minima shift slightly when the Stark effect is included.

has the opposite sign of the velocity shortly after ionization, so $\text{sgn}(\boldsymbol{\mu} \cdot \dot{\mathbf{r}}(t, t')) = \text{sgn}(\boldsymbol{\mu} \cdot \mathbf{F}(t'))$. The time-dependence of the Stark-shifted ionization potential introduces a small difference between short and long trajectories. If this field-dependence is ignored in the recombination step, then equation (5.14) simplifies to

$$\Phi_{\text{Stark}}^{(1)}(\omega) \approx \pm \mu \cos(\varphi) \sqrt{2(\omega - I_p)}. \quad (5.15)$$

The advantage of equation (5.15) is that it gives an analytical prediction of the first-order Stark phase directly in terms of the

harmonic frequency ω , rather than in terms of electron trajectories through $\omega(t, t')$.

The analytical model of equation (5.15) slightly overestimates the first-order Stark phase in figure 5.4(a) due to the use of the field-free ionization potential. The error is expected to increase with increasing intensity. Figure 5.8 shows the first-order Stark phase calculated with the Lewenstein model, classical trajectories, and equation (5.15) at two additional intensities. Comparing equation (5.15) to the Lewenstein result at the 21st harmonic, we observe an error of 8% (1.5×10^{14} W/cm²), 10% (2.0×10^{14} W/cm²), and 12% (2.5×10^{14} W/cm²). Note how the interference features move with intensity, but the overall square root behavior is the same at all three intensities. The close agreement between equation (5.15) and the long trajectory calculation (the dashed blue line) is due to the extremely narrow pulse envelope, which causes the long trajectories to recombine at low field strengths as shown in figure 5.6.

Unlike the first-order Stark phase, the second-order Stark phase cannot be expressed directly in terms of the harmonic frequency. This is clearly seen in figure 5.4(b), where the trajectory result decreases as a monotonic function of excursion time $t - t'$. The monotonic behaviour can be understood from equation (5.11), where the second-order Stark phase is negatively proportional to $\int_{t'}^t F(t'') dt''$. At the cutoff the short and long trajectories merge, and therefore have the same associated Stark phase.

In reference [88] we relate Stark phases to orbital tomography, where magnitudes and phases of high-harmonics are used to reconstruct the field-free ground state orbital [89–91]. Equation (5.15) is ideally suited to subtract the first-order Stark phase from measurements because it is simple to use and independent of the local peak field strength F_0 of the focused laser beam. As we cannot find a similar equation for the second-order Stark phase, the best we can do is to find experimental conditions that minimize it. The scaling of the second-order Stark phase with respect to laser parameters can be estimated by neglecting the pulse envelope, and integrating equation (5.11) from the peak of a half-cycle

Stark phases

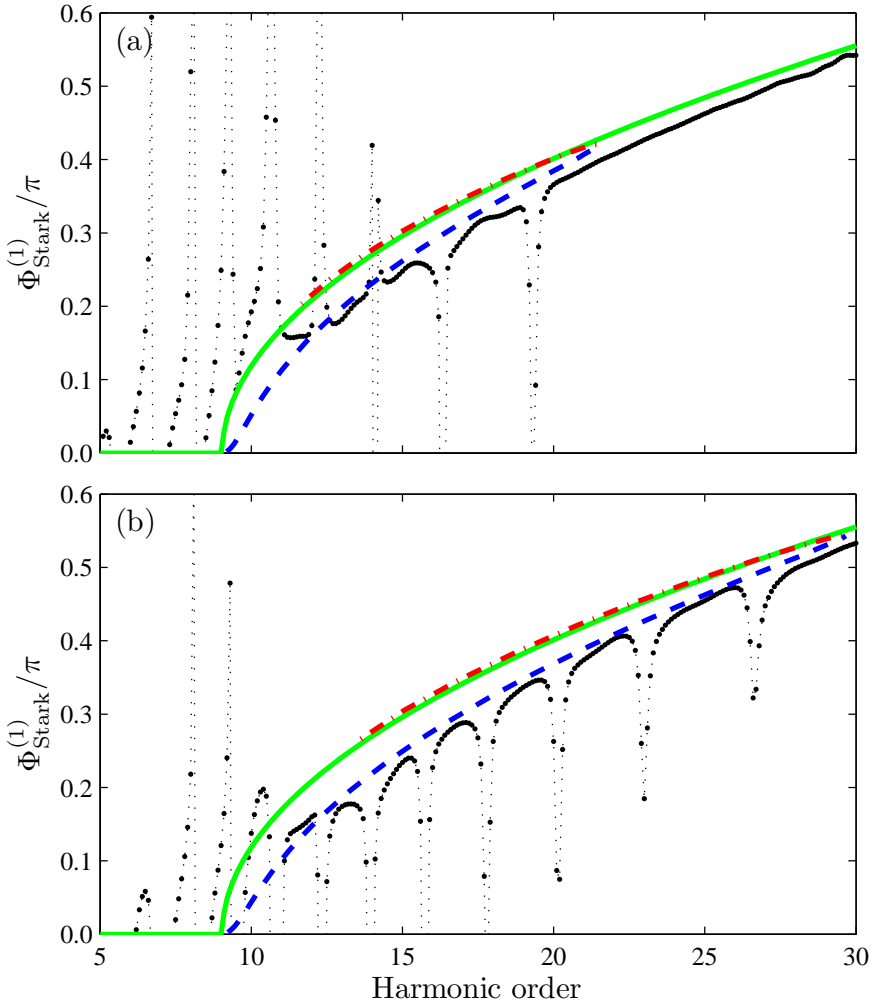


Figure 5.8 | Accumulated first-order Stark phase of CO subject to an ultra short laser pulse with a peak intensity of (a) 1.5×10^{14} W/cm², and (b) 2.5×10^{14} W/cm². The connected black dots indicate the phase obtained from the Stark-corrected Lewenstein model. The dashed blue curve is the phase predicted from short classical trajectories, and the dash-dotted red curve the phase from long trajectories. The smooth green curve is the analytical model of equation (5.15), with the phase defined to be zero for harmonics below I_p .

$t' = t_{\text{peak}}$ up to $t = t_{\text{peak}} + 2T/3$. The cut-off harmonics are then found to accumulate a second-order Stark phase proportional to $F_0^2/\omega_0 = 4\omega_0 U_p$, where ω_0 is the frequency of the driving laser, and U_p the ponderomotive potential. According to the usual cutoff rule, $\omega_{\text{max}} = 3.17U_p + I_p$, the importance of the second-order Stark phase can be reduced by increasing the wave length of the driving laser while keeping the harmonic cutoff fixed. Additionally, figure 5.4(b) shows that selection of the short-trajectory contribution also helps, as short trajectories accumulate a smaller second-order Stark phase.

If multi-cycle pulses are utilized, then each harmonic gets a contribution from trajectories that accumulate opposite Stark phases. In calculations, this can be avoided by artificially restricting ionization to every other half-cycle [92]. Experimentally, the relative weight between the two types of trajectories is determined by the effectiveness of the geometric gating. Figure 5.2 shows that geometric gating is expected to be fairly weak in CO.

Of perhaps greater interest is the case of aligned molecules. Again the crucial characteristic is the effectiveness of geometric gating, which can be partially enforced by using an ultra short driving pulse. Figure 5.9(a) shows the total (first- and second-order) Stark phase for oriented CO submitted to the pulse from before. There seems to be better agreement with the long trajectories than for the purely single-order Stark phase. For comparison, figure 5.9(b) shows a plot of the total Stark phase from aligned CO, calculated by adding the spectra of oppositely oriented CO molecules according to equation (2.25). Had it not been for geometric gating, then the Stark phase would have been dominated by the second-order Stark shift, and the result would have resembled that in figure 5.4(b). Instead, there is a clear signature of the first-order Stark phase. The sign of the Stark phase changes if the carrier envelope phase delay of the driving pulse is changed by π .

Inspired by the above findings, we expect that high-harmonic phases will provide the clearest indication of the validity of the Stark-corrected Lewenstein model. The experiment should be

Stark phases

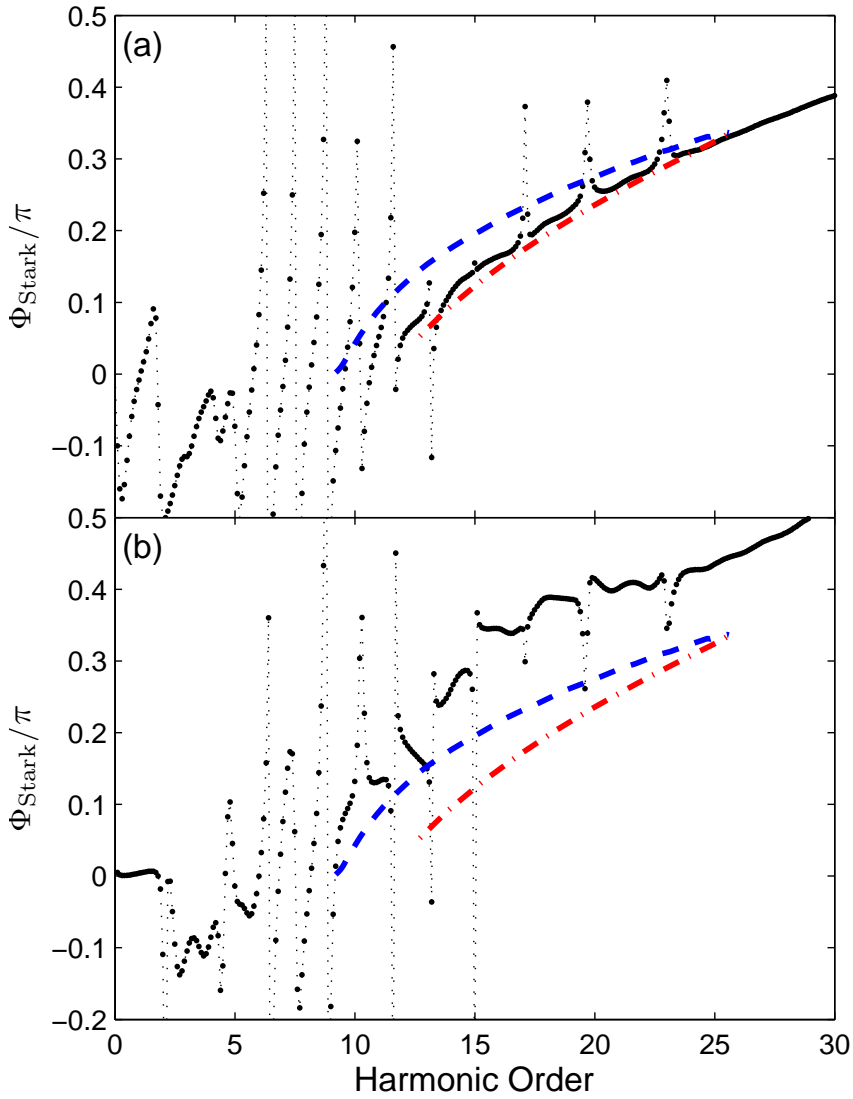


Figure 5.9 | Total accumulated Stark phase of (a) oriented CO, and (b) aligned CO. Dashed and dash-dotted curves indicate short and long classical trajectories.

performed on aligned polar molecules using ultra short driving pulses. When the ponderomotive phase, and possibly also the ionization phase, has been subtracted, the result should resemble a square root as a function of harmonic order, and reverse its sign when the carrier envelope phase of the driving laser is changed by π . There are two main experimental methods for extracting harmonic phases: Resolution of attosecond beating by interference of two photon transitions (RABBITT) [93, 94], and interference with harmonics generated in a reference gas [95, 96].

Two-centre interference

There are two main philosophies within the HHG community. One sees HHG as a light source capable of delivering coherent radiation reaching into the XUV range, and focuses on maximizing the harmonic yield and band width. The other school of thought sees HHG, as well as other strong-field phenomena, as a probe of ultra fast dynamics. The most robust structure information related to HHG is the so-called two-centre interference minimum [69, 97]. As the most prominent spectral feature in symmetric molecules, the two-centre interference minimum has become the prime example of HHG structure retrieval. In this chapter we will review the basic concepts, and then extend them to polar molecules.

6.1 Basic concepts

According to the Lewenstein model, the high-harmonic spectrum is given by the Fourier transform of the time-dependent dipole velocity

$$\langle \hat{\mathbf{v}}_{\text{dip}}(t) \rangle \approx i \int_{t_0}^t dt' \int_{\mathbb{R}^3} d\mathbf{k} \mathbf{v}_{\text{rec}}^*(\mathbf{k} + \mathbf{A}(t)) e^{-iS(\mathbf{k}, t, t')} \times \mathbf{F}(t') \cdot \mathbf{d}_{\text{ion}}(\mathbf{k} + \mathbf{A}(t')) \quad (6.1)$$

$$+ \text{complex conjugate.} \quad (6.2)$$

Inspired by the three-step model, we now search for a kinetic momentum \mathbf{k} (or a molecular orientation) at which the recombination matrix element vanishes. The corresponding high-harmonic frequency $\omega = \frac{1}{2}|\mathbf{k}|^2 + I_p$ is then expected to be suppressed in the final harmonic spectrum, irrespective of the ionization and propagation steps. Predicting the position of a two-centre interference thus reduces to analyzing the recombination matrix element [69].

We fix two of the Euler angles ($\theta = 90^\circ$ and $\chi = 0^\circ$) and vary φ . This means that the molecule is restricted to the xy plane. We keep the laser polarization axis along the x axis, so φ is the angle between the internuclear axis and the laser polarization axis. The oriented HOMO $|\psi, \varphi\rangle$ is now expanded as a linear combination of atomic orbitals (LCAO):

$$|\psi, \varphi\rangle = \sum_{n=1}^{N_a} c_n |\phi_n, \varphi\rangle. \quad (6.3)$$

The sum is over atomic centres. The recombination dipole velocity matrix element between $|\psi, \varphi\rangle$ and a plane wave $|\mathbf{k}\rangle$ then

takes the form

$$\langle \mathbf{k} | \hat{\mathbf{v}}_{\text{dip}} | \psi, \varphi \rangle = \int_{\mathbb{R}^3} \psi_{\mathbf{k}}^*(\mathbf{r}) \hat{\mathbf{v}}_{\text{dip}} \psi(\varphi; \mathbf{r}) d\mathbf{r} \quad (6.4)$$

$$= \int_{\mathbb{R}^3} \psi_{\mathbf{k}}^*(\mathbf{r}) \hat{\mathbf{v}}_{\text{dip}} \sum_{n=1}^{N_a} c_n \phi_n(\varphi; \mathbf{r} - \mathbf{R}_n) d\mathbf{r} \quad (6.5)$$

$$= \sum_{n=1}^{N_a} c_n \int_{\mathbb{R}^3} e^{i\mathbf{k}\cdot\mathbf{r}} \hat{\mathbf{v}}_{\text{dip}} \phi_n(\varphi; \mathbf{r} - \mathbf{R}_n) d\mathbf{r} \quad (6.6)$$

$$= \sum_{n=1}^{N_a} c_n e^{i\mathbf{k}\cdot\mathbf{R}_n} \int_{\mathbb{R}^3} e^{i\mathbf{k}\cdot\mathbf{r}} \hat{\mathbf{v}}_{\text{dip}} \phi_n(\varphi; \mathbf{r}) d\mathbf{r} \quad (6.7)$$

$$= \sum_{n=1}^{N_a} e^{i\mathbf{k}\cdot\mathbf{R}_n} c_n \langle \mathbf{k} | \hat{\mathbf{v}}_{\text{dip}} | \phi_n, \varphi \rangle \quad (6.8)$$

$$= \sum_{n=1}^{N_a} e^{i(\mathbf{k}\cdot\mathbf{R}_n + \vartheta_n(\mathbf{k}, \varphi))} |c_n \langle \mathbf{k} | \hat{\mathbf{v}}_{\text{dip}} | \phi_n, \varphi \rangle|. \quad (6.9)$$

The phase $\mathbf{k}\cdot\mathbf{R}_n$ is due to the atomic position \mathbf{R}_n , and $\vartheta_n(\mathbf{k}, \varphi)$ is an intrinsic recombination phase relating to the LCAO centered on atom n . Equation (6.9) shows that the harmonic emission from different atoms interfere, causing maximal destructive interference at a particular momentum \mathbf{k} for a fixed angle φ .

In the special case of diatomic molecules with molecular orbitals of purely even or odd parity,

$$\psi(\varphi; \mathbf{r}) = c_1 \phi_1(\varphi; \mathbf{r} - \mathbf{R}_1) \pm c_1 \phi_1(\varphi; \mathbf{r} - \mathbf{R}_2), \quad (6.10)$$

with plus for even parity and minus for odd parity. Equation (6.8) therefore simplifies to

$$\langle \mathbf{k} | \hat{\mathbf{v}}_{\text{dip}} | \psi, \varphi \rangle = [e^{i\mathbf{k}\cdot\mathbf{R}_1} \pm e^{i\mathbf{k}\cdot\mathbf{R}_2}] c_1 \langle \mathbf{k} | \hat{\mathbf{v}}_{\text{dip}} | \phi_1, \varphi \rangle \quad (6.11)$$

$$= [1 \pm e^{i\mathbf{k}\cdot\mathbf{R}}] e^{i\mathbf{k}\cdot\mathbf{R}_1} c_1 \langle \mathbf{k} | \hat{\mathbf{v}}_{\text{dip}} | \phi_1, \varphi \rangle, \quad (6.12)$$

where $\mathbf{R} = \mathbf{R}_2 - \mathbf{R}_1$. Equation (6.12) is equal to zero when

$$\mathbf{k} \cdot \mathbf{R} = (2m + 1)\pi \quad (\text{even parity}) \quad (6.13)$$

$$\mathbf{k} \cdot \mathbf{R} = (2m)\pi \quad (\text{odd parity}) \quad (6.14)$$

for any integer m . Rewriting in terms of the de Broglie wave length $\lambda_e = \frac{2\pi}{|\mathbf{k}|}$, and assuming that the returning electron is moving parallel to the polarization axis of the driving laser, we get destructive interference when

$$R \cos(\varphi) = \frac{2m+1}{2} \lambda_e \quad (\text{even parity}) \quad (6.15)$$

$$R \cos(\varphi) = m \lambda_e \quad (\text{odd parity}). \quad (6.16)$$

Similar equations can be derived for constructive interference

$$R \cos(\varphi) = m \lambda_e \quad (\text{even parity}) \quad (6.17)$$

$$R \cos(\varphi) = \frac{2m+1}{2} \lambda_e \quad (\text{odd parity}), \quad (6.18)$$

but a factor two enhancement is not as easy to identify in spectra as a near-perfect cancellation. Typically only the $m = 0$ interference minimum is seen due to the limited harmonic plateau.

In our implementation of the Lewenstein model, the assumption that the continuum electron moves parallel to the polarization of the driving laser is the same as neglecting the drift momentum in equation (2.41). As mentioned in section 3.1, the drift momentum has a negligible influence on the parallel component of the harmonics, so the approximation is valid for the parallel component. The perpendicular component, on the other hand, vanishes identically if the drift momentum is omitted. Equations (6.15)–(6.16) are therefore expected to fail for the perpendicular component. We will restrict our attention to the parallel component in the following discussion, as the parallel component completely dominates the total harmonic emission.

The physical interpretation of equations (6.15)–(6.16) is very clear. Harmonic generation is suppressed when the returning electron has a de Broglie wave length such that the travel phase acquired between the nuclei ensures destructive interference. This is often compared to Young's double slit experiment. A perhaps better analogue is that of a two-point emitter. Depending on the (projected) distance between the emitters and their relative

phase, certain emission frequencies will cancel in the observation direction.

The HOMOs of H_2 , H_2^+ , and CO_2 have pure symmetries, allowing the prediction of equations (6.15)–(6.16) to be applied directly. Good agreement is reached when comparing to theoretical calculations that restrict themselves to the HOMO contribution. The exact role of the HOMO–1, HOMO–2, and excited states in experiment remains an open question, however [25–31, 71, 98].

Even though some experimentally relevant molecules, like N_2 , have HOMOs of mixed symmetry, equations (6.15)–(6.16) can still be used as a reference point to understand the physics. The even components of the HOMO will give a contribution to the total HHG spectrum that has a minimum predicted by equation (6.15). The odd components of the HOMO will give a contribution with a minimum predicted by equation (6.16). Depending on the relative strength and phase of the two contributions, an interference minimum may or may not appear in the HHG spectrum. Two-centre interference minima in orbitals of mixed symmetry has been covered in great detail in references [76, 99, 100].

There is some amount of controversy regarding the correct way of translating a de Broglie wave length into the corresponding high-harmonic order. The problem relates to the influence of the Coulomb potential, which should change the wave length of the returning electron depending on its position relative to the nuclei. The naive approach followed here is inspired by the three-step model, and assumes energy conservation in the recombination step:

$$\omega = \frac{1}{2} \left(\frac{2\pi}{\lambda_e} \right)^2 + I_p. \quad (6.19)$$

Using an 800 nm laser, $I_p/\omega_0 = 9.0$ for CO , and $I_p/\omega_0 = 10.1$ for N_2 . Others argue that I_p should be omitted. For a treatment where the energy gain depends on the trajectory of the returning electron, see references [29, 101].

Two-centre interference has been observed both theoretically and experimentally in HHG from H_2 [38, 69], and theoretically in

above-threshold ionization (ATI) from CO [87]. In high-energy above-threshold ionization (HATI), two-centre interference has been observed theoretically for N_2 [102, 103], and theoretically and experimentally for O_2 [103, 104].

Another mechanism for interference minima in HHG are the so-called dynamic minima [25, 98], also referred to as multi-channel minima. In contrast to the structural minima discussed above, dynamic minima depend on laser parameters such as wave length and intensity. This can be understood in a single-active electron picture, where two or more independent channels contribute coherently to the total spectrum. Changes in the driving pulse introduce different relative phases between different channels, which modifies the position of a potential interference minimum. The issue is still debated, but it is very likely that the interference minimum in CO_2 is partly structural [27–30], and partly dynamic [25, 26, 71]. Another variant of this is the interference from excited states, which has been studied for H_2^+ using the TDSE [31].

The interference minimum in N_2 changes very little with changing intensity and wave length of the driving laser, but also does not shift noticeably with alignment angle [71]. As we saw in chapter 3, Lewenstein calculations performed on just the HOMO channel gives a minimum which does move with alignment angle. It has been suggested that the interference minimum in N_2 is similar to the so-called Cooper minimum in Ar [72, 73], which cannot be described using plane waves [72].

6.2 Oriented polar molecules

In polar molecules we do not have the luxury of equal atomic orbitals on the different nuclei, so we cannot get a simple condition like equation (6.12). Instead we have to find minima of equation (6.9). Two things are immediately clear. First, as the different nuclear centres do not have equal orbitals, we can no longer expect to find a momentum \mathbf{k} that gives perfect cancel-

Oriented polar molecules

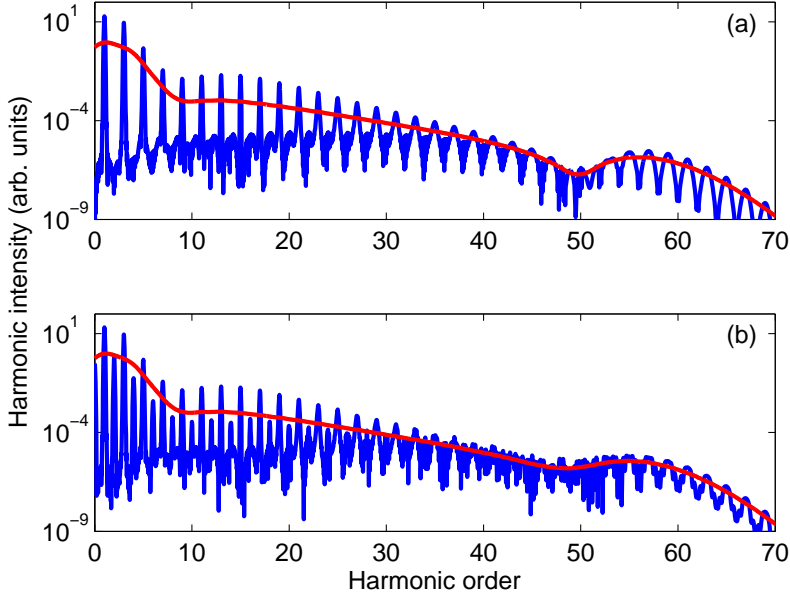


Figure 6.1 | Parallel components of HHG spectra from CO oriented at (a) $\varphi = 90^\circ$ and (b) $\varphi = 86^\circ$ to the laser polarization axis. The smooth red curves are obtained by averaging the spectra over several harmonic orders. The 800 nm driving laser pulse has a peak intensity of 4×10^{14} W/cm², and a cosine squared envelope with ten optical cycles FWHM. Short trajectories are selected using a window function, and the Stark effect is not included.

lation [100]. Second, the intrinsic recombination phases $\vartheta_n(\mathbf{k}, \varphi)$ now have different \mathbf{k} -dependencies that have to be accounted for [100, 105]. In the two-centre emitter picture the two emitters now have different (\mathbf{k} -dependent) emission strengths, and their relative phase depends on \mathbf{k} . An interesting consequence of this is that one can expect to observe two-centre interference minima when the molecular axis is perpendicular to the polarization axis of the driving laser, as is the case in figure 6.1.

It is usually assumed that two-centre interference minima are completely determined by the recombination step into the ground

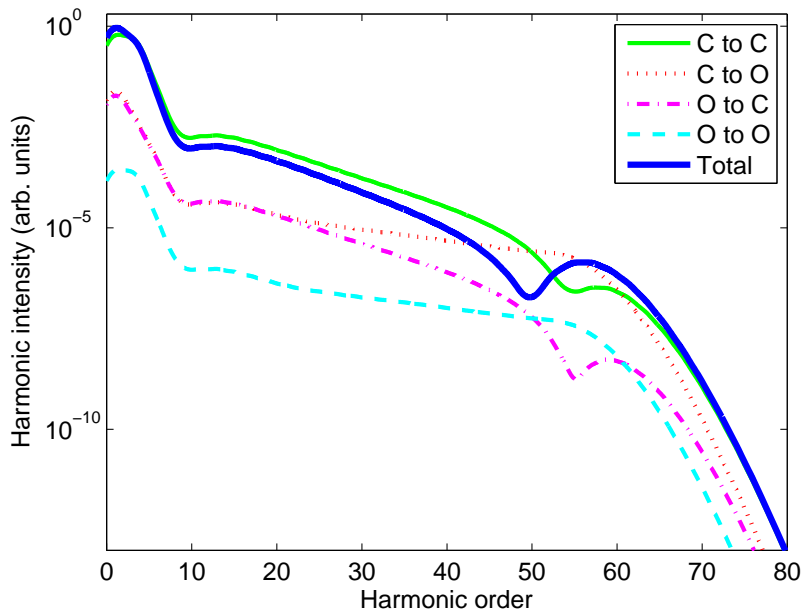


Figure 6.2 | Smoothed parallel components of the spectra associated with the four trajectories of CO oriented perpendicular to the laser polarization axis. The molecular spectrum is the coherent sum of all four contributions, and is dominated by trajectories that start with ionization at C. Short trajectories are selected, and the Stark effect is not included.

state orbital. This assumption needs to be justified for polar molecules due to the different classes of electron trajectories in the continuum [51, 106]. There are four different trajectories for CO, each one starting at either C or O, and recombining at either C or O. The contribution from each class of trajectory is plotted in figure 6.2 for CO oriented perpendicular to the laser polarization axis. Trajectories starting at C completely dominate the spectrum due to a larger ionization dipole matrix element at C. Removing the trajectories starting at O has very little impact on the shape and position of the interference minimum, showing that the interference is not caused by the ionization step.

The trajectory contributions in figure 6.2 are obtained using the multi-centre stationary-phase approximation described in section 2.3. In this approximation trajectories going from one atom to another acquire an extra component to the momentum. Using the atomic stationary-phase approximation, and thus neglecting this drift momentum, has a negligible effect on the shape and position of the interference minimum. Also, short trajectories have been selected using a window function, ruling out interference between long and short trajectories. These observations show that continuum dynamics are not responsible for the interference minimum either.

The following example illustrates the importance of including the recombination strengths when predicting two-centre interference minima from polar molecules. Figure 6.3 shows the relevant recombination dipole velocity matrix elements for CO oriented at $\varphi = 86^\circ$. The full blue curves are the norm and the phase of the total HOMO matrix element of CO. The dashed green curves are the norm and phase of the matrix element of the LCAO on C, and the dash-dotted magenta curves on O. If we were to neglect the \mathbf{k} -dependence of the individual recombination strengths, then we would predict a minimum in the total recombination norm when

$$|\mathbf{k}|R \cos(\varphi) + \vartheta_2(\mathbf{k}, \varphi) - \vartheta_1(\mathbf{k}, \varphi) = (2m + 1)\pi. \quad (6.20)$$

This predicts the minimum to be at $|\mathbf{k}| = 1.86$ au, which is in poor agreement with the actual position of $|\mathbf{k}| = 2.08$ au in figure 6.3(a). The reason is clearly that the atomic recombination strengths at $|\mathbf{k}| = 1.86$ au are too different for a strong interference minimum, even though the two contributions are completely out of phase.

6.3 Aligned polar molecules

As discussed in section 2.2, perfectly oriented molecules are not currently available for HHG experiments. However, an increasing amount of strong-field experiments are being performed on

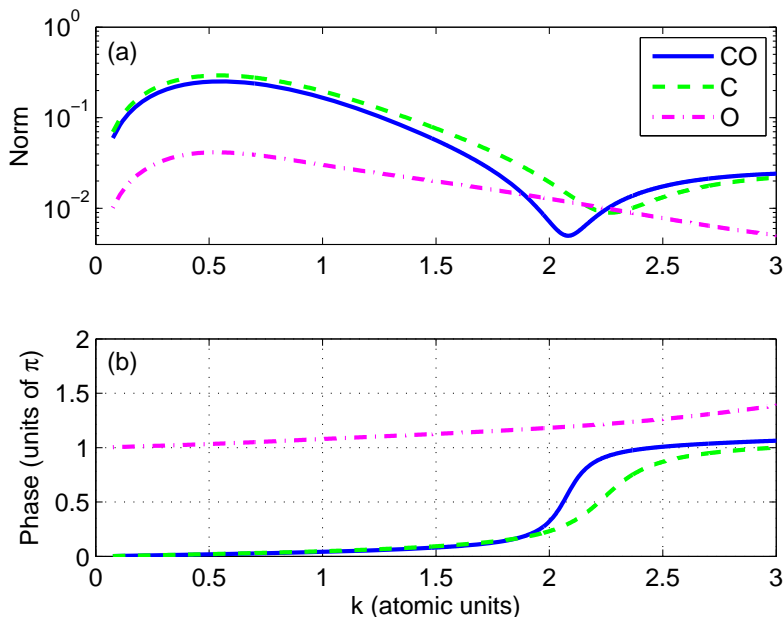


Figure 6.3 | (a) Norms of the dipole velocity matrix elements for CO oriented at $\varphi = 86^\circ$ to \mathbf{k} . The full blue curve is the matrix element with the entire HOMO ($\langle \mathbf{k} | \hat{\mathbf{v}}_{\text{dip}} | \psi, 86^\circ \rangle$), the dashed green curve is the matrix element with the LCAO on C ($\langle \mathbf{k} | \hat{\mathbf{v}}_{\text{dip}} | \phi_1, 86^\circ \rangle$), and the dash-dotted magenta the matrix element with the LCAO on O ($\langle \mathbf{k} | \hat{\mathbf{v}}_{\text{dip}} | \phi_2, 86^\circ \rangle$). (b) Phases of the same matrix elements. The dashed and dash-dotted curves are given by $\mathbf{k} \cdot \mathbf{R}_n + \vartheta_n(\mathbf{k}, \varphi)$.

aligned polar molecules. Figure 6.4 shows that not only does the two-centre interference survive alignment, but it is also stronger than in the oriented case. The key to understanding the interference in aligned polar molecules is to realize that the dipole velocity matrix elements of opposite orientations are closely related. In our coordinate system the laser polarization is along the x axis, and the molecular axis is confined to the xy plane. Flipping the orientation of the molecule is therefore the same as adding π to φ . All molecular orbitals can be chosen to be real, and either

Aligned polar molecules

even or odd in z . Orbitals that are odd in z do not contribute to the total HHG spectrum [21], which leaves orbitals for which adding π to φ is the same as replacing the wave function with $\psi(\varphi; -x, -y, z) = \psi(\varphi; -x, -y, -z)$. The recombination matrix element of the flipped molecule is

$$\langle \mathbf{k} | \hat{\mathbf{v}}_{\text{dip}} | \psi, \varphi + \pi \rangle = \mathbf{k} \nabla_{\mathbf{k}} \tilde{\psi}(\varphi + \pi; \mathbf{k}) \quad (6.21)$$

$$= \mathbf{k} \nabla_{\mathbf{k}} \tilde{\psi}(\varphi; -\mathbf{k}) \quad (6.22)$$

$$= \mathbf{k} \nabla_{\mathbf{k}} \tilde{\psi}^*(\varphi; \mathbf{k}) \quad (6.23)$$

$$= \langle \mathbf{k} | \hat{\mathbf{v}}_{\text{dip}} | \psi, \varphi \rangle^*, \quad (6.24)$$

where $\tilde{\psi}(\varphi; \mathbf{k})$ is the Fourier transform of the ground state wave function.

Together, equations (2.25), (6.9) and (6.24) show that the recombination dipole velocity matrix element of an aligned molecule is given by

$$\langle \mathbf{k} | \hat{\mathbf{v}}_{\text{dip}} | \psi, \varphi \rangle_{\text{aligned}} = \text{Re} (\langle \mathbf{k} | \hat{\mathbf{v}}_{\text{dip}} | \psi, \varphi \rangle) \quad (6.25)$$

$$= \sum_{n=1}^{N_a} \cos(\mathbf{k} \cdot \mathbf{R}_n + \vartheta_n(\mathbf{k}, \varphi)) \times |c_n \langle \mathbf{k} | \hat{\mathbf{v}}_{\text{dip}} | \phi_n, \varphi \rangle|. \quad (6.26)$$

The position of the two-centre minimum is determined by the value of \mathbf{k} that minimizes the absolute value of equation (6.26). The simplest approach would be to ignore the recombination strengths $|c_n \langle \mathbf{k} | \hat{\mathbf{v}}_{\text{dip}} | \phi_n, \varphi \rangle|$, and claim that harmonic emission from one atom cancels out the harmonic emission from another when

$$|\mathbf{k}|R \cos(\varphi) + \vartheta_2(\mathbf{k}, \varphi) - \vartheta_1(\mathbf{k}, \varphi) = (2m + 1)\pi \quad (6.27)$$

for any integer m . The same result was obtained in equation (6.20) when we ignored the recombination strengths for oriented molecules. However, we saw in section 6.2 that this is a very bad

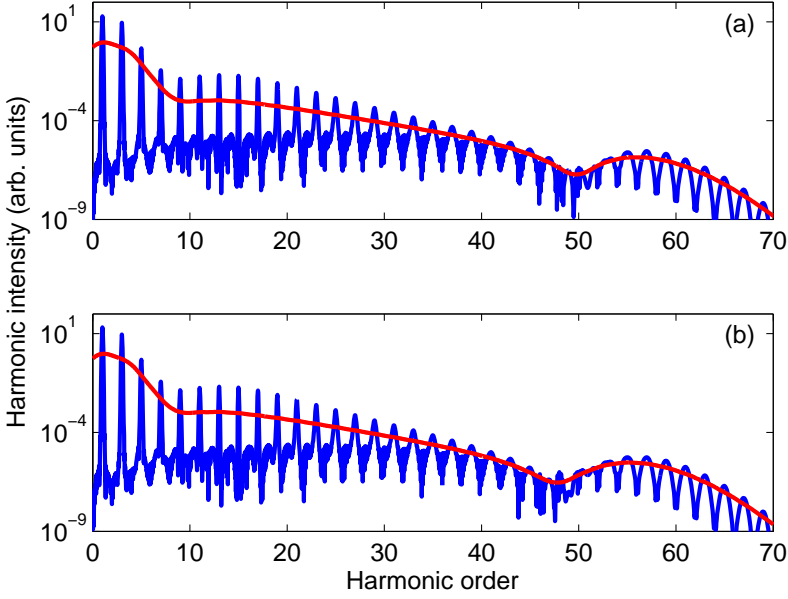


Figure 6.4 | Parallel components of HHG spectra from CO *aligned* at (a) $\varphi = 90^\circ$ and (b) $\varphi = 86^\circ$ to the laser polarization axis. All other parameters are the same as those in figure 6.1.

approximation for oriented polar molecules. There is no reason that it should work better for aligned polar molecules.

An alternative interpretation allows for a better prediction. Rather than as an interference between different atomic species, the interference minimum in aligned polar molecules can be thought of as an interference between opposite orientations. Equation (6.25) then shows that the interference minimum appears whenever the real part of the recombination matrix element of the *oriented* molecular orbital $\langle \mathbf{k} | \hat{\mathbf{v}}_{\text{dip}} | \psi, \varphi \rangle$ is zero:

$$\text{Re}(\langle \mathbf{k} | \hat{\mathbf{v}}_{\text{dip}} | \psi, \varphi \rangle) = 0. \quad (6.28)$$

According to the CO phase in figure 6.3(b), this happens at $|\mathbf{k}| = 2.06$ au. Using the relation $\omega = 0.5|\mathbf{k}|^2 + I_p$ to convert into

photon energy, this corresponds to a minimum at $\omega = 46.3\omega_0$. The actual position of the minimum is $47.8\omega_0$, as determined by the averaged spectrum in figure 6.4(a). For comparison, equation (6.27) predicts the minimum position to be $37.5\omega_0$. Equation (6.28) is clearly more precise at predicting the minimum position than equation (6.27).

Now we are also able to understand why the interference minimum is stronger for aligned CO in figure 6.4(b) than for oriented CO in figure 6.1(b). The strength of the interference minimum in oriented CO is determined by the minimal value of the matrix element norm. As illustrated in figure 6.3, this minimal value is not necessarily zero. For aligned CO only the real part has to be zero, which *is* obtained exactly, hence two-centre interference minima are generally expected to be stronger for aligned than for oriented polar molecules.

Equation (6.28) is more precise than equation (6.27) because no assumptions are made on the recombination strengths at different atomic centres. One might argue that it would be more natural to use equation (6.26) directly, and read off the minimum in the matrix element norm of the *aligned* molecule rather than focus on the matrix element phase of the *oriented* molecule. However, we will show in section 6.4 that the influence of the Stark effect on the minimum position is more easily understood in terms of the recombination phase of the oriented molecule.

Before we go on, it should be noted that the HOMO-1 is expected to contribute significantly to the harmonic spectrum at near-perpendicular orientation angles [107]. The three highest occupied molecular orbitals of CO are sketched in figure 6.5. The result of calculating the HOMO, HOMO-1, and HOMO-2 contributions independently is shown in figure 6.6, where the total signal is dominated by the HOMO-1 channel. This indicates that while our theory is applicable to all molecules, care should be made to find a system or geometry that avoids the influence of lower-lying orbitals. One possibility would be to align CO parallel to the laser polarization, in which case the HOMO-1 channel is suppressed due to its symmetry [21]. This would require

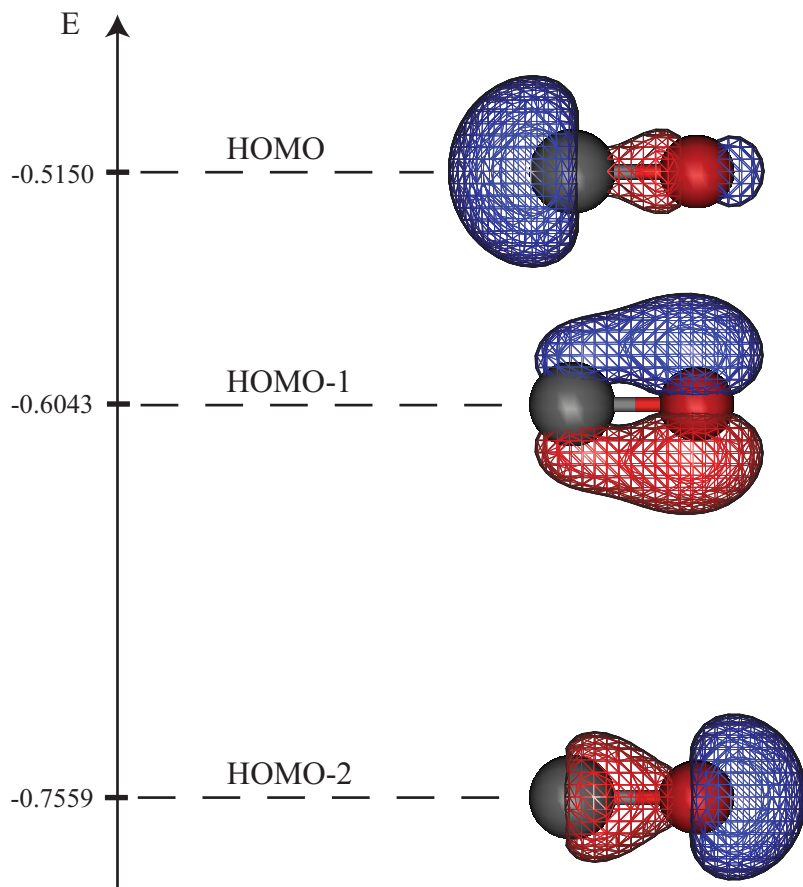


Figure 6.5 | The three highest occupied molecular orbitals of CO. The HOMO-1 is degenerate, with the other orbital being identical, but rotated by 90° around the internuclear axis.

Importance of Stark phases

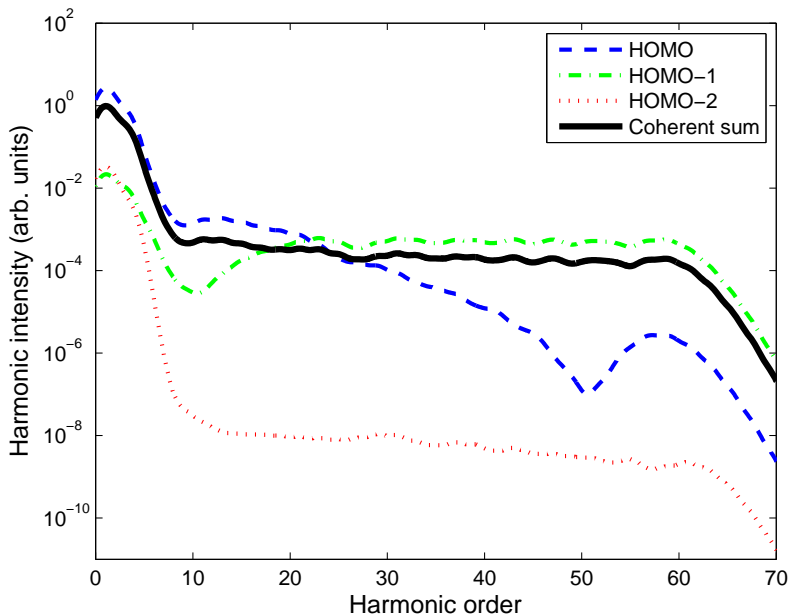


Figure 6.6 | Smoothed harmonic spectra from the HOMO, HOMO-1, and HOMO-2 channels of CO oriented perpendicular to the polarization axis of the same driving pulse as in figure 6.1. The coherent sum is seen to be dominated by the HOMO-1 channel. Stark shifts are not included.

a mid-infrared driving laser in order to include the interference minimum in the plateau.

6.4 Importance of Stark phases

Equation (6.28) shows that the interference minimum from an aligned polar molecule is expected to depend on the phase of the recombination matrix element of the *oriented* molecule. This begs the question whether phases from other steps of the HHG process influence the final position of the minimum.

One possible concern is the potential-energy shift related to

the use of the length gauge for the laser-electron interaction Hamiltonian [51, 106]. However, this potential-energy shift is mostly relevant at large internuclear distances [51]. Examples of the sub-cycle dynamics of the harmonic emission from CO oriented parallel to the laser polarization are shown in figures 4.2 and 5.2. If the choice of gauge were important, then the relative emission strength between neighbouring half-cycles would change when the molecule is flipped. The reason for this asymmetry is that the origin is placed in the centre of mass, so the nuclei have different distances to the origin. We do not observe such a change in our calculations, indicating that the potential-energy shift is not an issue for CO.

Another possible phase is due to the Stark shift felt by the polar HOMO. Figure 6.7 shows the position of the interference minimum in aligned CO calculated using the Lewenstein model. Including the Stark effect to first order is seen to shift the interference minimum by as much as three harmonic orders. Including the second-order Stark shift has negligible influence on the present spectra.

We propose that the shift of the interference minimum can be understood in terms of the first-order Stark phase

$$\Phi_{\text{Stark}}^{(1)} = \int_{t'}^t \boldsymbol{\mu} \cdot \mathbf{F}(t'') dt'' \quad (6.29)$$

that the polar HOMO picks up due to the driving pulse. The accumulated Stark phase can be estimated using classical trajectories of a single half-cycle as in chapter 5.3. This results in the characteristic square-root behaviour. However, it is not immediately clear that this estimate is relevant for multi-cycle driving fields. For comparison we plot the phase obtained by calculating the harmonic spectra from oriented CO with and without including the Stark effect. As neighbouring half-cycles experience opposite signs of the first-order Stark shift, we restrict the ionization step to times t' at which the x component of the electric field $\mathbf{F}(t')$ is positive. This singles out continuum trajectories that share the same sign of the Stark shift. Short trajectories

Importance of Stark phases

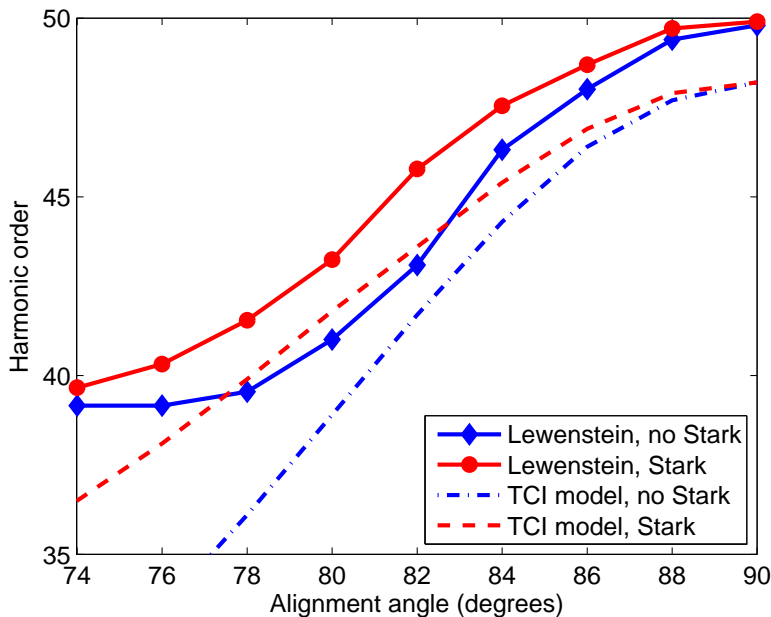


Figure 6.7 | Position of the interference minimum (of the smoothed spectrum) from aligned CO with and without including the Stark effect in the Lewenstein model. Short trajectories have been selected. Also plotted are the predicted minima positions using a two-centre interference (TCI) model based on equation (6.28)

are selected using a window function. The difference in harmonic phase between the two calculations is plotted in figure 6.8 as an irregular blue curve. The agreement with equation (6.29) is quite good.

The amount by which the Stark effect shifts the interference minimum can be estimated using equations (6.28) and (6.29). The interference minimum appears at the momentum $|\mathbf{k}|$ where the real part of the recombination matrix element is zero. For CO oriented at $\varphi = 86^\circ$ in figure 6.3(b), this happens at $|\mathbf{k}| = 2.06$ au, corresponding to $\omega = 46.3\omega_0$. The accumulated phase from equation (6.29) is on the order of 0.05π , which is enough to

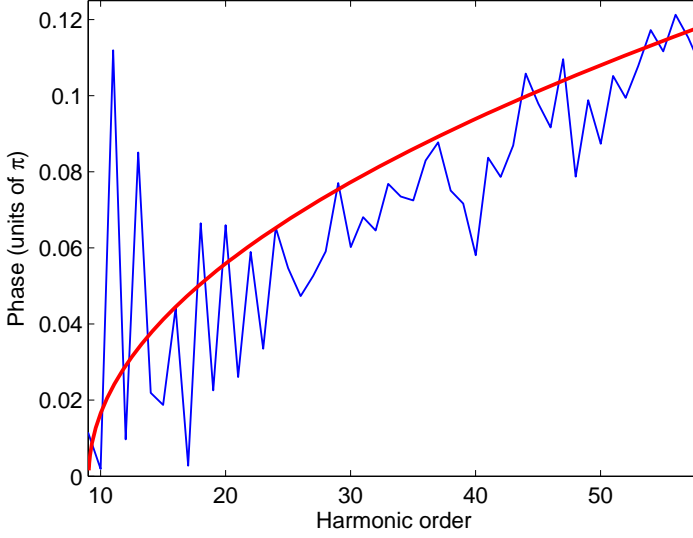


Figure 6.8 | Estimates of the Stark phase accumulated in the continuum for CO oriented at $\varphi = 82^\circ$, and using the pulse parameters from figure 6.1. The smooth red curve is calculated from equation (6.29) based on classical trajectories to map ionization and recombination times to harmonic order. The irregular blue curve is the phase difference between harmonics calculated with and without including the Stark effect in the Lewenstein model. To avoid cancellation from neighbouring half-cycles, ionization is artificially restricted to every other half-cycle.

shift the interference condition to $|\mathbf{k}| = 2.08$ au, corresponding to $\omega = 47.0\omega_0$. When φ is decreased, the phase shift increases due to the $\cos(\varphi)$ scaling in equation (6.29).

Combining equations (6.28) and (6.29) gives the two-centre interference predictions plotted in figure 6.7. At perpendicular alignment the first-order Stark shift is exactly zero, and the minima coincide. The two-centre model is seen to be off by two harmonic orders as compared with the Lewenstein calculations. As the alignment angle is decreased, the two-centre interference model adequately describes the shift of the minimum, down to

Importance of Stark phases

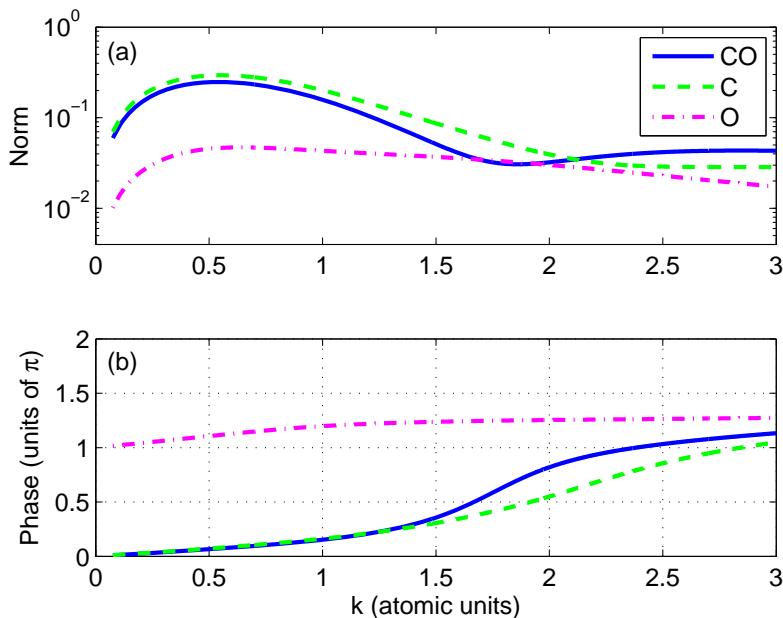


Figure 6.9 | Same as figure 6.3, but with $\varphi = 76^\circ$.

about $\varphi = 80^\circ$, after which the Lewenstein minimum washes out and finally vanishes.

The weakening of the interference minimum is not caused by interfering trajectories, as the long trajectories have been filtered out using a window function. A possible explanation is that the total recombination dipole velocity matrix element has a slower phase variation at smaller alignment angles, illustrated in figure 6.9(b) as a full blue curve for $\varphi = 76^\circ$. One might have expected the phase variation to be faster, due to the larger contribution from the geometric phase $\mathbf{k} \cdot \mathbf{R}_n$, but the total phase is dominated by the behaviour of the matrix element on C, which has a slower π phase change at smaller alignment angles.

Macroscopic phase-matching

As mentioned at the beginning of section 2.1, a full understanding of HHG requires modelling on both the microscopic and macroscopic scale. In chapters 2–6 we have studied several single-molecule effects, such as elliptically polarized harmonics, ionization gating, Stark phases, and two-centre interference minima. In this chapter we will briefly review how to extend our treatment to a macroscopic gas of molecules, and then discuss unique aspects of macroscopic phase-matching for polar molecules. Unlike the rest of the thesis, this chapter contains several formulas in SI units. As a rule of thumb, all propagation equations are in SI units, while all single-molecule quantities are kept in atomic units to be consistent with previous chapters.

7.1 Propagation equations

When calculating HHG from a macroscopic gas of molecules, we have to propagate the driving pulse as well as the generated harmonics forward in time and space. The geometry is sketched in figure 7.1. A focused laser beam is directed towards a gas jet,

Propagation equations

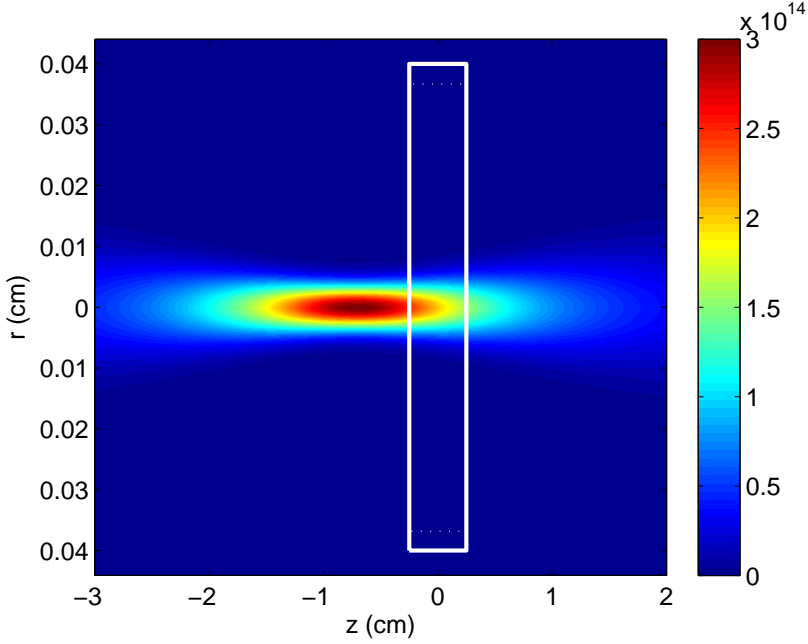


Figure 7.1 | Cut through a Gaussian beam with confocal parameter $b = 2$ cm that has been focused slightly in front of a gas jet, indicated by the white rectangle. The colour scale indicates the local intensity in units of W/cm^2 . The jet is completely homogeneous in the xy plane, but has absorbing boundaries at $r = \pm 0.37$ mm to limit the box size and avoid reflections from the box boundary.

indicated by the white box. The problem becomes rotationally symmetric if the gas is homogeneous in the plane perpendicular to the propagation direction z of the driving laser, and the beam is rotationally symmetric. In practical terms, we represent the gas as a grid in cylindrical coordinates with an absorbing boundary to avoid reflection at the edges. The boundary is placed far away from the core region where the harmonics are generated.

We now divide the target gas into slices that are sufficiently thin that the driving pulse does not change within the slice. Assuming that the generated harmonics do not propagate back-

wards, the full problem reduces to that of calculating the time-dependent polarization $\mathbf{P}(z, r, t)$ at each radius r , and propagating the total electric field $\mathbf{F}(z, r, t)$ into the adjacent slice according to Maxwell's wave equation (in SI units):

$$\nabla^2 \mathbf{F}(z, r, t) - \frac{1}{c^2} \frac{\partial^2}{\partial t^2} \mathbf{F}(z, r, t) = \frac{1}{\epsilon_0 c^2} \frac{\partial^2}{\partial t^2} \mathbf{P}(z, r, t). \quad (7.1)$$

We separate the electric field into a sum of the driving field and the generated high-harmonic field

$$\mathbf{F}(z, r, t) = \mathbf{F}_1(z, r, t) + \mathbf{F}_h(z, r, t), \quad (7.2)$$

apply the slowly evolving wave approximation, neglect absorption by the target gas, and neglect the back-action of the generated high-harmonics to obtain the following equations in the frequency domain:

$$\nabla_{\perp}^2 \tilde{\mathbf{F}}_1(z, r, \omega) + \frac{2i\omega}{c} \frac{\partial \tilde{\mathbf{F}}_1(z, r, \omega)}{\partial z} = -\frac{\omega^2}{\epsilon_0 c^2} \tilde{\mathbf{P}}_{\text{ion}}(z, r, \omega) \quad (7.3)$$

$$\nabla_{\perp}^2 \tilde{\mathbf{F}}_h(z, r, \omega) + \frac{2i\omega}{c} \frac{\partial \tilde{\mathbf{F}}_h(z, r, \omega)}{\partial z} = -\frac{\omega^2}{\epsilon_0 c^2} \tilde{\mathbf{P}}_{\text{dip}}(z, r, \omega). \quad (7.4)$$

In equation (7.3) the only influence of the gas on the driving field is through the free electrons generated by ionization of the target gas. This can be estimated using atomic or molecular ADK rates [32, 108]. Free electrons lead to defocusing of the focused laser beam, which influences the phase-matching conditions.

Of greater interest is the source term in equation (7.4) for the high-harmonic field, which is obtained from the Fourier transform of the single-molecule response multiplied by the (time-dependent) density:

$$\tilde{\mathbf{P}}(z, r, \omega) = \mathcal{F} \left[\rho(z, r, t) \left\langle \psi(t) \left| \hat{\mathbf{d}}_{\text{dip}} \right| \psi(t) \right\rangle \right]. \quad (7.5)$$

The time-dependence in $\rho(z, r, t)$ ensures that depletion of the ground state is taken into account. We use atomic or molecular ADK rates to estimate ionization. The expectation value

Phase-matching

$\langle \psi(t) | \hat{\mathbf{d}}_{\text{dip}} | \psi(t) \rangle$ has to be taken using a solution $|\psi(t)\rangle$ to the TDSE with the electric field $\mathbf{F}(z, r, t)$. Following the discussion in section 2.1 we choose to rewrite equation (7.5) in terms of the velocity spectrum:

$$\tilde{\mathbf{P}}(z, r, \omega) = \mathcal{F} \left[\rho(z, r, t) \frac{1}{i\omega} \langle \psi(t) | \hat{\mathbf{v}}_{\text{dip}} | \psi(t) \rangle \right]. \quad (7.6)$$

The conversion factor $\frac{1}{i\omega}$ is obtained by partial integration, assuming that the dipole moment is equal to zero at $t = \infty$. We solve equation (7.6) using the Stark-corrected Lewenstein model derived in section 5.1.

7.2 Phase-matching

We now have all the elements necessary to discuss phase-matching. The final macroscopic HHG signal is strongest if the harmonics generated in one slice add constructively with those generated in the adjacent slice. In other words, the wave vector \mathbf{k}_ω of the propagating field with angular frequency ω must be equal to the wave vector $\mathbf{k}_{\text{source}}$ of the newly generated field. Writing out the relevant contributions to $\mathbf{k}_{\text{source}}$ we get the phase-matching condition

$$\mathbf{k}_{\text{dip},j}(r, z) + \frac{\omega}{\omega_1} \mathbf{k}_{\text{focus}}(r, z) + \frac{\omega}{\omega_1} \mathbf{k}_1 = \mathbf{k}_\omega \quad (7.7)$$

$$\nabla \phi_{\text{dip},j}(r, z) + \frac{\omega}{\omega_1} \nabla \phi_{\text{focus}}(r, z) + \frac{\omega}{c} \mathbf{e}_z = \mathbf{k}_\omega, \quad (7.8)$$

where ω_1 is the central frequency of the laser light, \mathbf{k}_1 the central wave vector of the laser light, \mathbf{e}_z the unit vector along the propagation axis, $\phi_{\text{dip},j}(r, z)$ the intrinsic intensity-dependent phase of the generated radiation, and $\phi_{\text{focus}}(r, z)$ the geometrical phase variation caused by focusing of the laser beam. The index j in $\phi_{\text{dip},j}(r, z)$ distinguishes between short ($j = 1$) and long trajectories ($j = 2$). Optimal phase-matching is obtained when the phase

mismatch

$$\Delta \mathbf{k}_\omega(r, z) = \frac{\omega}{c} - \left| \mathbf{k}_{\text{dip},j}(r, z) + \frac{\omega}{\omega_1} (\mathbf{k}_{\text{focus}}(r, z) + \mathbf{k}_1) \right| \quad (7.9)$$

is minimized. We will now see how this is achieved on-axis in the forwards (+ z) direction.

For a given ω , each trajectory corresponds to a pair of ionization and recombination times (t, t'). Using the multi-centre stationary-phase method, the corresponding phase is

$$\begin{aligned} \phi_{\text{dip},j}(r, z) = & -S(\mathbf{k}_s, t, t') \\ & + [\mathbf{k} + \mathbf{A}(t)] \cdot \mathbf{R}_{n_f} - [\mathbf{k} + \mathbf{A}(t')] \cdot \mathbf{R}_{n_i} \end{aligned} \quad (7.10)$$

$$\begin{aligned} = & - \int_{t'}^t \left(\frac{1}{2} [\mathbf{k}_s + \mathbf{A}(r, z, t'')]^2 - E \right) dt'' \\ & + [\mathbf{k} + \mathbf{A}(t)] \cdot \mathbf{R}_{n_f} - [\mathbf{k} + \mathbf{A}(t')] \cdot \mathbf{R}_{n_i} \end{aligned} \quad (7.11)$$

for each combination of ionization site \mathbf{R}_{n_i} and recombination site \mathbf{R}_{n_f} . In the above equations

$$\mathbf{k}_s = -\frac{1}{t-t'} \int_{t'}^t \mathbf{A}(r, z, t'') dt'' + \frac{1}{t-t'} (\mathbf{R}_{n_f} - \mathbf{R}_{n_i}) \quad (7.12)$$

is the stationary momentum that dominates the harmonic signal at the frequency ω for a given ionization and recombination site within the molecule. However, the second term is completely independent of the position of the molecule within the gas, so it does not enter into $\mathbf{k}_{\text{dip},j}(r, z) = \nabla \phi_{\text{dip},j}(r, z)$.

The first term in equation (7.11) represents the kinetic energy gained in an oscillating laser field, and grows monotonically as a function of the ponderomotive potential $U_p = \frac{I}{4\omega_1^2}$. Ignoring the potential energies in equation (7.11), the intrinsic phase is therefore conveniently expressed as

$$\frac{d}{dz} \phi_{\text{dip},j}(r, z) \approx -\frac{dS(\mathbf{k}_s(t, t'), t, t')}{dI(r, z)} \frac{dI(r, z)}{dz}. \quad (7.13)$$

Phase-matching

The sign of the first factor is fixed, so the sign of $\frac{d}{dz}\phi_{\text{dip},j}(r, z)$ is determined by the second factor through the intensity variation of the focused laser beam.

For a Gaussian beam, $\phi_{\text{focus}}(r, z)$ is the so-called Gouy phase

$$\phi_{\text{focus}}(r, z) = -\text{atan}\left(\frac{2z}{b}\right) + \frac{2k_1 r^2 z}{b^2 + 4z^2}, \quad (7.14)$$

where b is the confocal parameter. The on-axis part gives the contribution

$$\left.\frac{d}{dz}\phi_{\text{focus}}(r, z)\right|_{r=0} = -\frac{2b}{b^2 + 4z^2}, \quad (7.15)$$

which has the same sign along the entire propagation axis. Inserting equations (7.13) and (7.15) into equation (7.9) we get the following expression for the on-axis phase mismatch:

$$\begin{aligned} \Delta k_\omega(r=0, z) \approx & \left.\frac{dS(\mathbf{k}_s(t, t'), t, t')}{dI(r, z)} \frac{dI(r, z)}{dz}\right|_{r=0} \\ & + \frac{\omega}{\omega_1} \frac{2b}{b^2 + 4z^2}. \end{aligned} \quad (7.16)$$

The Gouy contribution is always positive, while the ponderomotive phase is positive in front of the laser focus and negative after the laser focus. Equation (7.16) thus confirms the well-known result from atomic gasses that the laser focus must be placed in front of the target gas for optimal phase-matching.

The importance of ignoring the potential energies in equation (7.13) is difficult to determine, as the potential energy terms change sign depending on the ionization and recombination site. A further complication arises from the different ionization and recombination probabilities at different atomic centres. Macroscopic phase-matching of high harmonics in molecular gasses has previously been studied using the QRS model, and there are no indications that nonpolar molecules phase-match qualitatively differently than noble gas atoms [109–111]. On the contrary, under favorable conditions the effect of phase-matching may even be factored out of the HHG spectrum [111, 112].

7.3 Phase-matching for polar molecules

As discussed at length in chapter 5, polar molecules acquire an additional intensity dependent phase contribution due to the laser-induced Stark shift. We include this in the Lewenstein model by adiabatically adjusting the bound state energy, so equation (7.11) becomes

$$\begin{aligned} \phi_{\text{dip},j}(r, z) = & - \int_{t'}^t \left(\frac{1}{2} [\mathbf{k}_s(t, t') + \mathbf{A}(r, z, t'')]^2 \right. \\ & \left. - E(\mathbf{F}(r, z, t'')) \right) dt'' \\ & + [\mathbf{k} + \mathbf{A}(t)] \cdot \mathbf{R}_{n_f} - [\mathbf{k} + \mathbf{A}(t')] \cdot \mathbf{R}_{n_i}. \end{aligned} \quad (7.17)$$

At a first glance, equation (7.17) suggests that the optimal phase-matching condition is different for polar molecules. However, drawing on the results of section 5.3, we recognize that

$$\begin{aligned} \phi_{\text{dip},j}(r, z) = & - \int_{t'}^t \left(\frac{1}{2} [\mathbf{k}_s(t, t') + \mathbf{A}(r, z, t'')]^2 - E \right) \\ & - \Phi_{\text{Stark}}^{(1)}(t, t') - \Phi_{\text{Stark}}^{(2)}(t, t') \\ & + [\mathbf{k} + \mathbf{A}(t)] \cdot \mathbf{R}_{n_f} - [\mathbf{k} + \mathbf{A}(t')] \cdot \mathbf{R}_{n_i}, \end{aligned} \quad (7.18)$$

where

$$\Phi_{\text{Stark}}^{(1)}(t, t') = - \int_{t'}^t \boldsymbol{\mu} \cdot \mathbf{F}(r, z, t'') dt'' \quad (7.19)$$

$$\Phi_{\text{Stark}}^{(2)}(t, t') = - \frac{1}{2} \int_{t'}^t \mathbf{F}^T(r, z, t'') \underline{\underline{\boldsymbol{\alpha}}} \mathbf{F}(r, z, t'') dt''. \quad (7.20)$$

The main result of section 5.3 is equation (5.15)

$$\Phi_{\text{Stark}}^{(1)}(\omega) \approx \pm \mu \cos(\varphi) \sqrt{2(\omega - I_p)},$$

which shows that the first-order Stark phase is similar for short and long trajectories, and almost completely independent of intensity. This leaves the second-order Stark phase, which is fairly

Phase-matching for polar molecules

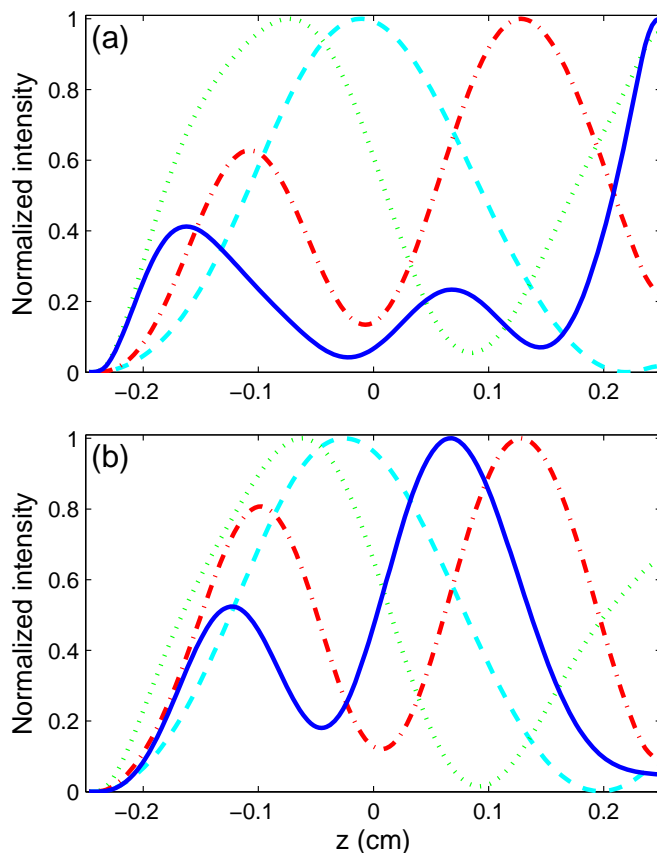


Figure 7.2 | On-axis build-up of four harmonics in a target gas of oriented CO (a) without including the Stark effect, and (b) including the Stark effect. The four harmonics are H15 (dashed cyan), H20 (dotted green), H25 (dash-dotted red), and H30 (full blue). Each harmonic is normalized to 1 to ease comparison.

flat and only on the order of 0.2π for usual field strengths (see figure 5.4). We are therefore led to expect that optimal phase-matching conditions for oriented polar molecules will be nearly identical to those of nonpolar targets.

The importance of phase-matching is illustrated by figure 7.2,

which shows the build-up of four harmonics. The gas is a 5 mm jet of CO molecules. The CO molecules are assumed to be perfectly oriented parallel to the polarization axis of the driving laser. The gas density is set to $5 \times 10^{14} \text{ cm}^{-3}$, which is low compared to most HHG experiments but high compared to the density that can be currently obtained for an oriented sample of CO molecules. The Gaussian laser beam is focused in the middle of the jet with a confocal parameter $b = 2.0 \text{ cm}$. The driving pulse has a central wave length of 800 nm, with a peak intensity of $2 \times 10^{14} \text{ W/cm}^2$. The electric field of the pulse has a cosine squared envelope containing six optical cycles T , corresponding to a FWHM of $2.18T$.

Following the intensity of the individual harmonics in figure 7.2(a), it is clear that the focusing conditions are far from optimal. Rather than building up steadily through the gas, each harmonic experiences a region of destructive interference due to phase-matching. Introducing the Stark effect in figure 7.2(b) gives qualitatively the same phase-matching. This is confirmed by figure 7.3, which shows the on-axis spectra at the end of the gas jet. The difference in amplitude is mainly caused by the influence that the Stark effect has on the initial ionization step, as discussed in section 5.2. This is clearer from the time-profile of the emitted harmonics in figure 7.4.

7.4 Robustness of Stark phases

The preceding section shows that Stark phases play a minor role in the macroscopic phase-matching of high-harmonics. We will now investigate whether the converse is also true; do the predictions of the single-molecule treatment in section 5.3 survive phase-matching?

As in section 5.3 we employ an ultra short pulse to restrict the HHG to one half-cycle, and compare spectra calculated with and without including the Stark effect. We use the same driving pulse as in figure 5.9, except for adding a Gaussian focus with confocal parameter $b = 2.0 \text{ cm}$. The focus is placed 0.7 cm in front of the

Robustness of Stark phases

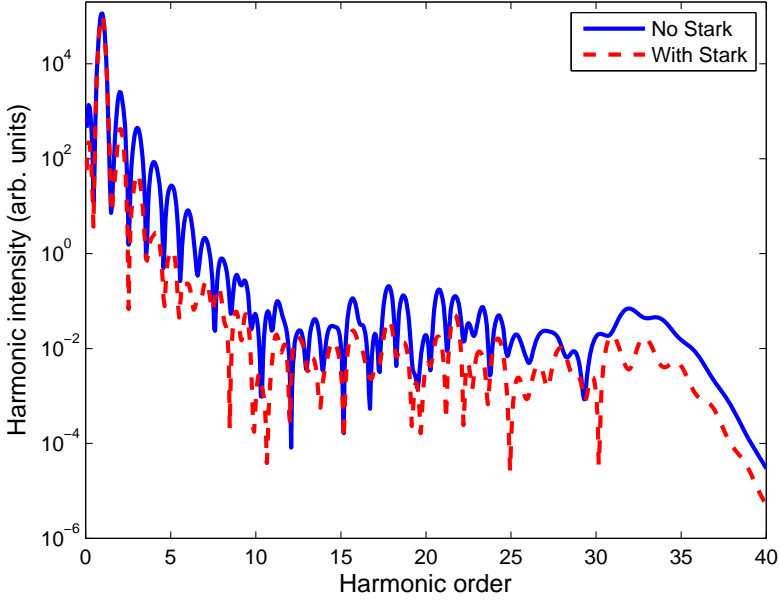


Figure 7.3 | On-axis HHG spectra from oriented CO with and without inclusion of the Stark effect. The driving pulse contains six optical cycles.

middle of the 5 mm gas jet in order to have good phase-matching of the short trajectories. The peak intensity is 3×10^{14} W/cm², chosen so as to give a peak intensity of 2×10^{14} W/cm² in the middle of the gas. Resulting on-axis spectra at the end of the gas jet are shown in figure 7.5. The interference minima are caused by interference between the short and long trajectories as in figure 5.7, except that they are broadened by the intensity variation of the driving pulse along the propagation direction.

It is not experimentally feasible to measure phases at the end of the target gas, nor only of the on-axis harmonics. We therefore transform the full harmonic field $\mathbf{F}_h(\omega, r)$ to the far field, apply a spatial filter that selects predominantly the central, short trajectory contribution to the harmonics, and transform back to the

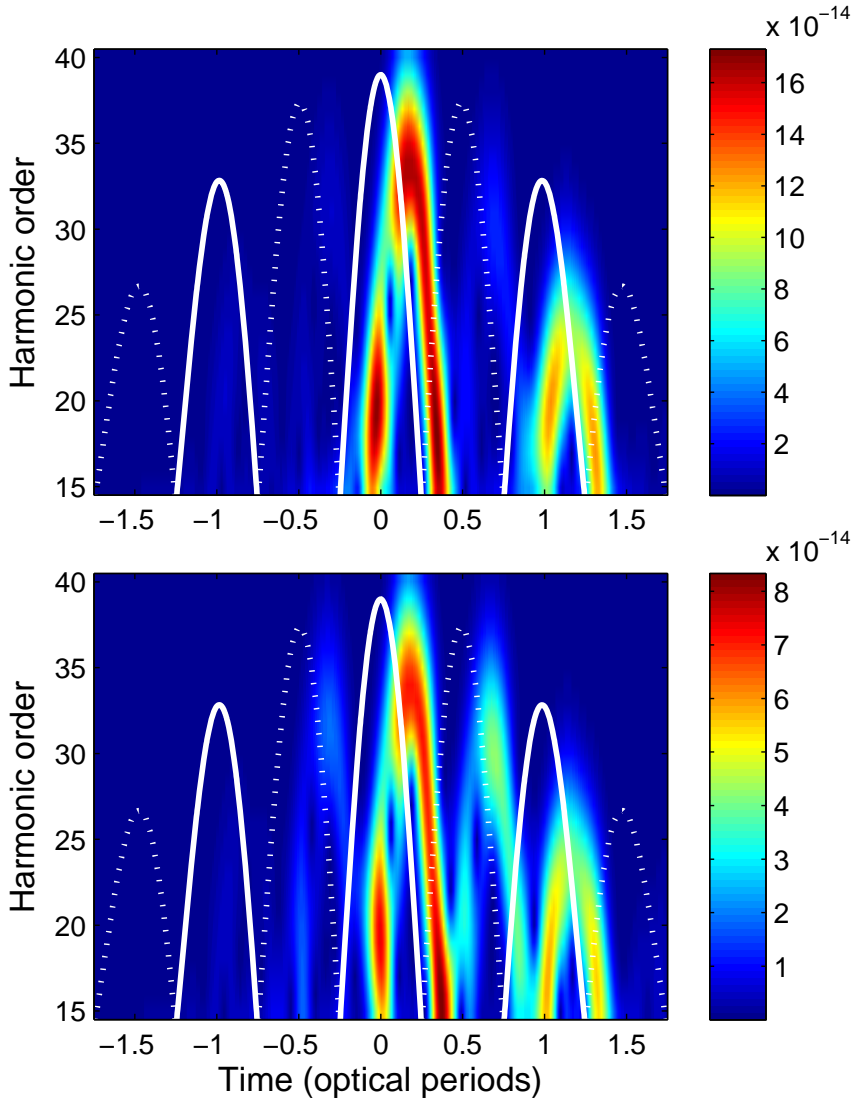


Figure 7.4 | On-axis time-profile analysis of the high-harmonics generated from oriented CO (a) without including the Stark effect, and (b) including the Stark effect. Note the different false-colour scale. The electric field is the on-axis field at the centre of the gas jet.

Robustness of Stark phases

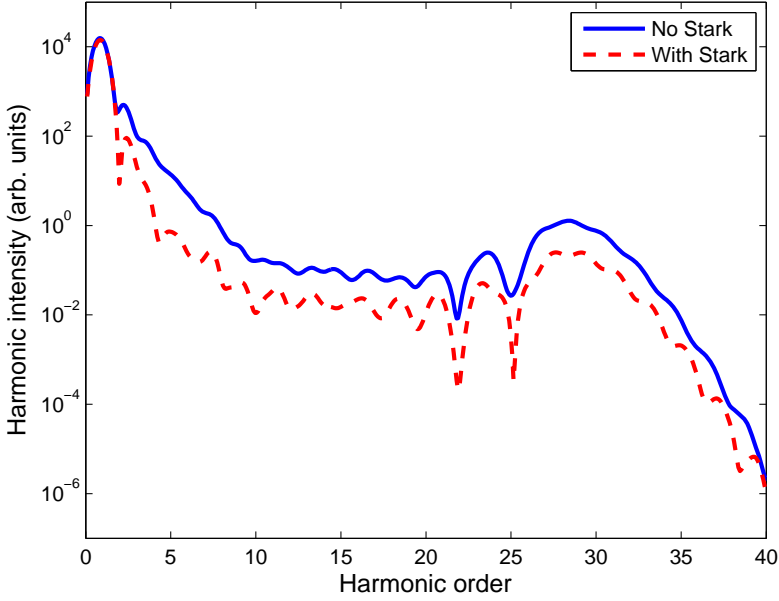


Figure 7.5 | On-axis HHG spectra from oriented CO with and without inclusion of the Stark effect. The driving pulse contains two optical cycles.

near field. In an experiment this would correspond to having an aperture or a refocusing mirror in the far field. Then we subtract the phases obtained with and without including Stark shifts. An average over the final spot on the detector screen is made by weighting the Stark phase $\Phi_{\text{Stark}}(\omega, r)$ at a given radius with the strength of the harmonic $|\mathbf{F}_h(\omega, r)|^2$:

$$\langle \Phi_{\text{Stark}}(\omega) \rangle_r = \frac{\int_0^\infty \Phi_{\text{Stark}}(\omega, r) |\mathbf{F}_h(\omega, r)|^2 r dr}{\int_0^\infty |\mathbf{F}_h(\omega, r)|^2 r dr}. \quad (7.21)$$

The result is shown in figure 7.6(a). The broad oscillations around the classical trajectory prediction can be attributed to the broadening of the intensity-dependent interference between short and long trajectories. The overall trend remains the same as for

the single-molecule result in figure 5.9(a), however. We therefore conclude that Stark phases really do survive phase-matching in the target gas, as we were led to expect from equation (5.15). Our results are almost unchanged if we extract the Stark phase from a coherent average of harmonic spectra over the final spot, rather than using the incoherent average of phases in equation (7.21).

As in the single-molecule case, we also present results for perfectly aligned CO molecules. Spectra are calculated with and without the Stark effect by solving the Maxwell wave equation separately for opposite orientations, and adding the resulting harmonics coherently at the end of the gas [34]. This procedure is valid in the limit where ionization-induced reshaping of the driving pulse is negligible, which is the case for the very low target densities we employ. The harmonics are then propagated to the far field, filtered, refocused, and the Stark phase extracted. Equation (7.21) is then used to calculate the radially averaged Stark phase shown in figure 7.6(b). Just as in the single-molecule calculation of figure 5.9(b), the first-order Stark phase survives due to geometric gating. We therefore repeat our conclusion from section 5.3: A measurement of the harmonic phase of aligned CO driven by an ultra short pulse will provide an unambiguous test of our Stark-corrected Lewenstein model.

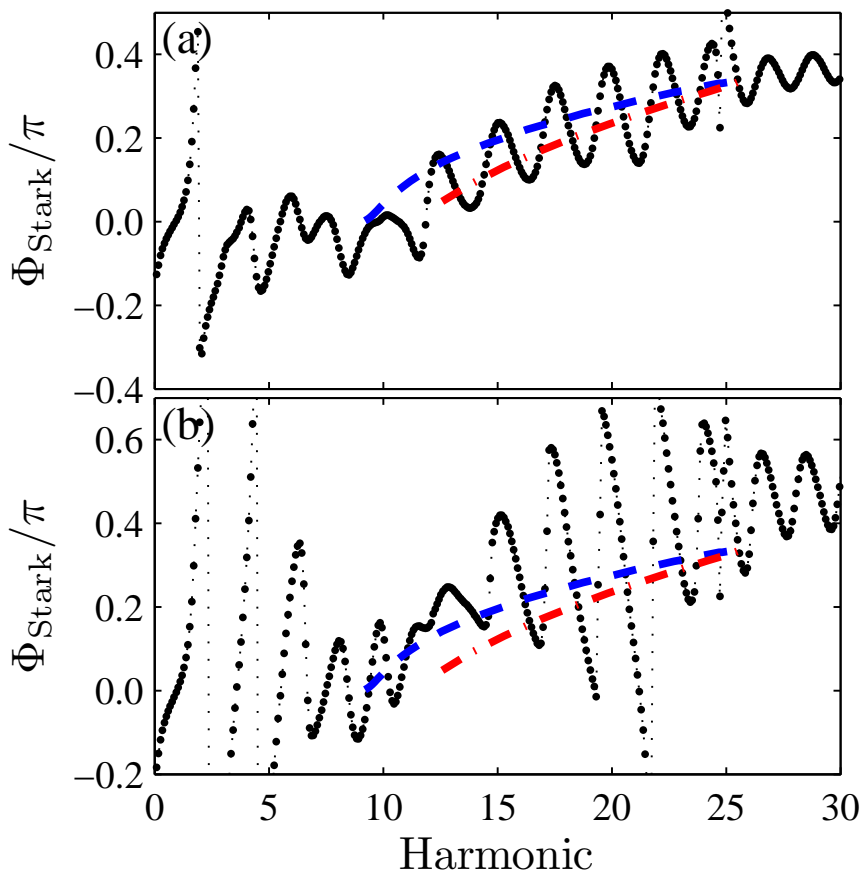


Figure 7.6 | Stark phases from a gas jet of CO molecules subject to the same ultra short driving pulse used for figure 5.9. (a) The CO molecules are oriented. The connected black dots are phases obtained from a full simulation including macroscopic propagation. The dashed blue curve is the single-molecule phase predicted from short classical trajectories, and the dash-dotted red curve the phase from long trajectories. (b) The CO molecules are *aligned* parallel to the laser polarization. The black dots include both orientations of the target molecules. Dashed and dash-dotted curves indicate short and long classical trajectories.

Summary and outlook

Strong-field physics is an exciting and rewarding field due to its combination of technological potential, experimental challenges, hard computational problems, and intuitively appealing models. The strong-field approximation is the gold standard that experiment and theory is compared against. This is sort of surprising, given the extreme approximations it entails. The first major approximation is that the ground state is completely unperturbed even though the laser field is strong enough to significantly populate the electron continuum. The second approximation says that the continuum electron is completely unaffected by the Coulomb potential of the residual ion. However, a new class of experiments is forcing us to refine both approximations greatly.

Taking HHG as an example, harmonic spectra have recently been used to reconstruct the highest occupied molecular orbitals of N_2 and CO_2 [89–91]. The long-term goal is to track electron dynamics in arbitrary molecules by reconstructing the electron wave function with Ångström spatial resolution and attosecond timing. To do so requires very detailed models that account for all deviations from the pure strong-field approximation.

8.1 Summary

The work presented in this thesis was mainly concerned with the influence that the strong driving laser has on the bound state. This was inspired by the photoelectron angular distribution recorded for oriented OCS, which disagrees completely with model calculations unless the laser-induced time-dependent Stark shift is included [41]. Seeing as ionization is the first step in HHG, a similar extension is expected to be necessary to describe HHG from polar molecules. We extended the Lewenstein model of HHG to polar molecules by adiabatically Stark shifting each occupied molecular orbital according to the instantaneous value of the driving laser. Using CO as an example, this was shown to impact HHG in several ways.

The first effect was directly related to the ionization step. Polar molecules have asymmetric ionization rates due to the asymmetric charge distribution of the highest occupied molecular orbital. In CO, this results in a much higher ionization rate when the electric field points from C to O, thus determining the relative strength between harmonic bursts in neighbouring half-cycles. The first-order Stark shift counteracted this gating mechanism by raising the ionization potential in the preferred half-cycle. While not large enough to reverse the trend completely, the Stark shift did reduce the asymmetry between neighbouring harmonic bursts considerably.

High-order harmonic generation is an intrinsically coherent process; a fact that is sometimes downplayed by the intuitive three-step model. If the continuum and bound-state wave packets did not evolve coherently, then the radiation emitted by each molecule in the target gas would not add up to a macroscopic high-harmonic signal. An alternative picture of HHG is that the returning continuum wave packet interferes with the bound-state wave packet, which sets up interference fringes. This serves as a molecular sized antenna, which emits high-frequency radiation. In the latter picture, it is clear that a modification of the bound state phase will result in a changed interference between the con-

tinuum and bound-state wave packets. We quantified this rather vague statement in terms of the Stark phase.

The Stark phase is the phase that the bound-state wave packet accumulates due to the Stark shift. It can be accessed theoretically by calculating high-harmonic spectra with and without including the Stark shift, and then subtracting the harmonic phases. The result was shown to agree with classical calculations based on continuum electron trajectories calculated within the three-step model.

Surprisingly, the first-order Stark phase turned out to be nearly the same for short and long trajectories. In fact, the first-order Stark phase was shown to be proportional to the return velocity of the continuum electron. The return velocity relates directly to the energy of the emitted photon, showing that the first-order Stark phase is independent of the detailed pulse parameters. An accurate analytical expression was derived, expressing the first-order Stark phase in terms of the square root of the harmonic frequency.

The smaller second-order Stark phase did not behave as nicely. It is different for short and long trajectories, and depends explicitly on the driving pulse. It was shown, however, that the second-order Stark phase can be minimized by keeping the harmonic cutoff fixed and increasing the wave length of the driving laser. This allows the total Stark phase to be predicted analytically under the right experimental conditions.

While most theoretical works on HHG are concerned with the single-molecule response, the actual harmonic field is the result of a coherent build-up of harmonics in a target gas. Theoretically, the single-molecule response serves as a source term in Maxwell's wave equation. The appearance of a sizable Stark phase in the single-molecule signal suggests that phase-matching might be quite different for polar molecules. We showed that this is not the case. This could be ascribed to the insensitivity of the dominating first-order Stark phase to the local driving field. This also caused the first-order Stark phase to survive phase-matching.

Experimentally, it is very difficult to obtain a gas of oriented

Summary

molecules with sufficient density to directly observe the above mentioned effects. Fortunately, the intrinsic gating in the ionization step ensures that an aligned gas will behave similar to an oriented one if subjected to an ultra short driving pulse. We showed in both single-molecule and macroscopic calculations that aligned CO should exhibit a significant first-order Stark phase. This allows our model to be verified (*or* falsified) by recording the harmonic phase of aligned CO and subtracting all other known phase contributions.

High-order harmonic generation from polar molecules has other unique features than just the Stark effect. One such feature is a modification of the famous two-centre interference minimum. The most prominent spectral feature in HHG, two-centre interference has received huge interest due to its connection to the internuclear distance. Two-centre interference is thus the prototypical example of structure retrieval using HHG.

We extended the two-centre interference model to both oriented and aligned polar molecules. In the oriented case, the interference minimum was shown to depend on both the phase *and* amplitude of the recombination matrix elements at each nucleus, as well as the usual dependence on the position of the nuclei. The corresponding interference condition was also derived for aligned polar molecules. The resulting minimum could be interpreted either as an interference between recombination at different atomic species or between opposite orientations. Our calculations showed that the interference minimum of CO not only survived alignment, but that it was actually more pronounced than in the oriented case. Surprisingly, the first-order Stark phase turned out to shift the interference minimum of aligned CO by as much as three harmonic orders, which could also be understood from our two-centre interference condition.

8.2 Outlook

Research in strong-field physics will most likely continue to revolve around the development of HHG as a light source. The major limitation for the technological application of HHG is its low conversion efficiency, which prevents attosecond pump-probe experiments from being realised. The most promising avenues being followed at the moment are HHG in high-pressure gasses [3–5], and seeding of free-electron lasers [10, 11]. While free-electron lasers have the potential of reaching much higher intensities than can ever be attained in a pure HHG setup, the need for an undulating cloud of mutually repelling electrons limits their use to experiments that do not require attosecond precision. The high-pressure gas method suffers from the fact that most schemes for generating sub-femtosecond pulses in HHG rely on detailed control of the pulse form of the driving laser. Translating these schemes into a regime where the laser undergoes self-focusing due to extensive ionization of a dense target gas is not trivial, and will require detailed modelling of both the single-atom and macroscopic response.

In the meantime, measurements of photoelectrons and high-order harmonics continue to be the only means with which to probe the dynamics of valence electrons on their natural time scale. This line of enquiry is limited by the need for extremely precise theories with which to interpret experimental data. The positive side effect is that strong-field experiments provide results that are detailed enough to challenge existing theories. This will hopefully accelerate the development of new theoretical and numerical strategies to cope with continuum dynamics of interacting many-body systems.

Due to the permanent dipoles of their orbitals, polar molecules are ideal systems with which to test the validity of new models that aim at improving the description of the laser-induced bound-state dynamics. Our results provide a reference point that allows true dynamical effects to be separated from the much simpler Stark shift, or the purely static effect of nonsymmetric or-

Outlook

bitals. The simplest extension is to use adiabatic ground states for each value of the electric field. This can be implemented in the Lewenstein model using quantum chemistry codes to find the adiabatic ground states. A problem with such an approach is that quantum chemistry codes typically do not produce very reliable results for large electric fields. This approach also only includes adiabatic deformations, but completely neglects nonadiabatic couplings between orbitals.

A promising numerical method is the separation of space into two separate volumes: An inner volume where the full many-body problem is solved under influence of both the Coulomb and laser interaction, and an outer volume where the dynamics of a single electron is dominated by the laser field [113]. Only electrons that make it back to the parent ion contribute to high-order harmonic generation, making absorbing boundaries or complex scaling methods well-suited for reducing the size of the outer volume. A recent advance is the development of the so-called infinite-range exterior complex scaling, which uses long-range basis states to describe the asymptotic region rather than throwing away all information beyond a sharp boundary. This drastically reduces the necessary size of the outer volume [114, 115].

As the target systems get bigger and bigger, the numerical methods are bound to become too time-consuming. In order to study, for example, energy transfer in the light harvesting complex [116], we need simplified models. So far the quantitative rescattering model has been very successful in describing new details of high-order harmonic generation [64, 65]. However, it relies on the factorization of high-order harmonic generation into a continuum wave packet and a more or less independent rescattering event. This means that effects that stem from a coherence between ionization and recombination are excluded. An example of such a coherence is the exchange trajectories that cause elliptically polarized harmonics to be emitted by N_2 in the Lewenstein model, even when driven by a linearly polarized driving laser [74]. The contribution from this coherence is smaller than the experimentally determined ellipticity, but there is no reason to expect

that a similar effect will not play a role in extended systems. The numeric method of partitioning space into an inner and an outer volume may provide a clue how to improve the factorization scheme.

Study of (almost) field-free molecular structure is restricted to moderate intensities on the order of $\sim 10^{14}$ W/cm². As the intensity is increased further, the bound state becomes more and more deformed, depending on its polarizability [44]. At the very highest intensities, the so-called Cramers-Henneberger states may turn out to be a more natural basis set for the description of strong-field phenomena [117, 118]. One challenge that needs to be addressed is how to reach sufficiently high laser intensities without ionizing the target during the ramp-up of the pulse envelope. Another challenge is to switch between the moderate-laser regime and the intense-laser regime in a consistent way.



Inducing elliptically polarized high-order harmonics from aligned molecules with linearly polarized femtosecond pulses

Adam Etches, Christian Bruun Madsen, and Lars Bojer Madsen

Physical Review A **81**, 013409 (2010).

Inducing elliptically polarized high-order harmonics from aligned molecules with linearly polarized femtosecond pulses

Adam Etches, Christian Bruun Madsen, and Lars Bojer Madsen

Lundbeck Foundation Theoretical Center for Quantum System Research, Department of Physics and Astronomy, Aarhus University, DK-8000 Aarhus C, Denmark

(Received 8 October 2009; published 22 January 2010)

A recent paper reported elliptically polarized high-order harmonics from aligned N_2 using a linearly polarized driving field [X. Zhou *et al.*, Phys. Rev. Lett. **102**, 073902 (2009)]. This observation cannot be explained in the standard treatment of the Lewenstein model and has been ascribed to many-electron effects or the influence of the Coulomb force on the continuum electron. We show that nonvanishing ellipticity naturally appears within the Lewenstein model when using a multicenter stationary-phase method for treating the dynamics of the continuum electron. The reason for this is the appearance of additional contributions, which can be interpreted as quantum orbits in which the active electron is ionized at one atomic center within the molecule and recombines at another. The associated exchange harmonics are responsible for the nonvanishing ellipticity and result from a correlation between the ionization site and the recombination site in high-order harmonic generation.

DOI: 10.1103/PhysRevA.81.013409

PACS number(s): 33.80.Rv, 42.65.Ky, 42.65.Re

I. INTRODUCTION

High-order harmonic generation (HHG) is a highly nonlinear process in which a medium in an intense laser field emits coherent radiation at multiples of the driving frequency. The short time scale of the generation process makes HHG a promising source of coherent attosecond pulses in the XUV regime. When the target is isotropic, such as a gas of atoms or unaligned molecules, it follows from symmetry arguments that the emitted harmonics have to be polarized parallel to the polarization axis of a linearly polarized driving laser. Breaking this isotropy by using a sample of aligned molecules for HHG allows for a nonvanishing perpendicular polarization component. This scenario is sketched in Fig. 1. The perpendicular component is generally heavily suppressed compared to the parallel component. This has led to a focus in the literature on the parallel component. Recent experiments on aligned N_2 , O_2 , and CO_2 , however, have reported a nonvanishing perpendicular component [1]. Moreover, elliptically polarized harmonics have been measured from aligned N_2 and CO_2 [2]. The presence of elliptically polarized harmonics opens up the possibility of generating elliptically polarized attosecond pulses in the XUV regime.

From a theoretical point of view, the observation of elliptically polarized harmonics is very interesting because it serves as an important benchmark for different models. Several approaches are currently used to calculate the HHG response. Ideally, one should propagate the time-dependent Schrödinger equation (TDSE) [3,4]. This approach has been used for atoms and small molecules. An example is the prediction of comparable polarization components from aligned H_2^+ near minima in the spectrum [5]. For systems beyond H_2^+ and H_2 , one commonly uses the semiclassical simple-man's model [6] or the quantum mechanical Lewenstein model [7] to describe HHG. Both models provide a three-step picture of the process in which a single active electron is brought into the continuum due to its interaction with the laser field, propagates in the field, and subsequently recombines and emits radiation.

The calculation of HHG spectra using the Lewenstein model is generally combined with a stationary-phase method to reduce the computational cost. As discussed in Sec. II B, this procedure causes the resulting harmonics to be linearly polarized parallel to the polarization of the driving laser. This shortcoming has been attributed to the Lewenstein model itself [1,2]. However, the standard stationary-phase method is not in general valid for molecular targets, as it fails to take into account the spatial extent of the molecule [8]. Instead, an extended stationary-phase method can be applied to evaluate the Lewenstein model, which leads to so-called exchange harmonics [8]. These are contributions to the total harmonic emission that are caused by quantum orbits describing an ionization event at one atomic center followed by recombination at another atomic center (see Fig. 2).

We show that the Lewenstein model does lead to elliptically polarized high-order harmonics when exchange harmonics are included. Exchange harmonics rely on a correlation between the ionization and recombination events in HHG. This is different from the perpendicular harmonic component reported in [9], which is obtained using scattering states for the continuum dynamics, thus causing a spread in momentum of the returning electron. The derivation in [9,10] uses the standard stationary-phase method to separate the three steps of the HHG process. Consequently, any correlation, in the sense of exchange harmonics, between ionization and recombination sites is lost. Detailed comparison with experiments such as that in [2] will serve to determine the importance of this correlation.

The present paper is organized as follows. We briefly describe the Lewenstein model for aligned molecules in Sec. II A. The stationary-phase method is introduced in Sec. II B, and the resulting harmonics shown to be linearly polarized parallel to the linear polarization of the driving laser. In Sec. II C we present the extended stationary-phase method, and Sec. III contains results demonstrating that such a treatment of the Lewenstein model leads to elliptically polarized harmonics from aligned N_2 . We summarize our

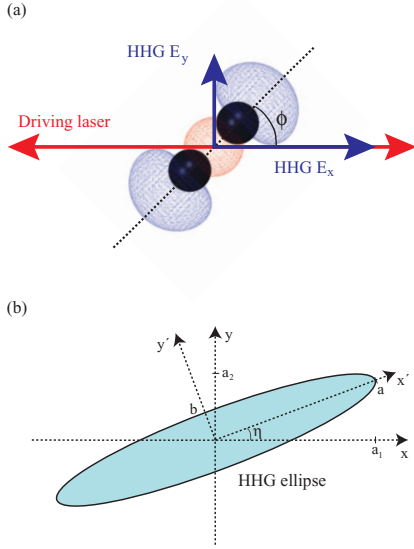


FIG. 1. (Color online) (a) The driving pulse propagates along the z axis and is linearly polarized along the x axis. The molecule is aligned at an angle of ϕ to the x axis in the xy plane. The alignment at a given angle with respect to the external field results in harmonic emission with components E_x and E_y . The hatched structure indicates the HOMO (see Sec. III). (b) The polarization ellipse for a single harmonic. The angle η of the major axis and the length b of the minor axis have been exaggerated for clarity.

findings in Sec. IV. Atomic units ($\hbar = e = m_e = a_0 = 1$) are used throughout unless stated otherwise.

II. THEORY

We treat the response of a single molecule to the electric field $\mathbf{F}(t)$ of an intense femtosecond laser pulse. The laboratory frame is chosen such that the pulse propagates along the z axis and is linearly polarized along the x axis. We define the pulse by the vector potential

$$\mathbf{A}(t) = \frac{F_0}{\omega_0} f(t) \cos(\omega_0 t) \mathbf{e}_x, \quad (1)$$

where F_0 is the maximal field strength, ω_0 the angular frequency, $f(t)$ the pulse envelope starting at $t = 0$ and ending at $t = T$ (see Sec. III), and \mathbf{e}_x the polarization direction. The electric field is obtained from Eq. (1) as $\mathbf{F}(t) = -\partial_t \mathbf{A}(t)$.

A. The Lewenstein model for aligned molecules

The calculated spectrum $S_n(\omega)$ of the harmonic component along \mathbf{n} depends on the choice of gauge and form. Following [11], we use the length gauge for the interaction Hamiltonian, and the velocity form to determine the dipole acceleration. Thus, given the dipole velocity $\mathbf{v}_{\text{dip}}(t)$, the signal is

$$S_n(\omega) = \left| \mathbf{n} \cdot \int_0^T dt e^{i\omega t} \frac{d}{dt} \langle \mathbf{v}_{\text{dip}}(t) \rangle \right|^2. \quad (2)$$

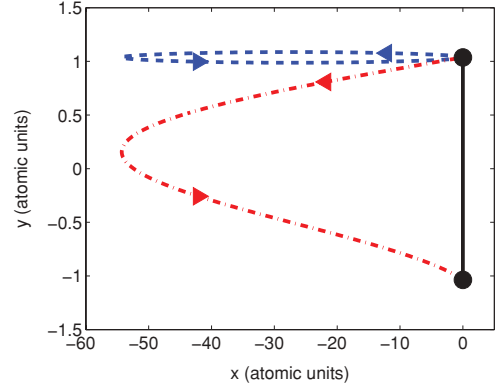


FIG. 2. (Color online) Two orbits with ionization at the peak of the field and recombination two thirds of an optical cycle later. The atomic centers of the molecule are sketched as black dots to the right. The laser polarization is taken to be in the x direction. The dashed (blue) line represents an orbit that gives rise to direct harmonics, i.e., ionization and recombination at the same center. A transverse component has been added manually to distinguish the return path. The dash-dotted (red) line is an orbit that gives rise to exchange harmonics, i.e., ionization at one center and recombination at another center. Note that the units on the two axes differ.

When evaluating Eq. (2), it is necessary to include contributions from all occupied molecular orbitals λ [12], so

$$\langle \mathbf{v}_{\text{dip}}(t) \rangle = \sum_{\lambda} P_{\lambda} \langle \mathbf{v}_{\lambda}(t) \rangle, \quad (3)$$

with weights P_{λ} fulfilling the normalization condition $\sum_{\lambda} P_{\lambda} = 1$. Introducing Euler angles $\mathcal{R} = (\phi, \theta, \chi)$ for the molecular orientation in the laboratory frame, the alignment distribution $G(\mathcal{R})$ for a given molecule and alignment pulse can be calculated as in [13]. Following [12,14], this results in a coherent average over fixed alignment angles

$$\langle \mathbf{v}_{\lambda}(t) \rangle = \int d\mathcal{R} G(\mathcal{R}) \langle \mathbf{v}_{\lambda}(\mathcal{R}, t) \rangle. \quad (4)$$

The dipole velocity of a single perfectly aligned molecular orbital is calculated using the Lewenstein formula

$$\begin{aligned} \langle \mathbf{v}_{\lambda}(\mathcal{R}, t) \rangle &= i \int_0^t d\tau \int d\mathbf{k} \mathbf{v}_{\text{rec},\lambda}^*(\mathcal{R}, \mathbf{k}, t) \\ &\quad \times e^{-iS_{\lambda}(\mathbf{k}, t, t-\tau)} \mathbf{F}(t-\tau) \cdot \mathbf{d}_{\text{ion},\lambda}(\mathcal{R}, \mathbf{k}, t-\tau) \\ &\quad + \text{c.c.}, \end{aligned} \quad (5)$$

where the nuclei are taken to be fixed during the driving pulse. This latter approximation is valid for heavy atoms such as nitrogen [15,16].

Equation (5) depends on the Fourier transform of the electronic wave function $\tilde{\psi}_{\lambda}$ in both the ionization term

$$\mathbf{d}_{\text{ion},\lambda}(\mathbf{k}, t-\tau) = i \nabla_{\mathbf{k}+\mathbf{A}(t-\tau)} \tilde{\psi}_{\lambda}[\mathcal{R}, \mathbf{k} + \mathbf{A}(t-\tau)], \quad (6)$$

and the recombination term

$$\mathbf{v}_{\text{rec},\lambda}(\mathbf{k}, t) = [\mathbf{k} + \mathbf{A}(t)] \tilde{\psi}_{\lambda}[\mathcal{R}, \mathbf{k} + \mathbf{A}(t)]. \quad (7)$$

The vertical ionization potential $|E_\lambda|$ enters into the phase factor $S_\lambda(\mathbf{k}, t, t - \tau)$ as

$$S_\lambda(\mathbf{k}, t, t - \tau) = \int_{t-\tau}^t \frac{1}{2} [\mathbf{k} + \mathbf{A}(t'')]^2 dt'' - E_\lambda \tau. \quad (8)$$

B. Standard stationary-phase method

The momentum integral in Eq. (5) describes the propagation of the active electron in the continuum. This integral is usually calculated using the stationary-phase method, approximating it by a normalization factor times the value of the integrand at the stationary point \mathbf{k}_s of the rapidly varying phase.

Identifying the total phase with $S_\lambda(\mathbf{k}, t, t - \tau)$ gives the stationary-phase condition

$$\nabla_{\mathbf{k}} S_\lambda(\mathbf{k}, t, t - \tau)|_{\mathbf{k}=\mathbf{k}_s} = 0, \quad (9)$$

which leads directly to the stationary momentum

$$\mathbf{k}_s = -\frac{1}{\tau} \int_{t-\tau}^t \mathbf{A}(t'') dt''. \quad (10)$$

The standard stationary-phase method thus yields

$$\begin{aligned} \langle \mathbf{v}_\lambda(\mathcal{R}, t) \rangle &\approx i \int_0^t d\tau \left(\frac{2\pi}{\epsilon + i\tau} \right)^{3/2} \mathbf{v}_{\text{rec},\lambda}^*(\mathcal{R}, \mathbf{k}_s, t) \\ &\times e^{-iS_\lambda(\mathbf{k}_s, t, t-\tau)} \mathbf{F}(t-\tau) \cdot \mathbf{d}_{\text{ion},\lambda}(\mathcal{R}, \mathbf{k}_s, t-\tau) \\ &+ \text{c.c.} \end{aligned} \quad (11)$$

Calculated spectra depend only weakly on the chosen value of ϵ , which is set to 1 in the following.

Equations (10) and (11) select the dominant contribution to the full momentum integral in Eq. (5). It is conventional to interpret the result of such a stationary-phase analysis in terms of quantum orbits [17,18]. In this language, the active electron tunnels out, propagates parallel to the polarization of the laser, and recombines.

The vector character of Eq. (11) is determined by $\mathbf{v}_{\text{rec},\lambda}(\mathcal{R}, \mathbf{k}_s, t)$. Referring to Eqs. (7) and (10), it is clear that the emitted harmonics are polarized parallel to the linear polarization of the driving laser. The Lewenstein model with the standard stationary-phase method cannot give rise to ellipticities different from zero.

C. Extended stationary-phase method

The treatment in Sec. II B is oversimplified in the molecular case [8]. The reason for this is that $\mathbf{d}_{\text{ion},\lambda}$ and $\mathbf{v}_{\text{rec},\lambda}$ pick up phase factors related to the internuclear separation. This is readily seen when the electronic wave function is expanded around the atomic centers as

$$\psi_\lambda(\mathbf{r}) = \sum_n \phi_n(\mathbf{r} - \mathbf{R}_n). \quad (12)$$

The Fourier transforms in Eqs. (6) and (7) then separate into terms each relating to just one atomic center. This implies that

$$\mathbf{d}_{\text{ion},\lambda}(\mathbf{k}, t - \tau) = \sum_{n_i} \mathbf{d}_{\text{ion},\lambda}^{n_i}(\mathbf{k}, t - \tau), \quad (13)$$

and

$$\mathbf{v}_{\text{rec},\lambda}(\mathbf{k}, t) = \sum_{n_f} \mathbf{v}_{\text{rec},\lambda}^{n_f}(\mathbf{k}, t). \quad (14)$$

Each term in Eqs. (13) and (14) acquires an associated phase factor $e^{i[\mathbf{k}+\mathbf{A}(t-\tau)]\cdot\mathbf{R}_{n_i}}$ or $e^{i[\mathbf{k}+\mathbf{A}(t)]\cdot\mathbf{R}_{n_f}}$, which has to be taken into account when performing the stationary-phase analysis. Here n_i refers to the atomic center involved in evaluating $\mathbf{d}_{\text{ion},\lambda}^{n_i}$, and n_f refers to $\mathbf{v}_{\text{rec},\lambda}^{n_f}$.

The above discussion means that Eq. (5) can be split into

$$\langle \mathbf{v}_\lambda(\mathcal{R}, t) \rangle = \sum_{n_i, n_f} \langle \mathbf{v}_\lambda^{n_i n_f}(\mathcal{R}, t) \rangle. \quad (15)$$

The stationary-phase condition for $\langle \mathbf{v}_\lambda^{n_i n_f}(\mathcal{R}, t) \rangle$ is

$$\int_{t-\tau}^t [\mathbf{k} + \mathbf{A}(t'')] dt'' - (\mathbf{R}_{n_f} - \mathbf{R}_{n_i})|_{\mathbf{k}=\mathbf{k}_s} = 0, \quad (16)$$

with associated stationary momenta

$$\mathbf{k}_s^{n_i n_f} = -\frac{1}{\tau} \int_{t-\tau}^t \mathbf{A}(t'') dt'' + \frac{1}{\tau} (\mathbf{R}_{n_f} - \mathbf{R}_{n_i}). \quad (17)$$

Applying this multicenter stationary-phase method to the integral in Eq. (5) finally yields

$$\begin{aligned} \langle \mathbf{v}_\lambda(\mathcal{R}, t) \rangle &\approx i \sum_{n_i, n_f} \int_0^t d\tau \left(\frac{2\pi}{\epsilon + i\tau} \right)^{3/2} \mathbf{v}_{\text{rec},\lambda}^{n_f*}(\mathcal{R}, \mathbf{k}_s^{n_i n_f}, t) \\ &\times e^{-iS_\lambda(\mathbf{k}_s^{n_i n_f}, t, t-\tau)} \\ &\times \mathbf{F}(t-\tau) \cdot \mathbf{d}_{\text{ion},\lambda}^{n_i}(\mathcal{R}, \mathbf{k}_s^{n_i n_f}, t-\tau) \\ &+ \text{c.c.} \end{aligned} \quad (18)$$

The terms in Eq. (18) can be interpreted as semiclassical orbits of electrons that are ionized at \mathbf{R}_{n_i} and recombine at \mathbf{R}_{n_f} . The effect of using the multicenter stationary-phase method is to properly include orbits from one atom to another. The resulting harmonics are referred to as exchange harmonics [8]. A similar idea was explored in an earlier paper [19], and its above-threshold ionization analog is well known in the literature [20–22].

The vector character of the emitted harmonics is determined by $\mathbf{v}_{\text{rec},\lambda}^{n_f}$ in Eq. (18). In analogy to the standard stationary-phase method, $\mathbf{v}_{\text{rec},\lambda}^{n_i n_f}$ is parallel to $\mathbf{A}(t) + \mathbf{k}_s^{n_i n_f}$. As seen from Eq. (17), this means that exchange harmonics will contribute with a nonvanishing perpendicular component if the molecular axis has a nonvanishing projection orthogonal to the driving laser. The conventional stationary-phase method only includes the direct harmonics, which is why the standard treatment of the Lewenstein model fails to reproduce, even qualitatively, the findings of [1,2].

An example of the two types of orbits is presented in Fig. 2. The electron is ionized at one atomic center at the peak of the field and recombines two thirds of an optical cycle later. Laser parameters are the same as those used in Sec. III below. The orbit that gives rise to direct harmonics has been plotted with a small artificial transverse displacement in order to separate the two parts of the electron motion. Similar orbits exist which describe ionization at the other atomic center.

We note in passing that the full Lewenstein expression in Eq. (5) is independent of whether a single-center or a multicenter expansion is adopted. The distinction is purely an artifact of using a stationary-phase method to approximate the momentum integral. In this setting, a multicenter expansion is

preferable, as it easily allows the geometric phase factors to be extracted.

III. RESULTS AND DISCUSSION

We present here a proof-of-principle calculation on N_2 in order to illustrate that Eq. (18) indeed leads to elliptically polarized harmonics when using a linearly polarized driving pulse. We assume only contributions from the $3\sigma_g$ orbital, which is the highest occupied molecular orbital (HOMO). The HOMO is obtained using the standard quantum chemistry software package GAMESS-US [23] with a triple zeta valence basis set and with additional diffuse s and p orbitals. We assume perfect alignment and perform no focal volume averaging. The alignment geometry and the polarization ellipse are shown in Fig. 1. Based on a wavelet analysis [24], the τ integral in Eq. (18) is restricted to allow only short trajectories. This means that the upper bound is set to 0.67 times an optical cycle. The driving field is taken to be an 800 nm pulse with 11 cycles in a trapezoidal envelope with three optical cycles for the linear ramp-up and ramp-down. The peak intensity is 6×10^{14} W/cm².

We follow the polarization conventions in [25]. This means that the harmonic of angular frequency ω is assumed to be a perfect plane wave

$$\mathbf{F}^H(t) = a_1 \cos(\omega t + \delta_1) \mathbf{e}_x + a_2 \cos(\omega t + \delta_2) \mathbf{e}_y, \quad (19)$$

$$= a \cos(\omega t + \delta_0) \mathbf{e}_x \pm b \sin(\omega t + \delta_0) \mathbf{e}_y, \quad (20)$$

where $\mathbf{e}_x, \mathbf{e}_y, a_1, a_2, \mathbf{e}_x', \mathbf{e}_y', a, b$ are defined in Fig. 1(b). Phases δ_i ($i = 0, 1, 2$) are found by assuming that the harmonic phase is equal to that of the dipole velocity [5,26].

The two physically relevant quantities are the ellipticity ϵ and the angle η that the polarization ellipse major axis makes to the polarization axis of the driving pulse. These are determined by

$$\epsilon = \pm \frac{b}{a}, \quad -\frac{\pi}{4} \leq \tan^{-1}(\epsilon) \leq \frac{\pi}{4}, \quad (21)$$

and

$$\tan(2\eta) = \frac{2a_1/a_2}{1 - (a_1/a_2)^2} \cos(\delta_2 - \delta_1). \quad (22)$$

A. Equilibrium nuclear spacing

In this subsection, we will restrict ourselves to the equilibrium nuclear spacing of $R_0 = 1.0977$ Å. Figures 3(a) and 3(b) and 4(a) and 4(b) show data for harmonics 17 and 27, with solid (blue) curves referring to the component parallel with the linear polarization of the driving field and dashed (red) curves to the perpendicular component. Panels (a) illustrate how the parallel polarization component of the harmonic emission changes its phase much faster than the perpendicular component. Comparison with panels (b) shows that the rapid change in phase is accompanied by a drop in harmonic intensity, causing an increase in the ratio of perpendicular to parallel harmonic intensity.

We determine the ellipticity ϵ and the angle η of the major axis using Eqs. (21) and (22). Results are shown in panels (c) and (d). Both are seen to be very angle dependent, taking nonvanishing values where the parallel component has

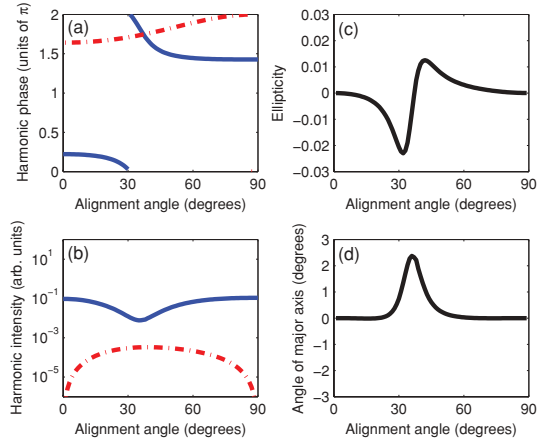


FIG. 3. (Color online) Orientation dependence of harmonic 17 from the $3\sigma_g$ HOMO of N_2 with equilibrium internuclear distance $R_0 = 1.0977$ Å. We use an 800 nm, 6×10^{14} W/cm² driving field. The envelope (for the vector potential) is trapezoidal with three optical cycles turn-on and turn-off and five cycles constant amplitude. (a) Harmonic phase, (b) harmonic intensity, (c) ellipticity, and (d) angle of polarization ellipse major axis with respect to molecular axis. In (a) and (b), the solid (blue) curves refer to the parallel polarization component and the dash-dotted (red) curves to the perpendicular component.

a rapid change in phase. This variation in phase changes the helicity of the harmonics over a very short angle interval, while the angle of the major axis has a definite sign for a given harmonic.

Figure 5 shows the absolute value of the ellipticity as a function of harmonic order for selected alignment angles. The angular dependence can largely be understood by comparing panel (b) in Fig. 3 with that in Fig. 4. The dip in the intensity of the parallel component is fairly narrow and moves to larger

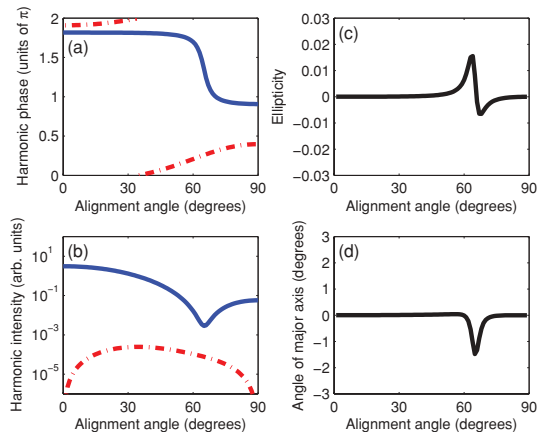


FIG. 4. (Color online) Same as Fig. 3, but for harmonic 27.

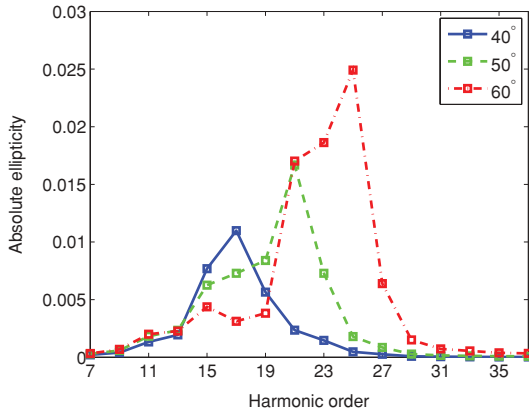


FIG. 5. (Color online) Absolute value of the harmonic ellipticity ϵ as a function of harmonic order for selected alignment angles ϕ of N_2 . The nuclei are fixed at their equilibrium position. The solid (blue) curve refers to $\phi = 40^\circ$, the dashed (green) curve to $\phi = 50^\circ$, and the dash-dotted (red) curve to $\phi = 60^\circ$. See the caption of Fig. 3 for laser parameters.

angles for increasing harmonic order in agreement with the two-slit interference formula [27]. The resulting ellipticity does not compare well with [2]. The experimental ellipticities are an order of magnitude higher and hardly have any angle dependence.

The presented calculation shows that elliptically polarized high-order harmonics are predicted within the Lewenstein model. Improvements have to be made in order to compare the model directly with experimental data. One of these is to include the lower-lying molecular orbitals (HOMO-1, HOMO-2, etc.). The inclusion of these is expected to cause a dynamical minimum in the parallel component [9], which would change the detailed structure. Taking into account the

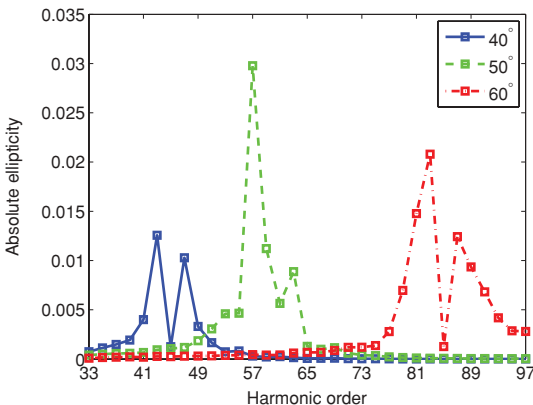


FIG. 6. (Color online) Same as Fig. 5, but with the nuclei fixed at $R = 2R_0$.

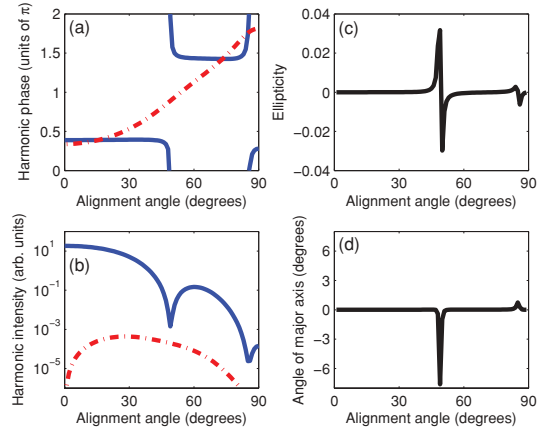


FIG. 7. (Color online) Same as Fig. 3, but for harmonic 57 and with $R = 2R_0$.

distribution over alignment angles $G(\mathcal{R})$ might also prove to be important [see Eq. (4)].

B. Extended nuclear spacing

As discussed above, exchange orbits give rise to elliptically polarized harmonics when the parallel polarization component is suppressed by the two-slit interference condition [27]. Changing the internuclear separation will have an effect on this interference. Figure 6 shows results for N_2 with $R = 2R_0$. The plotted ellipticity is seen to peak at higher harmonic orders than was the case at $R = R_0$. There is no significant change in the magnitude of the obtained ellipticities. Figure 7 shows the detailed behavior of the 55th harmonic. A second interference minimum appears at large alignment angles, which is consistent with the second-order minimum in the two-slit model.

IV. CONCLUSION

Motivated by recent experiments [1,2], we have addressed the issue of understanding how elliptically polarized harmonics arise in HHG when using a linearly polarized driving laser. It was shown that the Lewenstein model does not allow the emission of harmonics with a nonvanishing perpendicular component if the standard stationary-phase method is used to evaluate the continuum dynamics. A multicenter stationary-phase method was adopted in order to take into account the spatial extent of the molecule. This leads to additional terms in the Lewenstein model compared to the standard stationary-phase method. These were interpreted as quantum orbits describing an ionization event at one atomic center followed by propagation in the continuum and recombination at a different atomic center [8]. We illustrated that the total harmonic emission from N_2 calculated using this method is elliptically polarized near minima in the spectrum.

The electron continuum was described using only Volkov waves, as opposed to the use of scattering states [9],

indicating that the appearance of elliptically polarized harmonics is in part the result of having an extended target. Further work is required to ascertain the importance of the Coulomb interaction between the active electron and the molecular ion.

ACKNOWLEDGMENTS

We thank Brett D. Esry for fruitful discussions. This work was supported by the Danish Research Agency (Grant No. 2117-05-0081).

-
- [1] J. Levesque, Y. Mairesse, N. Dudovich, H. Pépin, J.-C. Kieffer, P. B. Corkum, and D. M. Villeneuve, *Phys. Rev. Lett.* **99**, 243001 (2007).
- [2] X. Zhou, R. Lock, N. Wagner, W. Li, H. C. Kapteyn, and M. M. Murnane, *Phys. Rev. Lett.* **102**, 073902 (2009).
- [3] M. B. Gaarde, J. L. Tate, and K. J. Schafer, *J. Phys. B* **41**, 132001 (2008).
- [4] E. Lorin, S. Chelkowski, and A. D. Bandrauk, *New J. Phys.* **10**, 025033 (2008).
- [5] M. Lein, N. Hay, R. Velotta, J. P. Marangos, and P. L. Knight, *Phys. Rev. Lett.* **88**, 183903 (2002).
- [6] P. B. Corkum, *Phys. Rev. Lett.* **71**, 1994 (1993).
- [7] M. Lewenstein, P. Balcou, M. Y. Ivanov, A. L'Huillier, and P. B. Corkum, *Phys. Rev. A* **49**, 2117 (1994).
- [8] C. C. Chirilă and M. Lein, *Phys. Rev. A* **73**, 023410 (2006).
- [9] O. Smirnova, S. Patchkovskii, Y. Mairesse, N. Dudovich, D. Villeneuve, P. Corkum, and M. Y. Ivanov, *Phys. Rev. Lett.* **102**, 063601 (2009).
- [10] M. Y. Ivanov, T. Brabec, and N. Burnett, *Phys. Rev. A* **54**, 742 (1996).
- [11] C. C. Chirilă and M. Lein, *J. Mod. Opt.* **54**, 1039 (2007).
- [12] C. B. Madsen and L. B. Madsen, *Phys. Rev. A* **76**, 043419 (2007).
- [13] J. Ortigoso, M. Rodríguez, M. Gupta, and B. Friedrich, *J. Chem. Phys.* **110**, 3870 (1999).
- [14] C. B. Madsen, A. S. Mouritzen, T. K. Kjeldsen, and L. B. Madsen, *Phys. Rev. A* **76**, 035401 (2007).
- [15] C. B. Madsen and L. B. Madsen, *Phys. Rev. A* **74**, 023403 (2006).
- [16] S. Patchkovskii, *Phys. Rev. Lett.* **102**, 253602 (2009).
- [17] P. Salieres *et al.*, *Science* **292**, 902 (2001).
- [18] C. Figueira de Morisson Faria, *Phys. Rev. A* **76**, 043407 (2007).
- [19] R. Kopold, W. Becker, and M. Kleber, *Phys. Rev. A* **58**, 4022 (1998).
- [20] M. Okunishi, R. Itaya, K. Shimada, G. Prümper, K. Ueda, M. Busuladžić, A. Gazibegović-Busuladžić, D. B. Milošević, and W. Becker, *Phys. Rev. Lett.* **103**, 043001 (2009).
- [21] M. Busuladžić, A. Gazibegović-Busuladžić, D. B. Milošević, and W. Becker, *Phys. Rev. A* **78**, 033412 (2008).
- [22] M. Busuladžić, A. Gazibegović-Busuladžić, D. B. Milošević, and W. Becker, *Phys. Rev. Lett.* **100**, 203003 (2008).
- [23] M. Schmidt *et al.*, *J. Comput. Chem.* **14**, 1347 (1993).
- [24] P. Antoine, B. Piraux, and A. Maquet, *Phys. Rev. A* **51**, R1750 (1995).
- [25] M. Born and E. Wolf, *Principles of Optics: Electromagnetic Theory of Propagation, Interference and Diffraction of Light* (Pergamon, New York, 1970), 4th ed.
- [26] C. C. Chirilă and M. Lein, *Phys. Rev. A* **80**, 013405 (2009).
- [27] M. Lein, N. Hay, R. Velotta, J. P. Marangos, and P. L. Knight, *Phys. Rev. A* **66**, 023805 (2002).



Extending the strong-field approximation of high-order harmonic generation to polar molecules: gating mechanisms and extension of the harmonic cutoff

Adam Etches, and Lars Bojer Madsen

Journal of Physics B **43**, 155602 (2010)

Extending the strong-field approximation of high-order harmonic generation to polar molecules: gating mechanisms and extension of the harmonic cutoff

Adam Etches and Lars Bojer Madsen

Lundbeck Foundation Theoretical Center for Quantum System Research, Department of Physics and Astronomy, Aarhus University, 8000 Aarhus C, Denmark

E-mail: bojer@phys.au.dk

Received 26 April 2010, in final form 24 June 2010

Published 20 July 2010

Online at stacks.iop.org/JPhysB/43/155602

Abstract

Polar molecules such as CO are interesting target systems for high-order harmonic generation (HHG) as they can be oriented with current laser techniques, thus allowing the study of systems without inversion symmetry. However, the asymmetry of the molecule also means that the molecular orbitals are Stark shifted in energy due to their interaction with the driving laser. We extend the strong-field approximation of HHG by incorporating the Stark shift into the Lewenstein model and discuss its impact on two different gating mechanisms in CO. In *system-induced gating* an oriented target molecule serves as a gate by selecting every other half-cycle due to an increased (decreased) ionization rate. In *field-induced gating* the waveform of the driving laser is tailored such that the harmonic emission from an aligned molecule is damped (enhanced) every other half-cycle. We show that the Stark shift weakens the strength of system-induced gating and also determines the relative contribution from opposite orientations in field-induced gating. Finally, we propose a novel scheme for extending the high-order harmonic cutoff by letting the two gating mechanisms counteract each other, thus allowing for a higher laser intensity without increased ionization of the target gas.

(Some figures in this article are in colour only in the electronic version)

1. Introduction

High-order harmonic generation (HHG) is a highly nonlinear process that takes place when an intense femtosecond laser pulse is focused onto a gas. The least bound electrons experience a force comparable to that of the Coulomb interaction with the nuclei, leading to the emission of a broad range of harmonics. HHG is often described as three separate steps. First an electron tunnels out into the continuum due to the laser interaction. The electron is then driven away from the parent ion by the laser field and back again when the field changes its sign. Finally, the electron recombines and emits its excess kinetic energy as radiation.

Studies of HHG are largely driven by the desire to obtain a table-top source of coherent attosecond pulses reaching into the water window (284–543 eV) and above. The main problem

so far has been to generate sufficiently intense attosecond pulses for practical applications. The most efficient methods depend on a single-atom signal, which is then phase matched in the target medium [1, 2]. Replacing the atomic target with a target of aligned molecules adds a degree of control, and thus offers the possibility of extending the natural obtainable harmonic cutoff.

Most models of molecular HHG are based on the simple man's model [3] or the Lewenstein model [4]. The Lewenstein model is often referred to as the strong-field approximation of HHG. Both models rely on the assumption that the initial state of the active electron is unperturbed by the electric field of the laser pulse. This assumption yields surprisingly accurate results for non-polar molecules but breaks down for polar molecules due to the dipole interaction between the molecule and the electric field.

We argue that the Lewenstein model can be extended to polar molecules by including the Stark shift on each molecular orbital. In a single-active electron model the total HHG signal is the coherent sum over the contribution from every occupied molecular orbital [5]. These orbitals will experience an energy shift in response to an electric field. As polar molecules generally have asymmetric molecular orbitals, this results in a first-order Stark shift as well as higher order shifts, which can be incorporated into the Lewenstein model by modifying the ionization potential of each orbital according to the instantaneous value of the electric field. While not describing the deformation of the target molecule, this method does allow us to study some of the features that are unique for HHG from polar molecules within a well-established framework.

As an example of the importance of including the Stark shift, we study the concept of gating in HHG. Normally, only odd harmonics are emitted due to selection rules relating to the inversion symmetry of the target and the driving laser [6, 7]. There are two ways of breaking this symmetry. One is to use an initial target, which is not symmetric along the polarization axis of the laser [8–13]. The other is to modify the waveform of the driving laser [14–20].

Breaking the inversion symmetry of the target molecule is made possible, e.g. by recent advances in field-free molecular orientation [21–24]. As opposed to aligned molecules, that only have a well-defined internuclear axis, oriented molecules also have a well-defined head-to-tail direction. In general, such a molecule will have a preferred direction of ionization [24, 25], which means that the harmonic contribution will be larger from one half-cycle than the adjacent. We shall refer to this gating mechanism as *system-induced gating* as it is the molecule itself that serves as a gate. We show that it is important to include the Stark shift in HHG from polar molecules as it tends to decrease the strength of system-induced gating.

We also consider *field-induced gating* in which the waveform is changed so as to dampen the harmonic emission from an aligned target in every other half-cycle. An easy way to implement field-induced gating is to add a small amount of the second harmonic of the driving laser to the driving pulse [15, 17, 20]. As illustrated in figure 1, the second harmonic will dampen (enhance) every other half-cycle, thus damping (enhancing) the harmonic emission. We show that the Stark shift plays an important role in determining the relative HHG contribution from opposite orientations of the aligned molecule.

Finally, we also present a novel scheme for extending the harmonic cutoff by combining system-induced and field-induced gating. We use field-induced gating to counteract the system-induced gating of an oriented molecule, thus lowering the ionization rate. This allows us to increase the intensity of the driving field without ionizing the target, which in turn leads to an extension of the harmonic cutoff. An appealing feature of our method is that it can be combined with any other cutoff-extension scheme that relies on modified waveforms.

This paper is organized as follows. Our extension of the Lewenstein model is presented in section 2, supplemented by

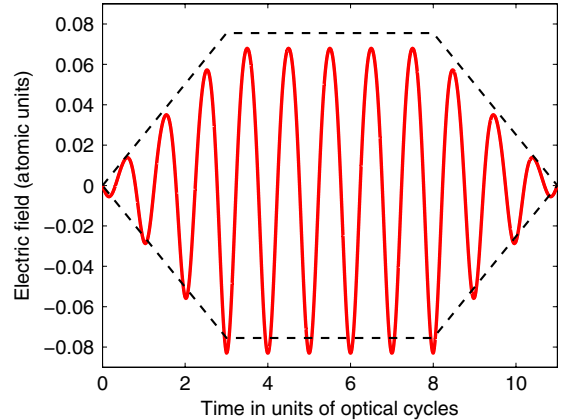


Figure 1. The result of adding 1% of the second harmonic in terms of intensity to an 11-cycle laser pulse with a trapezoidal envelope (indicated by the dashed line). The carrier envelope phase delay is set to zero in order to dampen (enhance) every other half-cycle. Note that the integral of the total field is zero as required of a physical pulse [26].

a discussion of the underlying physics behind system-induced and field-induced gating. Section 3 contains numerical results on CO, and section 4 sums up our conclusions. Atomic units ($\hbar = e = m_e = a_0 = 1$) are used throughout unless stated otherwise.

2. Theory

2.1. Lewenstein model without the Stark shift

The Lewenstein model for HHG has several variants [4, 27–35]. Our point of departure is the treatment in [35], where the extended stationary-phase method is used to approximate the momentum integral (describing continuum dynamics). Briefly, the HHG spectrum $S_n(\omega)$ of the harmonic component along \mathbf{n} is taken to be

$$S_n(\omega) = \left| \mathbf{n} \cdot \int e^{i\omega t} \frac{d}{dt} \langle \mathbf{v}_{\text{dip}}(t) \rangle dt \right|^2, \quad (1)$$

where $\mathbf{v}_{\text{dip}}(t)$ is the dipole velocity. The dipole velocity is split into a contribution from each molecular orbital λ [5]:

$$\langle \mathbf{v}_{\text{dip}}(t) \rangle = \sum_{\lambda} P_{\lambda} \langle \mathbf{v}_{\lambda}(t) \rangle. \quad (2)$$

Introducing the Euler angles $\mathcal{R} = (\phi, \theta, \chi)$ for the molecular orientation in the laboratory frame, the orientational distribution $G(\mathcal{R})$ of the molecule is factored out as a coherent sum [5, 12]

$$\langle \mathbf{v}_{\lambda}(t) \rangle = \int G(\mathcal{R}) \langle \mathbf{v}_{\lambda}(\mathcal{R}, t) \rangle d\mathcal{R}. \quad (3)$$

Finally, the Lewenstein model states that given an electric field $\mathbf{F}(t) = -\partial_t \mathbf{A}(t)$,

$$\langle \mathbf{v}_{\lambda}(\mathcal{R}, t) \rangle = i \int_0^t d\tau \int d\mathbf{k} \mathbf{v}_{\text{rec},\lambda}^*(\mathcal{R}, \mathbf{k}, t) e^{-iS_{\lambda}(\mathbf{k}, t, t-\tau)} \times \mathbf{F}(t-\tau) \cdot \mathbf{d}_{\text{ion},\lambda}(\mathcal{R}, \mathbf{k}, t-\tau) + \text{c.c.}, \quad (4)$$

where nuclear vibration is ignored, which is justified for heavy nuclei such as carbon and oxygen. We refer to [36–42] for a treatment that goes beyond the frozen core approximation. The momentum integral in (4) is evaluated using the extended stationary-phase method [29, 31, 35] in order to speed up calculations. Short trajectories are selected by restricting the τ -integral from zero to τ_{\max} of two thirds of an optical cycle, which is the classical return time.

Equation (4) depends on the Fourier transform of the electronic wavefunction $\tilde{\psi}_\lambda$ through the ionization term

$$\mathbf{d}_{\text{ion},\lambda}(\mathbf{k}, t - \tau) = i \nabla_{\mathbf{k}+\mathbf{A}(t-\tau)} \tilde{\psi}_\lambda[\mathcal{R}, \mathbf{k} + \mathbf{A}(t - \tau)] \quad (5)$$

and the recombination term

$$\mathbf{v}_{\text{rec},\lambda}(\mathbf{k}, t) = [\mathbf{k} + \mathbf{A}(t)] \tilde{\psi}_\lambda[\mathcal{R}, \mathbf{k} + \mathbf{A}(t)]. \quad (6)$$

Propagation in the continuum is contained in the semi-classical phase factor

$$S_\lambda(\mathbf{k}, t, t - \tau) = \int_{t-\tau}^t \left(\frac{1}{2} [\mathbf{k} + \mathbf{A}(t'')]^2 - E_\lambda \right) dt'', \quad (7)$$

where $|E_\lambda|$ is the vertical ionization potential of the molecular orbital in question.

2.2. Lewenstein model with the Stark shift

The Lewenstein model (4) is derived by approximating the full time-dependent molecular orbital with

$$|\psi_\lambda(t)\rangle = e^{-iE_\lambda(t-t_0)} |\psi_\lambda(t_0)\rangle - i \int_{t_0}^t d\mathbf{k} \int_{t_0}^t dt' |\psi_{\mathbf{k}}(t)\rangle \times e^{-iE_\lambda(t'-t_0)} \langle \psi_{\mathbf{k}}(t') | \mathbf{F}(t') \cdot \mathbf{r} | \psi_\lambda(t_0)\rangle. \quad (8)$$

Here $|\psi_\lambda(t_0)\rangle$ is the molecular orbital before the influence of the laser pulse, and $|\psi_{\mathbf{k}}(t)\rangle$ is the eigenstate of a free electron in a laser field with momentum \mathbf{k} , a so-called Volkov state. Equation (4) is obtained by calculating the expectation value of the dipole velocity and keeping only cross terms.

The phase factors in (8) containing E_λ are the result of applying the field-free time-evolution operator on a field-free energy eigenstate

$$\exp\left(-i \int_{t_0}^t \hat{H}_0 dt'\right) |\psi_\lambda(t_0)\rangle = \exp(-iE_\lambda(t-t_0)) |\psi_\lambda(t_0)\rangle, \quad (9)$$

assuming that the effect of the laser field on the initial state can be completely ignored up until the ionization step. However, a field-free eigenstate will experience a Stark shift in response to an electric field \mathbf{F} . Expanding in powers of the field, the shifted energy reads

$$E_\lambda = E_\lambda^{(0)} - \mu_\lambda^i F_i - \frac{1}{2} \alpha_\lambda^{ij} F_i F_j - \frac{1}{3!} \beta_\lambda^{ijk} F_i F_j F_k - \dots, \quad (10)$$

where μ_λ is the dipole, α_λ the polarizability and β_λ is the first hyperpolarizability of the molecular orbital expressed in the laboratory frame. We use Einstein summation for the tensor products. The relevant molecular orbital is typically the highest occupied molecular orbital (HOMO) due to its lower ionization potential.

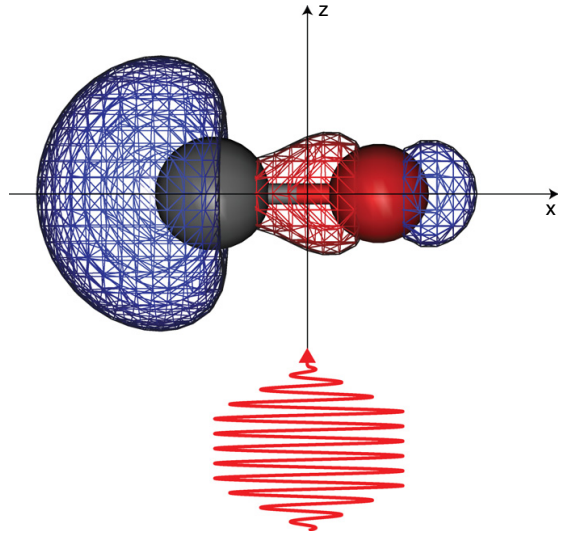


Figure 2. A sketch of the geometry. The molecule is oriented along the x axis, which is also the polarization axis of the linearly polarized driving pulse. Shown is the HOMO of CO obtained using standard quantum chemistry software [43]. There is a larger electron density near the carbon nucleus to the left, leading to a dipole of 1.1287 au pointing from the carbon to the oxygen nucleus. Note that the total dipole of the CO molecule is $0.112\text{D} = 0.0441$ au pointing from the oxygen to the carbon nucleus.

We propose to extend the Lewenstein model by Stark shifting the molecular orbitals according to the instantaneous value of the electric field

$$E_\lambda(t) = E_\lambda^{(0)} - \mu_\lambda^i F_i(t) - \frac{1}{2} \alpha_\lambda^{ij} F_i(t) F_j(t) - \dots \quad (11)$$

In this quasi-static approximation, it then follows that

$$\exp(-iE_\lambda(t-t_0)) |\psi_\lambda(t_0)\rangle \rightarrow \exp\left(-i \int_{t_0}^t E_\lambda(t') dt'\right) |\psi_\lambda(t_0)\rangle, \quad (12)$$

which reduces to first-order perturbation theory if the field is only included to first order in (11). The appealing feature of our approach is that it leaves the Lewenstein model in section 2.1 unchanged except for E_λ in (7) being replaced by $E_\lambda(t)$ in (11). The effect is thus to introduce a time-dependent ionization potential. The dipole and polarizabilities are found by calculating the energy of each molecular orbital for a range of static field strengths using standard quantum chemistry software [43], and fitting the result to a polynomial.

Our model is expected to be valid in the regime where the higher order Stark shifts are small. In HHG experiments typical field intensities are of the order of $1-2 \times 10^{14}$ W cm $^{-2}$, corresponding to a maximal field-strength of $F_0 \approx \sqrt{2} \times 10^{14} / 3.51 \times 10^{16}$ au = 0.075 au. Taking CO as an example, our quantum chemistry calculations [43] show that the HOMO, sketched in figure 2, has a permanent dipole of 1.1287 au leading to a Stark shift of 17% of the ionization potential. The maximal Stark shift is shown in figure 3 for the two possible orientations. The second-order Stark shift is much smaller than the first-order shift indicating that the field

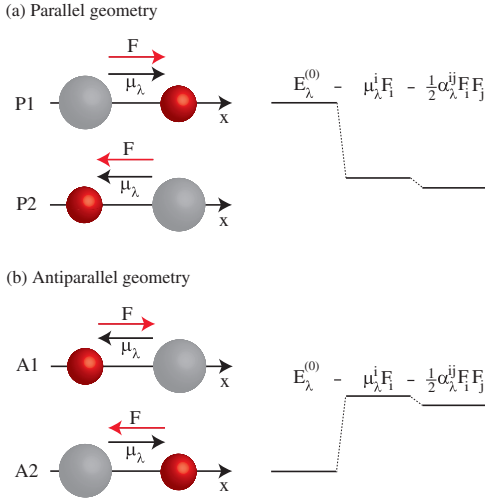


Figure 3. The two possible orientations of CO with the associated Stark shifts drawn to scale using the maximal field strength and the molecular parameters from section 3. The nuclei are drawn with an unequal size (C being the larger) to reflect the charge distribution of the HOMO in figure 2. (a) The HOMO dipole μ_λ is parallel to the electric field F , so the energy of the HOMO E_λ is shifted down. (b) The antiparallel geometry, in which the HOMO is shifted up in energy. The second-order induced-dipole shift caused by the polarizability α_λ is independent of the orientation and is much smaller than the first-order shift.

does not induce a large deformation of the molecular orbital or, equivalently, that there is not a large degree of state mixing of the bound states.

Simple considerations show why it has not previously been necessary to include the Stark shift in HHG modelling. The term that is linear in the field will always be exactly zero for non-polar molecules as their molecular orbitals do not possess a permanent dipole. The second-order term is symmetric with respect to the sign of the field and thus does not distinguish between half-cycles, and higher order terms are heavily suppressed due to the typical size of F_0 in HHG studies. The net effect is a slight lowering of the energy at the peak of the cycle due to the second-order Stark shift, leading to a negligible suppression of the total HHG signal. Including the first-order Stark shift is important for polar target molecules, however. We will highlight the role that the Stark shift plays in the context of gating mechanisms.

2.3. System-induced gating

The first gating mechanism to be discussed is system-induced gating, where the symmetry between half-cycles in HHG is broken due to a preferred direction of ionization in the oriented target molecule [24, 25]. One possible cause of asymmetry is the asymmetric charge distribution of the molecular orbital, which follows directly from the Lewenstein model. To simplify the argument we only consider the parallel geometry in figure 2, neglect the effect of the Stark shift and restrict ourselves to a driving field that is a sine with a constant

amplitude. This means that all the following vector equations can be restricted to just the x component along the polarization axis.

Applying the conventional stationary-phase approximation to the momentum integral in (4) leads to a stationary saddle-point momentum \mathbf{k}_s of [35]

$$\mathbf{k}_s(t, \tau) = -\frac{1}{\tau} \int_{t-\tau}^t \mathbf{A}(t') dt'. \quad (13)$$

Changing half-cycle is the same as changing the sign of \mathbf{A} , and thus of \mathbf{k}_s , because of the sinusoidal driving pulse. The overall effect of changing half-cycle can now be deduced from (4)–(7). Using general properties of the Fourier transform,

$$\tilde{\psi}_\lambda[\mathcal{R}, -\mathbf{k}] = \tilde{\psi}_\lambda^*[\mathcal{R}, \mathbf{k}], \quad (14)$$

and

$$\nabla_{-\mathbf{k}} \tilde{\psi}_\lambda[\mathcal{R}, -\mathbf{k}] = -\nabla_{\mathbf{k}} \tilde{\psi}_\lambda^*[\mathcal{R}, \mathbf{k}]. \quad (15)$$

Changing half-cycle thus results in

$$\mathbf{v}_{\text{rec},\lambda}^*(\mathcal{R}, \mathbf{k}, t) \rightarrow -\mathbf{v}_{\text{rec},\lambda}(\mathcal{R}, \mathbf{k}, t), \quad (16)$$

and

$$\begin{aligned} & \mathbf{F}(t - \tau) \cdot \mathbf{d}_{\text{ion},\lambda}(\mathcal{R}, \mathbf{k}, t - \tau) \\ & \rightarrow -\mathbf{F}(t - \tau) \cdot \mathbf{d}_{\text{ion},\lambda}^*(\mathcal{R}, \mathbf{k}, t - \tau). \end{aligned} \quad (17)$$

The semi-classical phase in (7) does not change, so the integrand in (4) is changed from

$$i\mathbf{v}_{\text{rec},\lambda}^*(\mathcal{R}, \mathbf{k}, t) e^{-iS_\lambda(\mathbf{k}, t, t-\tau)} \mathbf{F}(t - \tau) \cdot \mathbf{d}_{\text{ion},\lambda}(\mathcal{R}, \mathbf{k}, t - \tau) \quad (18)$$

to

$$i\mathbf{v}_{\text{rec},\lambda}(\mathcal{R}, \mathbf{k}, t) e^{-iS_\lambda(\mathbf{k}, t, t-\tau)} \mathbf{F}(t - \tau) \cdot \mathbf{d}_{\text{ion},\lambda}^*(\mathcal{R}, \mathbf{k}, t - \tau). \quad (19)$$

The contribution to the dipole velocity from either half-cycle is then obtained from (4) by taking the real part of (18) or (19) and integrating two thirds of an optical cycle. This will give different results as

$$\text{Re}[i\mathbf{v}_{\text{rec}}^* e^{-iS} \mathbf{F} \cdot \mathbf{d}_{\text{ion}}] \neq \text{Re}[i\mathbf{v}_{\text{rec}} e^{-iS} \mathbf{F} \cdot \mathbf{d}_{\text{ion}}^*] \quad (20)$$

when the molecular orbital is not symmetric along the polarization axis of the laser, which is exactly the case for asymmetric molecular orbitals. On the other hand, symmetric orbitals do yield the same dipole velocity in either half-cycle.

The above argument shows that one half-cycle will give a larger contribution to the HHG signal than the other given an asymmetric molecular orbital. The argument does not take into account the exchange harmonics [29, 31, 35] nor does it predict which half-cycle is the dominating one. It turns out that the harmonic signal is dominated by contributions corresponding to ionization in the half-cycle when the field points parallel to the dipole of the molecular orbital. In figure 2 this corresponds to the field pointing in the positive x direction, thus pulling electronic charge in the negative x direction. That the other half-cycle should be suppressed can be intuitively understood as a screening effect, where the main effect of the charge on the oxygen nucleus is to prevent tunnelling in the positive x direction. These observations are confirmed by the numerical results in section 3.

Reintroducing the Stark shift using (11) for $E_\lambda(t)$ in (7) results in the ionization potential being increased when

the field is parallel to the dipole of the molecular orbital and decreased when the field is antiparallel as illustrated in figure 3. Increasing (decreasing) the ionization potential will make it less (more) likely for the electron to tunnel into the continuum, so the Stark shift tends to counteract the geometric effect just described. To account for the field-induced shifts becomes increasingly important for higher field strengths. We should stress, however, that the term system-induced gating refers to the total gating effect caused by the response of the target system to the driving field, *including* the Stark shift. In more sophisticated models the modification of the ionization and recombination steps due to the presence of excited states should also be considered. The permanent dipole of the molecular potential (the dipole of the unrelaxed cation) can also play a role in determining the ionization dynamics, although this effect seems to be small for CO [44].

2.4. Field-induced gating

Field-induced gating refers to any gating mechanism, which relies on a waveform that deviates from a pure sinusoidal field. One example is the use of pulses that are so short that tuning the carrier envelope phase allows for the selection of one particular half-cycle [19]. Another example is that of using a polarization gate, where only part of the pulse has a linear polarization that allows the ionized electron to recombine with the molecular ion [16, 18].

We will restrict ourselves to a very simple field-induced gating scheme. Adding a small fraction of the second harmonic to the driving pulse with a relative carrier-envelope phase delay of zero leads to every other peak in the resulting field being enhanced (suppressed) as illustrated in figure 1. HHG scales exponentially with the maximal field strength due to the first step being a tunnelling process, making it possible to effectively weaken the HHG contribution from every other half-cycle. The control parameter is the amount of second harmonic that is added to the fundamental field.

In field-induced gating the target system is assumed to be inversion symmetric along the polarization axis. This means that polar molecules are only aligned, not oriented. An aligned molecule is the coherent superposition of two antiparallel oriented molecules, so by (3) the total HHG signal is a coherent sum of the individual signals [12]. At a given half-cycle, each orientation will experience either a parallel or an antiparallel electric field leading to system-induced gating as described in section 2.3. Assuming that the Stark shift is negligible and referring to the orientations in figure 3, P1 will dominate over A1 in the positive half-cycle, and P2 will dominate over A2 in the negative half-cycle. The gating felt by each orientation is thus reversed in neighbouring half-cycles, ensuring the overall inversion symmetry of the HHG process.

The symmetry between the two orientations is broken in field-induced gating due to the broken symmetry of the electric field. Assuming that the maximal field-strength is in the negative x direction, and ignoring the effect of the Stark shift, the contribution from P1 will still dominate A1, and P2 will dominate A2. However, P2 will dominate P1 due to the larger field-strength in the negative x direction. In the

limit where the system-induced gating is very strong, and the asymmetry of the field is very large, the only HHG contribution will be from the P2 geometry, making the HHG signal from field-induced gating indistinguishable to that from system-induced gating. The correspondence between the two gating mechanisms is only approximate, however, as the Stark shift weakens the effectiveness of system-induced gating. The exact weight from the different orientations and half-cycles on the total signal is determined by the size of the Stark shift.

3. Numerical results

Here we present numerical results for CO aligned along the polarization axis of the driving laser. The internuclear distance is set to the equilibrium distance 1.1283 Å. The molecular orbitals are obtained using standard quantum chemistry software [43]. The HOMO is a 3σ orbital shown in figure 2. The vertical ionization potential is 14.014 eV. The HOMO-1 is a degenerate 1π orbital with a nodal plane along the internuclear axis. The nodal plane means that the contribution from the HOMO-1 in the polarization direction is heavily suppressed [5]. Contributions from lower lying orbitals are suppressed by the higher ionization potential, so we only consider the contribution from the HOMO.

The dipole and polarizability of the HOMO are found by calculating the ionization potential for a range of static electric fields and fitting the resulting curve to a second-order polynomial. This yields a dipole of 1.1287 au pointing from C to O and a polarizability with $\alpha_{\parallel} = 3.2332$ au and $\alpha_{\perp} = 2.7668$ au. Note that the HOMO dipole points opposite to and is much larger than the molecular dipole $0.112\text{D} = 0.0441$ au. In our model the molecular dipole is only relevant if the orientational distribution due to an alignment pulse is needed.

The 800 nm driving pulse is taken to be linearly polarized along the x axis. The trapezoidal envelope is sketched in figure 1. Three optical cycles are allowed for ramp-up and three cycles for ramp-down, with five cycles at full field strength. The relatively long pulse ensures that carrier envelope phase effects play a minor role in our calculations. The field-strength is determined by the maximal intensity, which is set to 2.0×10^{14} W cm⁻² as default. Two-colour fields as the one in figure 1 are made by adding the second harmonic with the same trapezoidal envelope and a relative carrier envelope phase of zero.

In section 3.1 we directly compare results obtained with and without including the Stark effect in (7) using (11). The Stark shift is included in sections 3.2 and 3.3, where system-induced and field-induced gating are compared, and our cutoff extension scheme presented.

3.1. Importance of the Stark shift

A common way of analysing HHG is to perform a Gabor transform [7, 45, 46]. A plot of the Gabor transform yields information on the time at which a given harmonic is emitted. Figure 4 shows such a plot without inclusion of the Stark shift given the orientation in figure 2. The times at which the

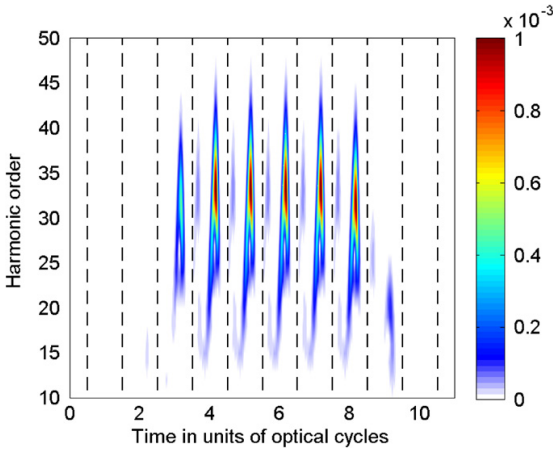


Figure 4. Gabor analysis illustrating system-induced gating when the Stark shift is omitted (7). The driving field is an 800 nm pulse with eleven optical cycles and five optical cycles in the plateau. The peak intensity is 2.0×10^{14} W cm $^{-2}$. The molecular target is the HOMO of CO oriented as in figure 2. The vertical dashed lines indicate the times at which the electric field peaks in the positive x direction. It is clearly seen that harmonic emission is restricted to once every other half-cycle due to the asymmetry of the target.

electric field peaks in the positive x direction are indicated by vertical dashed lines. As seen from the figure, harmonics are predominantly emitted every other half-cycle, corresponding to ionization in the positive half-cycle and recombination roughly two thirds of an optical cycle later. Due to the asymmetry of the HOMO, the molecule itself acts as a gate for the HHG process. This is in excellent agreement with the description of system-induced gating in section 2.3.

The geometric effect described in section 2.3 always favours the parallel geometry in figure 3. The Stark effect, however, increases the effective ionization potential in the parallel geometry, resulting in a weakening of the system-induced gating. Figure 5 shows the Gabor analysis when the Stark shift is included in (7) using (11). It is immediately clear that half-cycles suppressed in figure 4 now contribute much more to the spectrum.

Spectra obtained with and without the Stark shift (not shown) exhibit differences in the detailed structure but it is difficult to make any quantitative comparison. Roughly speaking, the spectrum for oriented CO is more rugged when the Stark shift is included. This can be understood as a consequence of added interference between half-cycles.

3.2. Comparing gating mechanisms

The two different gating mechanisms both imply a broken symmetry, which should result in even harmonics in the HHG spectrum. Figure 6 serves as a reference spectrum in which the target CO molecule is aligned and the driving field a trapezoidal pulse with 11 cycles as described in the caption. Even harmonics are suppressed due to the inversion symmetry of both target and field [6, 7]. Figure 7 shows the HHG spectrum when CO is oriented, thus causing system-induced gating. The even harmonics are due to the broken

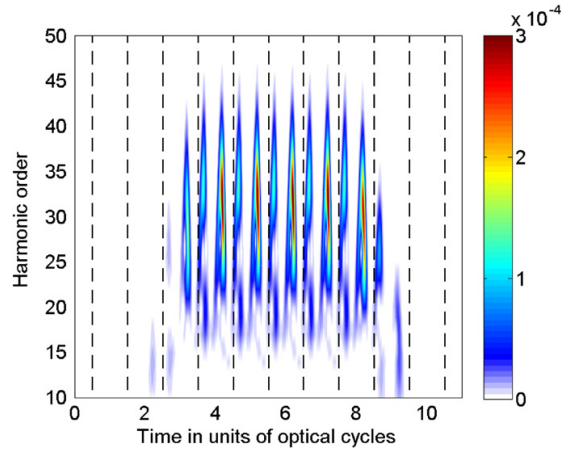


Figure 5. Gabor analysis illustrating the weakening of system-induced gating caused by the Stark shift. All parameters are the same as in figure 4 except that the Stark shift is now included in (7) using (11) for $E(t)$.

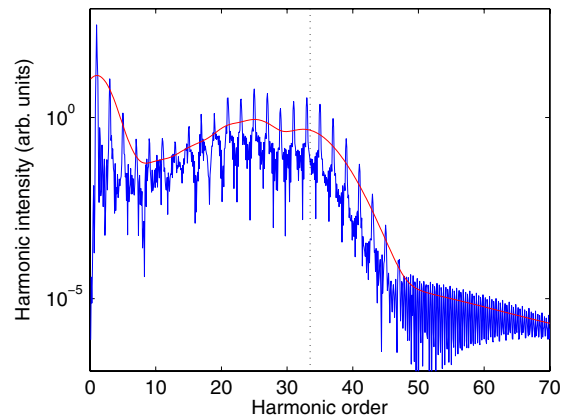


Figure 6. Reference HHG spectrum from aligned CO calculated with the Stark shift included in (7) as dictated by (11). The electric field is an 800 nm pulse with eleven optical cycles and a trapezoidal envelope with five optical cycles in the plateau. The peak intensity is 2.0×10^{14} W cm $^{-2}$. Only odd harmonics appear due to the inversion symmetry of both target and field. The smooth curve is obtained by averaging over neighbouring peaks. The vertical broken line indicates the harmonic cutoff calculated using $\omega_{\max} = I_p + 3.17U_p$. The Stark effect is not included in estimating the cutoff.

inversion symmetry of the target. Figure 8 shows the spectrum from aligned CO with field-induced gating implemented using 1% of the second harmonic as in figure 1. The even harmonics are due to the broken inversion symmetry of the field.

Figures 7 and 8 both contain even harmonics but differ in their detailed structure. Figure 9 shows a Gabor analysis of the two orientations in the field-induced gating case. One orientation, figure 9(a), is seen to have its system-induced gating *counteracted* by the field-induced gating, and the other orientation, figure 9(b), to have its system-induced gating

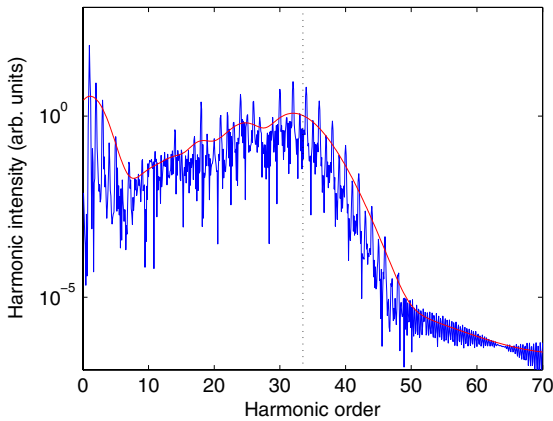


Figure 7. HHG spectrum using system-induced gating. All parameters are the same as in figure 6 except that the CO molecule is now oriented, making even harmonics possible due to the broken inversion symmetry of the target. The vertical broken line indicates the harmonic cutoff calculated using $\omega_{\max} = I_p + 3.17U_p$. The Stark effect is not included in estimating the cutoff.

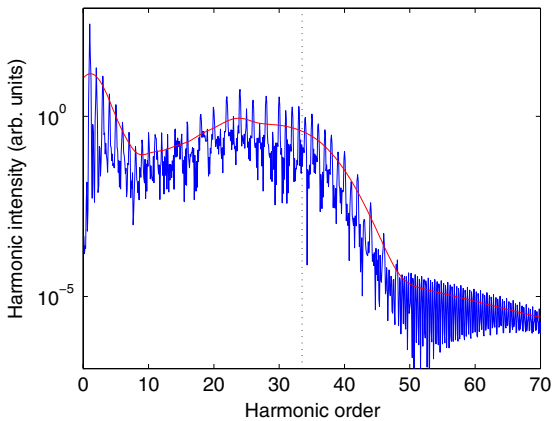


Figure 8. HHG spectrum using field-induced gating. The target molecule is aligned as in figure 6 but the driving field has had 1% of its second harmonic added, resulting in the field in figure 1. The broken inversion symmetry of the field allows even harmonics to appear in the spectrum. The vertical broken line indicates the harmonic cutoff calculated using $\omega_{\max} = I_p + 3.17U_p$. The Stark effect and the second harmonic are not included in estimating the cutoff.

enhanced. In the limit of perfect system-induced gating only the latter orientation would contribute to the spectrum, as described in section 2.4. The exact weight on each orientation is determined by the effectiveness of the system-induced gating, which depends on the Stark shift as discussed in section 3.1.

3.3. Extending the harmonic cutoff

We propose to extend the harmonic cutoff by suppressing the system-induced gating of an oriented polar molecule using field-induced gating as in figure 9(a). The combined effect is

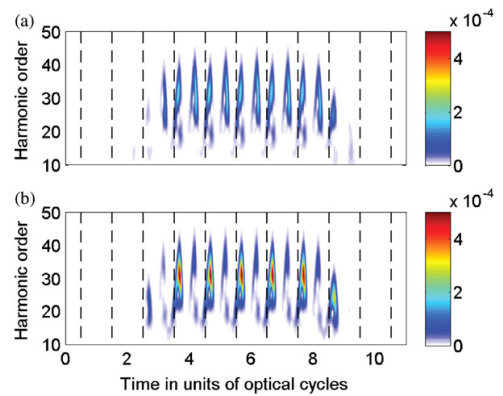


Figure 9. Gabor analysis illustrating the different dynamics of opposite orientations in field-induced gating. The total response of the aligned molecule is the coherent sum of the two orientations. The electric field is the same as that in figures 1 and 8. (a) The HOMO dipole is oriented in the positive x direction as in figure 2. The Gabor analysis would be the one shown in figure 5 in the absence of the second harmonic, so field-induced gating clearly counteracts system-induced gating. (b) The HOMO dipole is oriented in the negative x direction causing field-induced gating to enhance system-induced gating.

to suppress tunnelling into the continuum in both half-cycles, thus suppressing both HHG and ionization. Ionization of the target medium is one of the main restrictions in attaining high cutoffs as it causes depletion of the target medium as well as defocusing of the laser pulse due to free electrons. As a proof-of-principle calculation we have used MO-ADK theory [47, 48] to calculate the ionization rates for oriented CO with and without the added second harmonic, confirming a suppressed ionization rate. According to the MO-ADK calculations an electric field with a peak intensity of $2.4 \times 10^{14} \text{ W cm}^{-2}$ with 1% added second harmonic causes the same amount of ionization as the original single-colour field with a peak intensity of $2.0 \times 10^{14} \text{ W cm}^{-2}$. The corresponding spectrum is shown in figure 10. Comparison with figure 6 shows an increase in cutoff of roughly five harmonic orders, corresponding to a 14% extension. Note that this increase can be entirely ascribed to the higher intensity of the 800 nm component of the driving field, as the harmonic cutoff is correctly predicted by the usual cutoff rule.

The size of the obtainable cutoff extension depends on the exact reduction of the ionization rate in a combined system-induced and field-induced gating scheme. Such a calculation is beyond the scope of this paper. The scheme itself is fairly independent of the detailed dynamics, however. As long as the oriented target molecule has a preferred half-cycle, suppression of this half-cycle with a specially tailored field will allow for higher intensities and thus higher cutoffs. This method can also be combined with driving pulses in the mid-infrared, which also lead to higher cutoff energies [49]. Finally, the argument does not depend on long pulses, so short-pulse schemes [19] for obtaining quasi-continuous spectra will also work, as will double optical gating schemes [18].

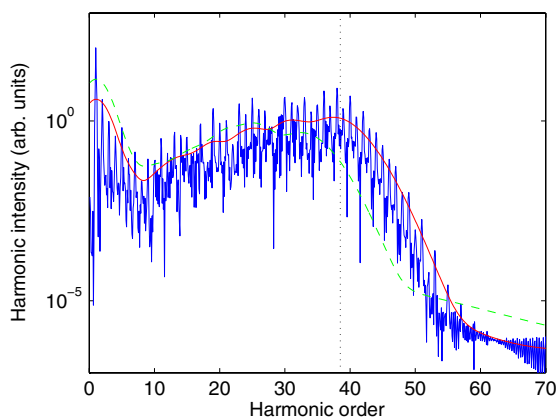


Figure 10. HHG spectrum illustrating the extension of the harmonic cutoff in a combined system-induced and field-induced gating scheme. The target CO molecule is oriented as in figure 2. The two-colour field is chosen so as to counteract system-induced gating, resulting in a reduced ionization rate as described in the text. Using the combined gating scheme the peak intensity of the 800 nm component can be raised to $2.4 \times 10^{14} \text{ W cm}^{-2}$ before the ionization rate is the same as in figure 6. The vertical dashed line indicates the harmonic cutoff calculated using $\omega_{\text{max}} = I_p + 3.17U_p$. The Stark effect and the second harmonic are not included in estimating the cutoff. The dashed line is the smoothed spectrum from figure 6, confirming a 14% extension of the harmonic cutoff energy.

4. Conclusion and outlook

We have addressed the problem of describing HHG from polar molecules in intense laser fields. The conventional strong-field approximation [4] is not expected to be valid for polar molecules due to the interaction between the permanent dipole of the field-free molecular orbitals and the driving field. The Lewenstein model is extended to polar molecules by applying a quasi-static approximation in which the energy levels of the molecular orbitals are Stark shifted according to the instantaneous value of the field. Qualitatively, the effect of the Stark shift is to increase (decrease) the ionization potential in half-cycles where the field points parallel (antiparallel) to the dipole of the molecular orbital thus causing a decreased (increased) contribution to the HHG signal. The second-order Stark shift causes a very slight suppression of the HHG signal for both half-cycles and is largely negligible. Our model reduces to the standard Lewenstein model for non-polar molecules and corresponds to first-order perturbation theory in the limit of small linear Stark shifts.

The importance of including the Stark shift is evident when considering gating mechanisms. The asymmetric charge distribution from an oriented molecule leads to suppressed HHG signal in half-cycles where the field points opposite to the dipole of the molecular orbital. This leads to a geometric gating which we refer to as system-induced gating. We show that the Stark shift suppresses the HHG signal in half-cycles where the field is parallel to the orbital dipole so the effectiveness of system-induced gating is reduced by the Stark shift. We also compare system-induced to field-induced

gating, where the symmetry of the laser field is broken rather than that of the target. It is shown that even though this broken symmetry is very similar to that in system-induced gating, the coherent nature of the HHG process means that the dynamics in a field-induced gating setup is more complicated.

Finally, we propose a novel scheme for extending the harmonic cutoff by combining system-induced and field-induced gating. By suppressing half-cycles in which an oriented molecule is most easily ionized, it is possible to go to higher intensities without suffering the usual drawbacks. This method is very general and does not depend on the details of our modelling. A proof-of-principle calculation indicates that increases on the order of 14% are obtainable.

In our current work we have focused on the influence that the Stark shift has on the spectrum. There is currently much interest in gaining information about HHG from the phases of individual harmonics. Such phases are experimentally available using e.g. the RABITT technique [50] or by performing mixed gas experiments [51]. In order to extract the influence of the Stark shift on the harmonic phases, it is necessary to have a reference that is uninfluenced by the Stark shift. Krypton would be a good second species in a mixed gas experiment as it has nearly the same ionization potential as CO while only experiencing weak higher order Stark shifts.

Acknowledgments

The authors would like to thank Mahmoud Abu-samha for calculating the dipole and polarizabilities of CO and Christian Bruun Madsen for helpful discussions.

References

- [1] Gibson E A *et al* 2003 *Science* **302** 95
- [2] Takahashi E J, Kanai T, Ishikawa K L, Nabekawa Y and Midorikawa K 2008 *Phys. Rev. Lett.* **101** 253901
- [3] Corkum P B 1993 *Phys. Rev. Lett.* **71** 1994
- [4] Lewenstein M, Balcou Ph, Ivanov M Y, L'Huillier A and Corkum P B 1994 *Phys. Rev. A* **49** 2117
- [5] Madsen C B and Madsen L B 2007 *Phys. Rev. A* **76** 043419
- [6] Alon O E, Averbukh V and Moiseyev N 1998 *Phys. Rev. Lett.* **80** 3743
- [7] Kamta G L and Bandrauk A D 2004 *Phys. Rev. A* **70** 011404
- [8] Kreibich T, Lein M, Engel V and Gross E K U 2001 *Phys. Rev. Lett.* **87** 103901
- [9] Kamta G L, Bandrauk A D and Corkum P B 2005 *J. Phys. B: At. Mol. Opt. Phys.* **38** L339
- [10] Heslar J, Carrera J, Telnov D and Chu S 2007 *Int. J. Quantum Chem.* **107** 3159
- [11] Lan P, Lu P, Cao W, Li Y and Wang X 2007 *Phys. Rev. A* **76** 021801
- [12] Madsen C B, Mouritzen A S, Kjeldsen T K and Madsen L B 2007 *Phys. Rev. A* **76** 035401
- [13] Zhang Q, Lu P, Hong W, Liao Q and Wang S 2009 *Phys. Rev. A* **80** 033405
- [14] Kim I J, Kim C M, Kim H T, Lee G H, Lee Y S, Park J Y, Cho D J and Nam C H 2005 *Phys. Rev. Lett.* **94** 243901
- [15] Dudovich N, Smirnova O, Levesque J, Mairesse Y, Ivanov M Y, Villeneuve D M and Corkum P B 2006 *Nat. Phys.* **2** 781
- [16] Dudovich N, Levesque J, Smirnova O, Zeidler D, Comtois D, Ivanov M Y, Villeneuve D M and Corkum P B 2006 *Phys. Rev. Lett.* **97** 253903



Two-center minima in harmonic spectra from aligned polar molecules

Adam Etches, Mette B. Gaarde, and Lars Bojer Madsen

Physical Review A **84**, 023418 (2011)

Two-center minima in harmonic spectra from aligned polar moleculesAdam Etches,^{1,2} Mette B. Gaarde,² and Lars Bojer Madsen^{1,*}¹*Lundbeck Foundation Theoretical Center for Quantum System Research, Department of Physics and Astronomy, Aarhus University, 8000 Aarhus C, Denmark*²*Department of Physics and Astronomy, Louisiana State University, Baton Rouge, Louisiana 70803-4001, USA*
(Received 6 May 2011; published 29 August 2011)

We extend a model of two-center interference to include the superposition of opposite orientations in aligned polar molecules. We show that the position of the minimum in the harmonic spectrum from both aligned and oriented CO depends strongly on the relative recombination strength at different atoms, not just the relative phase. We reinterpret the minimum in aligned CO as an interference between opposite orientations, and obtain good agreement with numerical calculations. Inclusion of the first-order Stark effect shifts the position of the interference minimum in aligned CO even though aligned molecules do not possess total permanent dipoles. We explain the shift in terms of the phase that the electron of *oriented* CO accumulates due to the Stark effect.

DOI: [10.1103/PhysRevA.84.023418](https://doi.org/10.1103/PhysRevA.84.023418)

PACS number(s): 33.80.Rv, 42.65.Ky, 42.65.Re

I. INTRODUCTION

Two-center interference minima are an important spectral signature in high-harmonic spectra from homonuclear molecules [1,2]. Two-center interference is often described within the framework of the three-step model, in which an electron (i) tunnels through the effective barrier formed by the molecular potential and a strong laser field, (ii) picks up kinetic energy in the continuum, and (iii) emits high-energy photons upon recombination into the ground state [3,4]. The harmonic emission splits into contributions from recombination at each atomic center, with the possibility of destructive interference between different centers. The position of the minimum depends on the momentum of the returning continuum electron, and the projected internuclear distance [1,2].

It has recently been shown within the Lewenstein model [5] that two-center interference in oriented polar molecules is more complicated than in aligned homonuclear molecules. The added complication is caused by different intrinsic recombination phases at different atoms, which can shift the interference minimum [6]. We show that different recombination strengths also strongly affect the minimum position, and extend the analysis to the case of aligned polar molecules, which have a well-defined alignment of the internuclear axis, but not a well-defined head-to-tail direction. Field-free molecular alignment is much easier to obtain experimentally than full orientation [7]. We obtain a simple equation for the prediction of the minimum position by reinterpreting the minimum as an interference between opposite orientations.

Polar molecules differ from homonuclear molecules in that their molecular orbitals have permanent dipole moments that interact strongly with electric fields. This requires that a model of high-order harmonic generation (HHG) from polar molecules should include the effect of the laser field on the ground state, something which is typically unimportant for atomic and homonuclear systems. The response of the ground state to the laser field can be included to lowest order by adiabatically Stark shifting the energy levels of the field-free

molecular orbitals to the instantaneous value of the electric field [8]. The influence of Stark shifts on strong-field ionization has recently been investigated in tunneling theory [9–12], in the strong-field approximation [13], and in calculations using the time-dependent Schrödinger equation in the single-active electron approximation [14].

In our present calculations the Stark effect shifts the interference minimum in aligned CO by as much as three harmonic orders even though aligned molecules do not possess total permanent dipoles. The shift is explained in terms of the Stark phase that the highest occupied molecular orbital (HOMO) of *oriented* CO accumulates between the ionization and recombination step. Our results indicate that inclusion of the Stark effect is important when modeling spectral features of HHG from polar molecules.

The paper is organized as follows. We briefly describe how we calculate HHG spectra in Sec. II, then present our model of two-center interference from aligned molecules in Sec. III. In Sec. IV we discuss how the Stark effect shifts the position of the minimum, and explain the shift in terms of the Stark phase accumulated by an electron between ionization and recombination. We summarize our results in Sec. V. Two derivations are relegated to Appendix.

Atomic units ($\hbar = e = m_e = a_0 = 1$) are used throughout.

II. CALCULATING SPECTRA

We use CO to illustrate various aspects of HHG from polar molecules. For this proof-of-principle study we restrict ourselves to including the HOMO, ignoring ionization from lower-lying states [15–18] as well as recombination into excited bound states [19]. The HOMO is a 3σ orbital with vertical ionization potential $I_p = 14.014$ eV, a permanent dipole $\mu = 1.1287$ a.u. pointing from C to O, and static polarizabilities $\alpha_{\parallel} = 3.2332$ a.u. and $\alpha_{\perp} = 2.7668$ a.u. parallel and perpendicular to the internuclear axis [8]. The nuclei are frozen to the equilibrium distance $R = 1.1283$ Å. The wave function is obtained using a triple- ζ valence basis set in the quantum chemistry software package GAMESS-US [20].

The driving pulse is chosen with a linear polarization along the x axis, peak intensity 4×10^{14} W/cm², and a wavelength of 800 nm. The electric field has a \cos^2 envelope with 10

*bojer@phys.au.dk

optical cycles FWHM. The carrier envelope phase delay has no impact on our results for such long pulses, and is set to zero.

The spectrum $S_{\mathbf{n}}(\omega)$ of the harmonic component along a given direction \mathbf{n} from a single oriented molecule is given by

$$S_{\mathbf{n}}(\theta; \omega) = |A_{\mathbf{n}}(\theta; \omega)|^2, \quad (1)$$

where $A_{\mathbf{n}}(\theta; \omega)$ is the projection onto \mathbf{n} of the Fourier transform of the time-dependent expectation value of the dipole velocity operator $\langle \hat{v}_{\text{dip}}(\theta; t) \rangle$ [21]. Due to the cylindrical symmetry of σ orbitals, the molecular orientation is defined entirely by the angle θ between the laser polarization axis and the nuclear displacement $\mathbf{R} = \mathbf{R}_2 - \mathbf{R}_1$. Reference [8] explains how to calculate $\langle \hat{v}_{\text{dip}}(\theta; t) \rangle$ using an extended Lewenstein model that includes the time-dependent Stark shifts felt by the molecular orbitals. Short trajectories are selected with a window function, which suppresses trajectories that have excursion times longer than approximately two-thirds of an optical cycle.

Spectra for CO at two different orientations are plotted in Fig. 1. Figure 1(a) shows a clear two-center interference minimum from CO oriented perpendicular to the laser polarization axis. However, as soon as the molecule is oriented slightly away from perpendicular in Fig. 1(b), the minimum becomes less pronounced. Also, Fig. 1(b) contains even harmonics due to the broken inversion symmetry of the target molecule [8,22,23].

The spectrum from an aligned molecule is obtained by adding the contribution from opposite orientations coherently [24,25]:

$$S_{\mathbf{n},\text{aligned}}(\theta; \omega) = |A_{\mathbf{n}}(\theta; \omega) + A_{\mathbf{n}}(\theta + \pi; \omega)|^2. \quad (2)$$

The effect of alignment is seen in Fig. 2. The spectra of aligned and oriented CO are the same in the perpendicular geometry, but at 86° they differ substantially. The first observation is that the spectrum in Fig. 2(b) contains only odd harmonics, which is

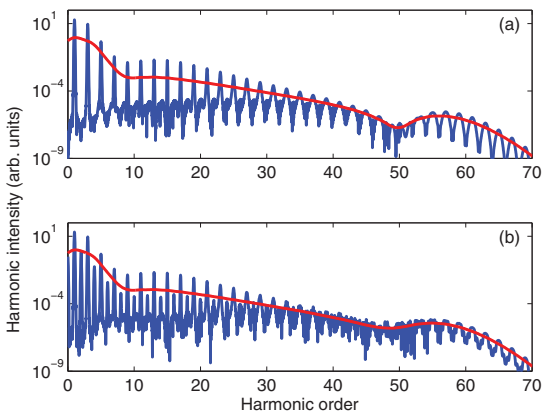


FIG. 1. (Color online) Parallel components of HHG spectra from CO oriented at (a) $\theta = 90^\circ$ and (b) $\theta = 86^\circ$ to the laser polarization axis. The smooth (red) curves are obtained by averaging the spectra over several harmonic orders. The 800 nm driving laser pulse has a peak intensity of 4×10^{14} W/cm 2 . Short trajectories are selected using a window function, and the Stark effect is not included.

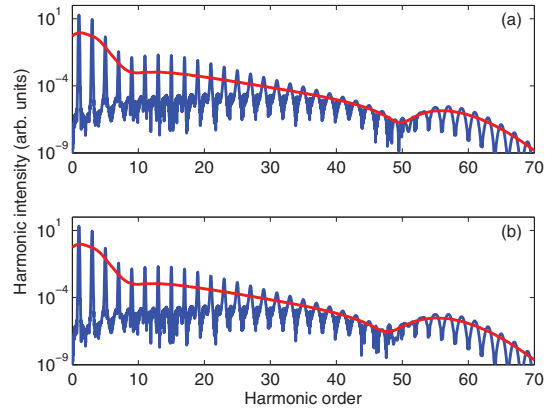


FIG. 2. (Color online) Parallel components of HHG spectra from CO aligned at (a) $\theta = 90^\circ$ and (b) $\theta = 86^\circ$ to the laser polarization axis. All other parameters are the same as those in Fig. 1.

due to the inversion symmetry of the aligned target [8,22,23]. The second observation is that the interference minimum is much clearer than for oriented CO.

III. TWO-CENTER MINIMUM IN ALIGNED MOLECULES

We now present a simple model of the interference minimum in Fig. 2, and show that it can be thought of either as an interference between recombination at different atoms, or as an interference between opposite orientations.

It is a common assumption that two-center interference minima are completely determined by the recombination step into the ground state orbital. This assumption needs to be justified for polar molecules due to the different classes of electron trajectories in the continuum [26–28]. There are four different trajectories for CO, each one starting at either C or O, and recombining at either C or O. The contribution from each class of trajectories is plotted in Fig. 3 for CO oriented perpendicular to the laser polarization axis. Trajectories starting at the carbon atom completely dominate the spectrum due to a larger ionization dipole matrix element at carbon. Removing the trajectories starting at oxygen has very little impact on the shape and position of the interference minimum, showing that the interference is not caused by the ionization step. For a detailed discussion of trajectories beginning and ending on the two different atoms, see Refs. [26–28].

The trajectory contributions in Fig. 3 are obtained using the extended stationary-phase approximation [26], in which the trajectories going from one atom to another acquire an extra component to the momentum. Using the conventional stationary-phase approximation, and thus neglecting this drift momentum, has a negligible effect on the shape and position of the interference minimum. Also, short trajectories were selected using a window function, ruling out interference between long and short trajectories. These observations show that continuum dynamics are not responsible for the interference minimum either.

We now turn to the recombination step, having ruled out interferences in the continuum as well as in the ionization

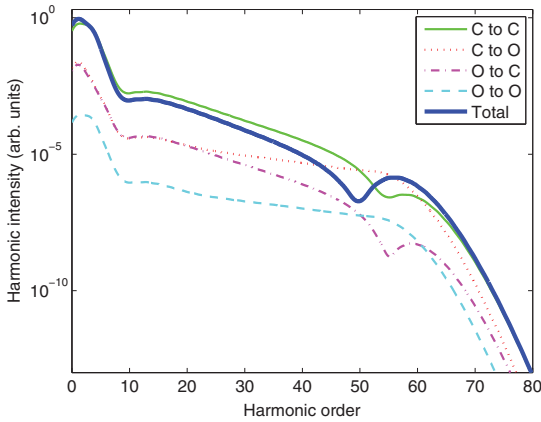


FIG. 3. (Color online) Parallel components of the spectra associated with the four trajectories of CO oriented perpendicular to the laser polarization axis. The molecular spectrum is the coherent sum of all four contributions, and is dominated by trajectories that start with ionization at the carbon atom. Short trajectories are selected, and the Stark effect is not included.

step. First the oriented HOMO $|\psi, \theta\rangle$ is expanded as a linear combination of atomic orbitals (LCAO) $|\psi_n, \theta\rangle$:

$$|\psi, \theta\rangle = \sum_n c_n |\psi_n, \theta\rangle. \quad (3)$$

The sum is over atomic centers. The recombination dipole velocity matrix element between $|\psi, \theta\rangle$ and a plane wave $|\mathbf{k}\rangle$ then takes the form

$$\langle \mathbf{k} | \hat{\mathbf{v}}_{\text{dip}} | \psi, \theta \rangle = \sum_n e^{i(\mathbf{k} \cdot \mathbf{R}_n + \phi_n(\mathbf{k}, \theta))} |c_n \langle \mathbf{k} | \hat{\mathbf{v}}_{\text{dip}} | \psi_n, \theta \rangle|. \quad (4)$$

The calculation is given in Appendix. The phase $\mathbf{k} \cdot \mathbf{R}_n$ is due to the atomic position \mathbf{R}_n , and $\phi_n(\mathbf{k}, \theta)$ is an intrinsic recombination phase relating to the LCAO centered on atom n . Equation (4) shows that the harmonic emission from different atoms interfere, causing maximal destructive interference at a particular momentum \mathbf{k} for a fixed angle θ .

The key to understanding the interference in aligned polar molecules is to realize that the dipole velocity matrix elements of opposite orientations are closely related:

$$\langle \mathbf{k} | \hat{\mathbf{v}}_{\text{dip}} | \psi, \theta + \pi \rangle = \langle \mathbf{k} | \hat{\mathbf{v}}_{\text{dip}} | \psi, \theta \rangle^*. \quad (5)$$

The calculation is given in Appendix. Together, Eqs. (2), (4), and (5) show that the recombination dipole velocity matrix element of an aligned molecule is given by

$$\langle \mathbf{k} | \hat{\mathbf{v}}_{\text{dip}} | \psi, \theta \rangle_{\text{aligned}} = \text{Re}(\langle \mathbf{k} | \hat{\mathbf{v}}_{\text{dip}} | \psi, \theta \rangle) \quad (6)$$

$$= \sum_n \cos[\mathbf{k} \cdot \mathbf{R}_n + \phi_n(\mathbf{k}, \theta)] |c_n \langle \mathbf{k} | \hat{\mathbf{v}}_{\text{dip}} | \psi_n, \theta \rangle|. \quad (7)$$

The position of the two-center minimum is determined by the value of \mathbf{k} that minimizes the absolute value of Eq. (7). The simplest approach would be to ignore the recombination strengths $|c_n \langle \mathbf{k} | \hat{\mathbf{v}}_{\text{dip}} | \psi_n, \theta \rangle|$, and claim that harmonic emission

from one atom cancels out the harmonic emission from another when

$$|\mathbf{k}|R \cos(\theta) + \phi_2(\mathbf{k}, \theta) - \phi_1(\mathbf{k}, \theta) = (2m + 1)\pi \quad (8)$$

for any integer m . In this approximation, the same result is obtained for oriented molecules using Eq. (4), and was first presented in Ref. [6]. However, the absolute values of Eqs. (4) and (7) do not generally have a minimum at the same location, nor can they be predicted entirely from recombination phases. The reason for this is that the recombination strengths in Eqs. (4) and (7) generally have different $|\mathbf{k}|$ dependencies at different atomic centers. The problem disappears in the case of homonuclear molecules, where the matrix norms are identical.

The following example illustrates our point. Figure 4 shows the relevant recombination dipole velocity matrix elements for CO oriented at $\theta = 86^\circ$. The solid (blue) curves are the norm and the phase of the total HOMO matrix element of CO. The dashed (green) curves are the norm and phase of the matrix element of the LCAO on carbon, and the dash-dotted (magenta) curves on oxygen. The solid (blue) curve in Fig. 4(a) has a minimum at $|\mathbf{k}| = 2.08$ a.u. According to Eq. (8), the minimum should be located at the momentum $|\mathbf{k}|$ for which the phase difference between the carbon and oxygen matrix elements in Fig. 4(b) is π . This gives a predicted minimum at $|\mathbf{k}| = 1.86$ a.u., which is in poor agreement with the actual position.

The interference minimum in aligned polar molecules can also be thought of as an interference between opposite orientations. Equation (6) shows that the interference minimum appears whenever the real part of the recombination matrix element of the total molecular orbital $\langle \mathbf{k} | \hat{\mathbf{v}}_{\text{dip}} | \psi, \theta \rangle$ is zero:

$$\text{Re}(\langle \mathbf{k} | \hat{\mathbf{v}}_{\text{dip}} | \psi, \theta \rangle) = 0. \quad (9)$$

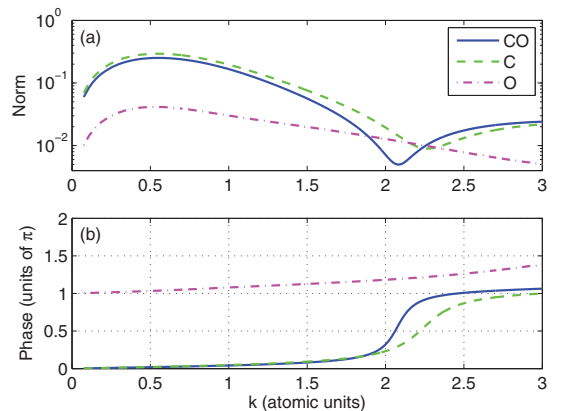


FIG. 4. (Color online) (a) Norms of the dipole velocity matrix elements for CO oriented at $\theta = 86^\circ$ to \mathbf{k} . The solid (blue) curve is the matrix element with the entire HOMO $\langle \mathbf{k} | \hat{\mathbf{v}}_{\text{dip}} | \psi, 86^\circ \rangle$, the dashed (green) curve is the matrix element with the LCAO on carbon $\langle \mathbf{k} | \hat{\mathbf{v}}_{\text{dip}} | \psi_1, 86^\circ \rangle$, and the dash-dotted (magenta) the matrix element with the LCAO on oxygen $\langle \mathbf{k} | \hat{\mathbf{v}}_{\text{dip}} | \psi_2, 86^\circ \rangle$. (b) Phases of the same matrix elements. The dashed and dash-dotted curves are given by $\mathbf{k} \cdot \mathbf{R}_n + \phi_n(\mathbf{k}, \theta)$.

According to the solid (blue) curve in Fig. 4(b), this happens at $|\mathbf{k}| = 2.06$ a.u. Using the relation $\hbar\omega = 0.5|\mathbf{k}|^2 + I_p$ to convert into photon energy, this corresponds to a minimum at $\omega = 46.3\omega_0$. The actual position of the minimum is $47.8\omega_0$, as determined by the averaged spectrum in Fig. 2. For comparison, Eq. (8) yields a prediction of $37.5\omega_0$. Equation (9) is clearly more precise at predicting the minimum position than Eq. (8).

Now we are also able to understand why the interference minimum is stronger for aligned CO in Fig. 2(b) than for oriented CO in Fig. 1(b). The strength of the interference minimum in oriented CO is determined by the minimal value of the matrix element norm. As illustrated in Fig. 4, this minimal value is not necessarily zero. For aligned CO only the real part has to be zero, which is obtained exactly, hence two-center interference minima are generally expected to be stronger for aligned than for oriented polar molecules.

Equation (9) is more precise than Eq. (8) because no assumptions are made on the recombination strengths at different atomic centers. One might argue that it would be more natural to use Eq. (7) directly, and read off the minimum in the matrix element norm of the *aligned* molecule rather than focus on the matrix element phase of the *oriented* molecule. However, we show in Sec. IV that the influence of the Stark effect on the minimum position is more easily understood in terms of the recombination phase of the oriented molecule.

IV. IMPORTANCE OF THE STARK EFFECT

Equation (9) shows that the interference minimum from an aligned polar molecule is expected to depend on the phase of the recombination matrix element of the *oriented* molecule. This begs the question whether phases from other steps of the HHG process influence the final position of the minimum.

One possible concern is the potential-energy shift related to the use of the length gauge for the laser-electron interaction Hamiltonian [26,27]. However, this potential-energy shift is mostly relevant at large internuclear distances [26]. The subcycle dynamics of the harmonic emission from CO oriented parallel to the laser polarization is shown in Figs. 4 and 5 of Ref. [8]. If the choice of gauge were important, then the relative emission strength between neighboring half-cycles would change when the molecule is flipped. The reason for this asymmetry is that the origin is placed in the center of mass. We do not observe such a change in our calculations (not shown), indicating that the potential-energy shift is not an issue for CO.

Another possible phase is due to the Stark shift felt by the polar HOMO. Figure 5 shows the position of the interference minimum in aligned CO calculated using an extended Lewenstein model [8] with the pulse parameters from Sec. II. Including the Stark effect to first order is seen to shift the interference minimum by as much as three harmonic orders. Including the second-order Stark shift has negligible influence on the present spectra.

We propose that the shift of the interference minimum can be understood in terms of the first-order Stark shift that the polar HOMO experiences due to the driving pulse. An electron trajectory starting with ionization at time t' , and ending with

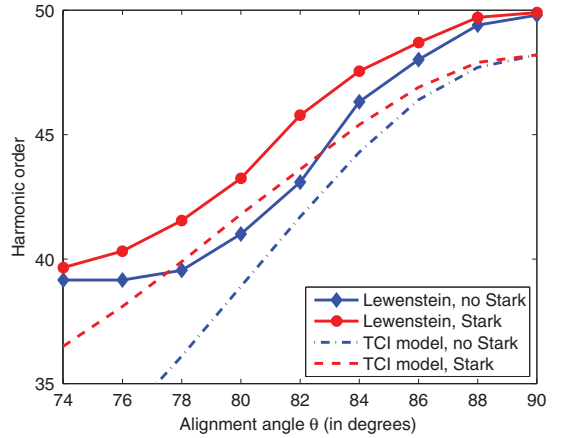


FIG. 5. (Color online) Position of the interference minimum (of the smoothed spectrum) from aligned CO with and without including the Stark effect in the Lewenstein model. Short trajectories have been selected. Also plotted are the predicted minima positions using a two-center interference (TCI) model based on Eq. (9).

recombination at time t , will accumulate a first-order Stark phase [8] given by

$$\begin{aligned} \Phi_{\text{Stark}} &= \int_{t'}^t \boldsymbol{\mu} \cdot \mathbf{F}(t'') dt'' \\ &= -\mu \cos(\theta)[A(t) - A(t')]. \end{aligned} \quad (10)$$

$\mathbf{A}(t)$ is the vector potential of the driving field $\mathbf{F}(t) = -\partial_t \mathbf{A}(t)$, which is linearly polarized along the x axis.

The accumulated Stark phase in Eq. (11) can be estimated using classical trajectories from the three-step model [3,4]. In short, we consider a single cycle of the electric field, and calculate the return time t , and return energy E_{kin} , of a classical electron being liberated at time t' with zero kinetic energy. The accumulated phase is entirely determined by t , t' and θ through Eq. (11), and mapped onto photon energy using $\hbar\omega = E_{\text{kin}} + I_p$. The result is plotted as a smooth (red) curve in Fig. 6 for $\theta = 82^\circ$. The predicted Stark phase only depends on the orientation angle through an overall factor of $\cos(\theta)$.

An alternative estimate based on the Lewenstein model is obtained by calculating the harmonic spectra from oriented CO with and without including the Stark effect. As neighboring half-cycles experience opposite signs of the first-order Stark shift, we restrict the ionization step to times t' at which the x component of the electric field $\mathbf{F}(t')$ is positive. This singles out continuum trajectories that share the same sign of the Stark shift. Short trajectories are selected using a window function. The difference in harmonic phase between the two calculations is plotted in Fig. 6 as an irregular (blue) curve. The agreement with Eq. (11) is quite good, especially when keeping in mind the simplicity of the model, and the fact that there are no fitting parameters whatsoever.

The amount by which the Stark effect shifts the interference minimum can be estimated using Eqs. (9) and (11). The interference minimum appears at the momentum $|\mathbf{k}|$ where the real part of the recombination matrix element is zero. For CO

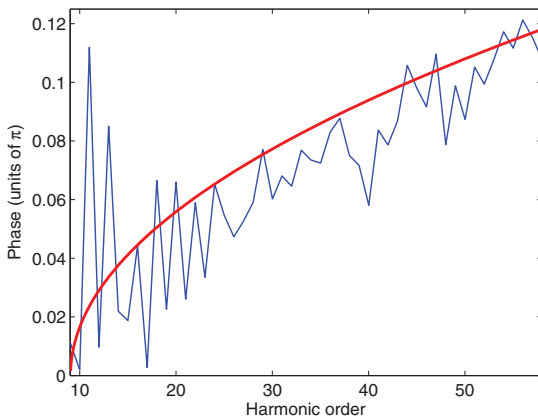


FIG. 6. (Color online) Estimates of the Stark phase accumulated in the continuum for CO oriented at $\theta = 82^\circ$, and using the pulse parameters from Sec. II. The smooth (red) curve is calculated from Eq. (11) based on classical trajectories to map ionization and recombination times to harmonic order. The irregular (blue) curve is the phase difference between harmonics calculated with and without including the Stark effect in the Lewenstein model. To avoid cancellation from neighboring half-cycles, ionization is artificially restricted to every other half-cycle (see text).

oriented at $\theta = 86^\circ$ in Fig. 4(b), this happens at $|\mathbf{k}| = 2.06$ a.u., corresponding to $\omega = 46.3\omega_0$. The accumulated phase from Eq. (11) is on the order of 0.05π , which is enough to shift the interference condition to $|\mathbf{k}| = 2.08$ a.u., corresponding to $\omega = 47.0\omega_0$. When θ is decreased, the phase shift increases due to the $\cos(\theta)$ scaling in Eq. (11).

Combining Eqs. (9) and (11) gives the two-center interference predictions plotted in Fig. 5. At perpendicular alignment the first-order Stark shift is exactly zero, and the minima coincide. The two-center model is seen to be off by two harmonic orders as compared with the Lewenstein calculations. As the alignment angle is decreased, the two-center interference model adequately describes the shift of the

minimum, down to about $\theta = 80^\circ$, after which the Lewenstein minimum washes out and finally vanishes.

The weakening of the interference minimum is not caused by interfering trajectories, as the long trajectories have been filtered out using a window function. A possible explanation is that the total recombination dipole velocity matrix element has a slower phase variation at smaller alignment angles, illustrated in Fig. 7(b) as a full (blue) curve for $\theta = 76^\circ$. One might have expected the phase variation to be faster, due to the larger contribution from the geometric phase $\mathbf{k} \cdot \mathbf{R}_n$, but the total phase is dominated by the behavior of the carbon matrix element, which has a slower π phase change at smaller alignment angles.

V. CONCLUSIONS AND DISCUSSION

We extend a model of two-center interference to include the superposition of opposite orientations in aligned polar molecules. Our analysis shows that two-center interference minima can be thought of either as an interference between recombination at different atoms or as an interference between opposite orientations. Using the former interpretation, we get the same estimate for the position of the minimum as for oriented molecules [6]. In this approximation the minimum only depends on the phase difference between recombination at different atoms. However, our calculations on CO show that the different recombination strengths are also important in determining the position of the minimum.

Interpreting the minimum as an interference between orientations, we predict the minimum position in aligned molecules in terms of the phase of the recombination dipole velocity matrix element of the *oriented* molecule. This model successfully predicts the minimum position in spectra calculated for aligned CO to within two harmonic orders for alignment angles ranging between 80° and 90° . At smaller alignment angles the observed minimum vanishes.

Interference minima from aligned homonuclear [29] and oriented heteronuclear [30] molecules have also been analyzed in terms of recombination into atomic orbitals of different parities. Such an approach explicitly accounts for the geometry of the molecular orbital, making it more reliable than previous models. Our model also includes the orbital structure, but within the framework of the Lewenstein model, thus showing how to extend previous models of two-center interference to polar molecules.

In the present study we focused on the effect of alignment vs orientation for polar molecules. We restricted our analysis to the spectrum from the HOMO channel. This is justified for CO when the internuclear axis is parallel to the laser polarization, as ionization from the HOMO-1 is strongly suppressed by a nodal plane, and the HOMO-2 is bound even more strongly [8,24]. However, ionization experiments indicate that the contribution from the HOMO-1 may become important at perpendicular alignment angles [31]. The HOMO-1 channel does not have a two-center interference minimum at the same location as the HOMO channel, because of different associated recombination strengths and phases. It is still an open question whether this would cause the minimum in the HOMO channel to be masked by the HOMO-1 contribution in experimentally measured harmonic spectra.

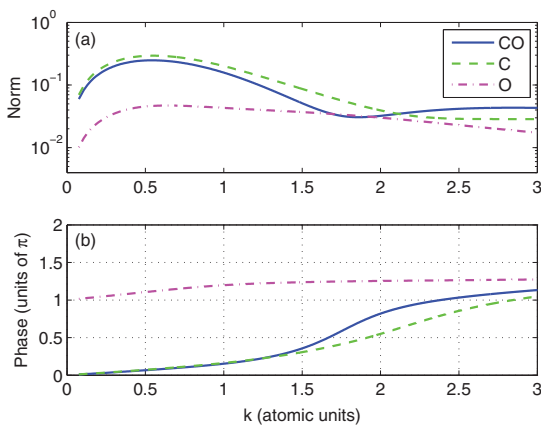


FIG. 7. (Color online) Same as Fig. 4, but with $\theta = 76^\circ$.

Inclusion of the Stark effect shifts the observed interference minimum *even though aligned molecules do not possess total permanent dipoles*. We explain this by the fact that the interference minimum is determined by the recombination phase of the *oriented* molecule, which does have a permanent dipole. This recombination phase is modified by the first-order Stark phase that the HOMO accumulates between the ionization and recombination step. Our model successfully reproduces the shift of the interference minimum due to the Stark effect.

ACKNOWLEDGMENTS

This work was supported by the Danish National Research Council (Grant No. 10-85430) and the National Science Foundation under Grant No. PHY-1019071.

APPENDIX

Here we derive Eqs. (4) and (5). The HOMO of the oriented molecule is denoted $|\psi, \theta\rangle$, and the corresponding wave function in the laboratory frame $\psi(\theta; \mathbf{r})$. Using the multi-center expansion in Eq. (3), the total recombination dipole velocity matrix element is

$$\langle \mathbf{k} | \hat{\mathbf{v}}_{\text{dip}} | \psi, \theta \rangle = \int \psi_{\mathbf{k}}^*(\mathbf{r}) \hat{\mathbf{v}}_{\text{dip}} \psi(\theta; \mathbf{r}) d\mathbf{r} \quad (\text{A1})$$

$$= \int \psi_{\mathbf{k}}^*(\mathbf{r}) \hat{\mathbf{v}}_{\text{dip}} \sum_n c_n \psi_n(\theta; \mathbf{r} - \mathbf{R}_n) d\mathbf{r} \quad (\text{A2})$$

$$= \sum_n c_n \int e^{i\mathbf{k}\cdot\mathbf{r}} \hat{\mathbf{v}}_{\text{dip}} \psi_n(\theta; \mathbf{r} - \mathbf{R}_n) d\mathbf{r} \quad (\text{A3})$$

$$= \sum_n c_n e^{i\mathbf{k}\cdot\mathbf{R}_n} \int e^{i\mathbf{k}\cdot\mathbf{r}} \hat{\mathbf{v}}_{\text{dip}} \psi_n(\theta; \mathbf{r}) d\mathbf{r} \quad (\text{A4})$$

$$= \sum_n c_n e^{i\mathbf{k}\cdot\mathbf{R}_n} \langle \mathbf{k} | \hat{\mathbf{v}}_{\text{dip}} | \psi_n, \theta \rangle \quad (\text{A5})$$

$$= \sum_n e^{i[\mathbf{k}\cdot\mathbf{R}_n + \phi_n(\mathbf{k}, \theta)]} |c_n \langle \mathbf{k} | \hat{\mathbf{v}}_{\text{dip}} | \psi_n, \theta \rangle|. \quad (\text{A6})$$

In the last step the intrinsic recombination phase $\phi_n(\mathbf{k}, \theta)$ of the matrix element $c_n \langle \mathbf{k} | \hat{\mathbf{v}}_{\text{dip}} | \psi_n, \theta \rangle$ is written out explicitly.

Equation (5) follows from the observation that the recombination dipole velocity matrix element is given by

$$\langle \mathbf{k} | \hat{\mathbf{v}}_{\text{dip}} | \psi, \theta \rangle = \mathbf{k} \tilde{\psi}(\theta; \mathbf{k}), \quad (\text{A7})$$

where $\tilde{\psi}(\theta; \mathbf{k})$ is the Fourier transform of the ground-state wave function. Flipping the orientation of the molecule is the same as adding π to θ . We now fix the coordinate system such that the laser polarization is along the x axis and the molecular axis confined to the xy plane. All molecular orbitals can then be chosen to be real, and either even or odd in z . Orbitals that are odd in z do not contribute to the total HHG spectrum [24], which leaves orbitals for which adding π to θ is the same as replacing the wave function with $\psi(\theta; -x, -y, z) = \psi(\theta; -x, -y, -z)$.

The recombination dipole velocity matrix element of a flipped molecule is then

$$\langle \mathbf{k} | \hat{\mathbf{v}}_{\text{dip}} | \psi, \theta + \pi \rangle = \mathbf{k} \tilde{\psi}(\theta + \pi; \mathbf{k}) \quad (\text{A8})$$

$$= \mathbf{k} \tilde{\psi}(\theta; -\mathbf{k}) \quad (\text{A9})$$

$$= \mathbf{k} \tilde{\psi}^*(\theta; \mathbf{k}) \quad (\text{A10})$$

$$= \langle \mathbf{k} | \hat{\mathbf{v}}_{\text{dip}} | \psi, \theta \rangle^*. \quad (\text{A11})$$

In the above we use the behavior of the Fourier transform under coordinate inversion as well as a property of Fourier transforms of real functions.

-
- [1] M. Lein, N. Hay, R. Velotta, J. P. Marangos, and P. L. Knight, *Phys. Rev. A* **66**, 023805 (2002).
- [2] M. Lein, N. Hay, R. Velotta, J. P. Marangos, and P. L. Knight, *Phys. Rev. Lett.* **88**, 183903 (2002).
- [3] J. L. Krause, K. J. Schafer, and K. C. Kulander, *Phys. Rev. Lett.* **68**, 3535 (1992).
- [4] P. B. Corkum, *Phys. Rev. Lett.* **71**, 1994 (1993).
- [5] M. Lewenstein, P. Balcou, M. Y. Ivanov, A. L'Huillier, and P. B. Corkum, *Phys. Rev. A* **49**, 2117 (1994).
- [6] X. Zhu, Q. Zhang, W. Hong, P. Lan, and P. Lu, *Opt. Express* **19**, 137866 (2011).
- [7] H. Stapelfeldt and T. Seideman, *Rev. Mod. Phys.* **75**, 543 (2003).
- [8] A. Etches and L. B. Madsen, *J. Phys. B* **43**, 155602 (2010).
- [9] L. Holmegaard *et al.*, *Nature Phys.* **6**, 428 (2010).
- [10] D. Dimitrovski, M. Abu-samha, L. B. Madsen, F. Filsinger, G. Meijer, J. Küpper, L. Holmegaard, L. Kalhøj, J. H. Nielsen, and H. Stapelfeldt, *Phys. Rev. A* **83**, 023405 (2011).
- [11] J. L. Hansen *et al.*, *Phys. Rev. A* **83**, 023406 (2011).
- [12] M. Lein, *J. Mod. Opt.* **58**, 1188 (2011).
- [13] D. Dimitrovski, C. P. J. Martiny, and L. B. Madsen, *Phys. Rev. A* **82**, 053404 (2010).
- [14] M. Abu-samha and L. B. Madsen, *Phys. Rev. A* **82**, 043413 (2010).
- [15] O. Smirnova, S. Patchkovskii, Y. Mairesse, N. Dudovich, D. Villeneuve, P. Corkum, and M. Y. Ivanov, *Phys. Rev. Lett.* **102**, 063601 (2009).
- [16] O. Smirnova, Y. Mairesse, S. Patchkovskii, N. Dudovich, D. Villeneuve, P. Corkum, and M. Ivanov, *Nature* **460**, 972 (2009).
- [17] H. J. Wörner, J. B. Bertrand, P. Hockett, P. B. Corkum, and D. M. Villeneuve, *Phys. Rev. Lett.* **104**, 233904 (2010).
- [18] C. Figueira de Morisson Faria and B. B. Augstein, *Phys. Rev. A* **81**, 043409 (2010).
- [19] Y.-C. Han and L. B. Madsen, *J. Phys. B* **43**, 225601 (2010).
- [20] M. Schmidt *et al.*, *J. Comput. Chem.* **14**, 1347 (1993).
- [21] J. C. Baggese and L. B. Madsen, *J. Phys. B* **44**, 115601 (2011).
- [22] O. E. Alon, V. Averbukh, and N. Moiseyev, *Phys. Rev. Lett.* **80**, 3743 (1998).
- [23] G. L. Kamta and A. D. Bandrauk, *Phys. Rev. A* **70**, 011404 (2004).
- [24] C. B. Madsen and L. B. Madsen, *Phys. Rev. A* **76**, 043419 (2007).

- [25] C. B. Madsen, A. S. Mouritzen, T. K. Kjeldsen, and L. B. Madsen, *Phys. Rev. A* **76**, 035401 (2007).
- [26] C. C. Chirilă and M. Lein, *Phys. Rev. A* **73**, 023410 (2006).
- [27] C. F. de Morisson Faria, *Phys. Rev. A* **76**, 043407 (2007).
- [28] A. Etches, C. B. Madsen, and L. B. Madsen, *Phys. Rev. A* **81**, 013409 (2010).
- [29] S. Odžak and D. B. Milošević, *Phys. Rev. A* **79**, 023414 (2009).
- [30] B. B. Augstein and C. F. de Morisson Faria, *J. Phys. B* **44**, 055601 (2011).
- [31] P. von den Hoff, I. Znakovskaya, S. Zherebtsov, M. F. Kling, and R. de Vivie-Riedle, *Appl. Phys. B* **98**, 659 (2010).



Laser-induced bound-state phases in high-order harmonic generation

Adam Etches, Mette B. Gaarde, and Lars Bojer Madsen

arXiv:1206.2104v1

Laser-induced bound-state phases in high-order harmonic generation

Adam Etches,¹ Mette B. Gaarde,² and Lars Bojer Madsen¹

¹*Lundbeck Foundation Theoretical Center for Quantum System Research,*

Department of Physics and Astronomy, Aarhus University, 8000 Aarhus C, Denmark

²*Department of Physics and Astronomy, Louisiana State University, Baton Rouge, Louisiana 70803-4001, USA*

(Dated: June 12, 2012)

We present single-molecule and macroscopic calculations showing that laser-induced Stark shifts contribute significantly to the phase of high-order harmonics from polar molecules. This is important for orbital tomography, where phases of field-free dipole matrix elements are needed in order to reconstruct molecular orbitals. We derive an analytical expression that allows the first-order Stark phase to be subtracted from experimental measurements.

PACS numbers: 42.65.Ky, 42.65.Re

It is a long-standing goal of atomic and molecular physics to follow electronic processes on their natural length and time scales, and eventually even to control their dynamics. Advances towards orbital tomography, the experimental reconstruction of an electronic wave function, have been made using high-order harmonic generation (HHG) [1–3]. In HHG based tomography, a continuum electron wave packet is formed at the peak of each half-cycle of an infrared driving laser. The continuum wave packet is accelerated in the oscillating laser field, and brought back to the vicinity of the bound-state wave packet at a later time. A high-energy photon is emitted when the continuum electron recombines into the ground state after having picked up kinetic energy in the laser field [4, 5]. The recombination step encodes information about the ground state onto the emitted harmonics through the recombination dipole matrix elements.

In order to reconstruct the ground state orbital, one needs both the magnitudes and the phases of the recombination matrix elements. It is challenging to extract these phases from HHG spectra, as phases not related to the recombination step have to be subtracted from the harmonic phases. Phases related to the formation of a continuum wave packet and its subsequent acceleration in the laser field have already been accounted for, allowing the reconstruction of symmetric orbitals in N₂ and CO₂ [2, 3]. Nonsymmetric orbitals, however, pose a problem for orbital tomography due to their permanent dipoles, which cause them to acquire an additional laser-induced bound-state Stark phase. Using CO as a representative polar molecule, we find that the first-order Stark phase grows from zero to 0.5 π within the harmonic plateau. The aim of this work is to extend the tomographic method by accounting for this Stark phase, and presenting an analytical expression with which to subtract it from measurements.

To isolate the effect of Stark phases we consider the idealized [6–10] case of perfectly 3D oriented molecules. In the simplest model, the electric field $\mathbf{F}(t)$ of the driving pulse only influences the highest occupied molecular orbital (HOMO) by adiabatically Stark-shifting its orbital

energy E (atomic units are used throughout):

$$E(\mathbf{F}(t)) = E_0 - \boldsymbol{\mu} \cdot \mathbf{F}(t) - \frac{1}{2} \mathbf{F}^T(t) \underline{\underline{\alpha}} \mathbf{F}(t). \quad (1)$$

As an example, we take CO oriented parallel to the polarization axis of the driving laser. The HOMO has σ symmetry, and an ionization potential of $I_p = |E_0| = 0.5150$ au. Its permanent dipole $|\boldsymbol{\mu}| = 1.1$ au points from the carbon towards the oxygen nucleus. The components of the polarizability tensor $\underline{\underline{\alpha}}$ are $\alpha_{\parallel} = 3.2$ au, and $\alpha_{\perp} = 2.8$ au [11]. The resulting Stark shift caused by a moderately intense laser is sketched in Fig. 1. The chosen geometry suppresses contributions from the HOMO–1 due to its π symmetry [12].

As the bound state evolves in time from t' to t , it accumulates the phase $\int_{t'}^t E(\mathbf{F}(t'')) dt''$. According to Eq. (1) the accumulated phase differs from the field-free time-evolution by a Stark phase

$$\Phi_{\text{Stark}}(t, t') = \Phi_{\text{Stark}}^{(1)}(t, t') + \Phi_{\text{Stark}}^{(2)}(t, t'), \quad (2)$$

where the first- and second-order Stark phases read

$$\Phi_{\text{Stark}}^{(1)}(t, t') = - \int_{t'}^t \boldsymbol{\mu} \cdot \mathbf{F}(t'') dt'' \quad (3)$$

$$\Phi_{\text{Stark}}^{(2)}(t, t') = - \frac{1}{2} \int_{t'}^t \mathbf{F}^T(t'') \underline{\underline{\alpha}} \mathbf{F}(t'') dt''. \quad (4)$$

The Stark phase changes the interference between the bound state, and the continuum wave packet that is born at time t' , and returns at time t .

Equations (2)–(4) are formulated in the time-domain, while orbital tomography is performed in the frequency domain. We therefore calculate classical electron trajectories, and translate the kinetic energy into photon energy using energy conservation for those continuum electrons that recombine at the origin:

$$\omega(t, t') = \frac{1}{2} \dot{\mathbf{r}}^2(t, t') + I_p(\mathbf{F}(t)). \quad (5)$$

Here $\dot{\mathbf{r}}(t, t')$ is the velocity at time t of an electron that is detached at the origin with zero velocity at time t' , and

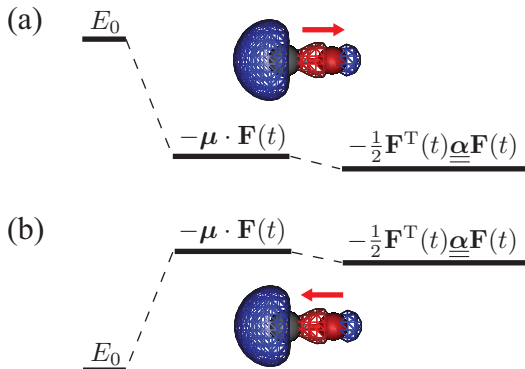


FIG. 1: (Color online) Sketch of the Stark shift felt by the HOMO of CO when subject to an electric field. The relative size of the first- and second-order Stark shift is drawn to scale for an electric field $F_0 = 0.075$ au, corresponding to a laser intensity of 2×10^{14} W/cm². (a) The electric field is parallel to the permanent dipole of the orbital, and the effective ionization potential is raised. (b) The electric field is antiparallel to the permanent dipole, and the effective ionization potential is lowered.

$I_p(\mathbf{F}(t)) = |E(\mathbf{F}(t))|$. The effect of the ionic potential on the continuum trajectories is ignored. The result of a classical trajectory calculation is shown in Fig. 2 for an ultrashort pulse. The electric field is assumed to have a cosine squared envelope, and an 800 nm sine carrier wave. The full width at half maximum is 0.72 times one optical cycle T , corresponding to a full duration of $2T$. The maximum of the electric field is $F_0 = 0.071$ au, corresponding to a peak intensity of 2.0×10^{14} W/cm² of the envelope. Only one half-cycle contributes to the harmonic emission, which ensures that the continuum electron only recollides from one direction. Controlling the recollision direction is essential for tomography of nonsymmetric states [13]. Together, Eq. (5) and the calculation leading to Fig. 2 provide the required map between (t, t') and harmonic frequency.

Returning to the Stark phases, Eq. (3) can be interpreted in terms of the integral of the force felt by the continuum electron, showing that the first-order Stark phase is directly proportional to the return velocity

$$\Phi_{\text{Stark}}^{(1)}(t, t') = \boldsymbol{\mu} \cdot \dot{\mathbf{r}}(t, t'). \quad (6)$$

With orbital tomography in mind, one might be interested in minimizing the Stark phase. However, Eq. (6) reveals that the first-order Stark phase cannot be minimized by varying the driving pulse, as it only depends

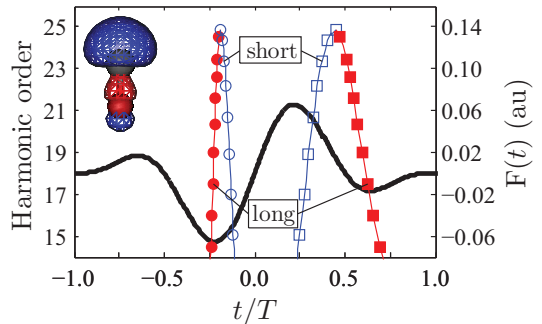


FIG. 2: (Color online) Classical trajectories for CO subject to an ultrashort laser pulse, indicated by the solid black curve. Instants of ionization are marked by circles, and instants of recombination by squares. The vertical offset of a trajectory, consisting of a circle and a square, indicates the photon energy of the emitted harmonic, calculated using Eq. (5). Open (blue) markers indicate short trajectories, and full (red) markers indicate long trajectories.

on the return velocity, and the angle θ between the internuclear axis and the laser polarization axis. Insertion into Eq. (5) gives

$$\Phi_{\text{Stark}}^{(1)}(t, t') = \text{sgn}(\boldsymbol{\mu} \cdot \dot{\mathbf{r}}(t, t')) \mu |\cos(\theta)| \times \sqrt{2(\omega(t, t') - I_p(\mathbf{F}(t)))}, \quad (7)$$

where $\text{sgn}(\boldsymbol{\mu} \cdot \dot{\mathbf{r}}(t, t'))$ keeps track of the direction with which the returning electron probes the bound state. The time-dependence of the Stark-shifted ionization potential introduces a small difference between short and long trajectories. If the field-dependence of the ionization potential is ignored, then Eq. (7) simplifies to

$$\Phi_{\text{Stark}}^{(1)}(\omega) \approx \pm \mu \cos(\theta) \sqrt{2(\omega - I_p)}. \quad (8)$$

The advantage of Eq. (8) is that it gives an analytical prediction of the first-order Stark phase directly in terms of the harmonic frequency, ω , rather than in terms of electron trajectories through $\omega(t, t')$. We return to a discussion of the accuracy of this result below.

The second-order Stark phase cannot be expressed as simply in terms of the harmonic frequency. This is because Eq. (4) turns out to depend explicitly on the driving pulse, as well as giving qualitatively different result for short and long trajectories. The scaling of the second-order Stark phase with respect to laser parameters can be estimated by neglecting the pulse envelope, and integrating Eq. (4) from the peak of a half-cycle $t' = t_{\text{peak}}$ up to $t = t_{\text{peak}} + 2T/3$. The cut-off harmonics are then found to accumulate a second-order Stark phase proportional to $F_0^2/\omega_0 = 4\omega_0 U_p$, where ω_0 is the frequency of

the driving laser, and U_p the ponderomotive potential. According to the usual cutoff rule, $\omega_{\max} = 3.17U_p + I_p$, the importance of the second-order Stark phase can be reduced by increasing the wave length of the driving laser while keeping the harmonic cutoff fixed.

We use the Lewenstein model [14] to test the validity of the trajectory calculations. The first-order Stark phase is extracted by subtracting harmonic phases calculated with and without inclusion of the first-order Stark shift in the Lewenstein model [11, 15]. Figure 3(a) shows that short trajectories account for the first-order Stark phase within the limits set by the classical model, which does not account for harmonics below the ionization threshold, nor beyond the harmonic cutoff. The phase spikes coincide with minima in the harmonic plateau. The minima are caused by the interference between short and long trajectories, and each is associated with a sharp variation in the harmonic phase. The exact position of each minimum changes when the Stark shift is included, which explains the phase spikes.

The analytical model of Eq. (8) slightly overestimates the first-order Stark phase due to the use of the field-free ionization potential. The error is therefore expected to increase with increasing intensity. Comparing Eq. (8) to Lewenstein calculations at the 21st harmonic for three different intensities we observe an error of 8% (1.5×10^{14} W/cm²), 10% (2.0×10^{14} W/cm²), and 12% (2.5×10^{14} W/cm²). The interference features also move with intensity, but the square root behavior is the same at all three intensities. The close agreement between Eq. (8) and the long trajectory calculation is due to the extremely narrow pulse envelope, which causes the long trajectories to recombine at low field strengths as shown in Fig. 2.

The second-order Stark phase is plotted in Fig. 3(b). The Lewenstein result is obtained by including the first and second-order Stark shifts in the Lewenstein model, calculating the harmonic phases, and then subtracting the phase obtained when only the first-order Stark shift is included. The calculation agrees qualitatively with the short trajectory prediction. The trajectory calculation shows that the second-order Stark phase increases in magnitude when the electron spends longer time in the continuum. Selecting the short-trajectory contribution is thus an additional way of reducing the importance of second-order Stark phases.

We would like to stress the point that the simple behavior of the Stark phase is due to the fact that only one half-cycle, and mostly the short trajectories, contributes to the high-order harmonics. When several sets of trajectories contribute, the total phase is the result of a coherent sum of harmonic amplitudes, which can cause large modulations on top of the trend in Fig. 3. Experimentally, the dominating trajectory is selected through phase-matching by adjusting the position of the laser focus relative to the nonlinear medium [16].

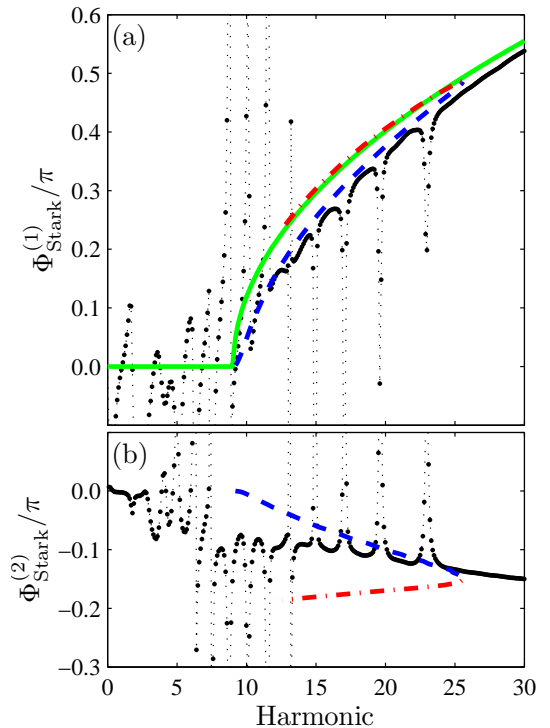


FIG. 3: (Color online) (a) Accumulated first-order Stark phase of CO subject to an ultrashort laser pulse (parameters are given in the text). The connected black dots indicate the phase obtained from a quantum calculation. The dashed (blue) curve is the phase predicted from short classical trajectories, and the dash-dotted (red) curve the phase from long trajectories. The smooth (green) curve is the analytical model of Eq. (8), with the phase defined to be zero for harmonics below I_p . (b) Accumulated second-order Stark phase. Dashed and dash-dotted curves indicate short and long classical trajectories.

In order to uncover the interplay between Stark phases and phase-matching, we now present results of the coupled solutions of the Maxwell wave equation (MWE) and the time-dependent Schrödinger equation (TDSE). We solve the MWE in the slowly evolving wave approximation as described in [16], and at each plane in the propagation direction we solve the TDSE in the Lewenstein model to calculate the time-dependent dipole moment [11]. The nonlinear medium is a 5 mm jet of CO molecules. The CO molecules are assumed to be perfectly oriented as in Fig. 2. The gas density is set to 5×10^{14} cm⁻³. We use the same driving pulse as above, except for adding a Gaussian focus with confocal parameter $b = 2.0$ cm. The focus is placed 0.70 cm in front of the

middle of the jet. The peak intensity is 3.0×10^{14} W/cm², chosen so as to give a peak intensity of 2.0×10^{14} W/cm² in the middle of the medium. Our results are insensitive to ionization due to the very low target density.

The Stark phase is calculated by propagating the MWE twice, with and without including the first- and second-order Stark effect in the single-molecule Lewenstein calculations. In each case we transform to the far field, apply a spatial filter that selects predominantly the central, short trajectory contribution to the harmonics, and transform back to the near field. In an experiment this would correspond to having an aperture or a refocusing mirror in the far field. Then we subtract the phases obtained with and without including Stark shifts. An average over the final spot on the detector screen is made by weighting the Stark phase $\Phi_{\text{Stark}}(\omega, r)$ at a given radius with the strength of the harmonic $|F_{\text{HHG}}(\omega, r)|^2$:

$$\langle \Phi_{\text{Stark}}(\omega) \rangle_r = \frac{\int_0^\infty \Phi_{\text{Stark}}(\omega, r) |F_{\text{HHG}}(\omega, r)|^2 r dr}{\int_0^\infty |F_{\text{HHG}}(\omega, r)|^2 r dr}. \quad (9)$$

The result, shown in Fig. 4(a), compares qualitatively with single-molecule predictions based on classical trajectories calculated for a peak intensity of 2.0×10^{14} W/cm². The phase oscillations stem from the intensity dependence of minima caused by interference between short and long trajectories. At a fixed intensity the minima are very sharp, giving rise to sharp variations in the extracted Stark phase as in Fig. 3. In macroscopic calculations the intensity falls off along, and perpendicular to, the propagation axis of the driving laser, causing the minima to smear out. The Lewenstein model has been known to overestimate the importance of the long trajectories [17], leading to an exaggeration of these interference oscillations in our calculations.

We also present results for perfectly aligned CO molecules. Spectra are calculated with and without the Stark effect by solving the MWE separately for opposite orientations, and adding the resulting harmonics coherently at the end of the gas [18]. This procedure is valid in the limit where ionization-induced reshaping of the driving pulse is negligible. The harmonics are then propagated to the far field, filtered, refocused, and the Stark phase extracted. Equation (9) is used to calculate the radially averaged Stark phase shown in Fig. 4(b). If the first-order Stark phase from opposite orientations had canceled out, then the total Stark phase would have been similar to that in Fig. 3(b). Instead, the total Stark phase is similar to that of fully oriented CO molecules in Fig. 4(a). The reason for this is that the Lewenstein model favors ionization when the electric field points from carbon to oxygen [11]. The ultrashort pulse only allows one half-cycle to contribute, thus increasing the relative contribution from the orientation shown in Fig. 2. The nonvanishing first-order Stark phase in Fig. 4 underlines that polar molecules behave differently from nonpolar molecules,

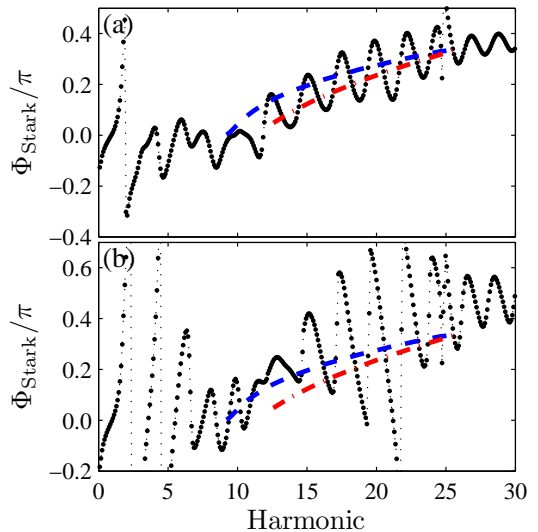


FIG. 4: (Color online) Stark phases from a gas jet of CO molecules (parameters are given in the text). (a) The CO molecules are oriented as in Fig. 2. The connected black dots are phases obtained from a full simulation including macroscopic propagation. The dashed (blue) curve is the single-molecule phase predicted from short classical trajectories, and the dash-dotted (red) curve the phase from long trajectories. (b) The CO molecules are aligned parallel to the laser polarization. The black dots include both orientations of the target molecules. Dashed and dash-dotted curves indicate short and long classical trajectories.

even if their head-to-tail symmetry is unbroken.

In conclusion, we have investigated the role of laser-induced bound-state phases in HHG. We show that first- and second-order Stark shifts may both contribute significantly to the phase of harmonics generated from polar molecules. Such Stark phases must be accounted for if HHG is to be used for orbital tomography. We find a simple analytical expression for the first-order Stark phase, showing it to scale as the square root of harmonic frequency. No simple expression is found for the second-order Stark phase, but it can be minimized by increasing the laser wave length while keeping the ponderomotive potential fixed. Propagation of the Maxwell wave equation confirms that Stark phases survive phase-matching in the target gas.

This work was supported by the Danish National Research Council (Grant No. 10-85430), the National Science Foundation under Grant No. PHY-1019071, and an ERC-StG (Project NO. 277767 -TDMET). High-performance computational resources were provided by the Louisiana Optical Network Initiative, www.loni.org. We would like to thank Hans-Jakob Wörner for advice

regarding experimental parameters.

-
- [1] J. Itatani, J. Levesque, D. Zeidler, H. Niikura, H. Pepin, J. Kieffer, P. Corkum, and D. Villeneuve, *Nature* **432**, 867 (2004).
- [2] S. Haessler, J. Caillat, W. Boutu, C. Giovanetti-Teixeira, T. Ruchon, T. Auguste, Z. Diveki, P. Breger, A. Maquet, B. Carré, et al., *Nature Physics* **6**, 200 (2010).
- [3] C. Vozzi, M. Negro, F. Calegari, G. Sansone, M. Nisoli, S. De Silvestri, and S. Stagira, *Nature Physics* **7**, 822 (2011).
- [4] J. L. Krause, K. J. Schafer, and K. C. Kulander, *Phys. Rev. Lett.* **68**, 3535 (1992).
- [5] P. B. Corkum, *Phys. Rev. Lett.* **71**, 1994 (1993).
- [6] H. Stapelfeldt and T. Seideman, *Rev. Mod. Phys.* **75**, 543 (2003).
- [7] L. Holmegaard, J. H. Nielsen, I. Nevo, H. Stapelfeldt, F. Filsinger, J. Küpper, and G. Meijer, *Phys. Rev. Lett.* **102**, 023001 (2009).
- [8] F. Filsinger, J. Küpper, G. Meijer, L. Holmegaard, J. H. Nielsen, I. Nevo, J. L. Hansen, and H. Stapelfeldt, *J. Chem. Phys.* **131**, 064309 (2009).
- [9] O. Ghafur, A. Rouzee, A. Gijbbersen, W. K. Siu, S. Stolte, and M. J. J. Vrakking, *Nature Physics* **5**, 289 (2009).
- [10] S. De, I. Znakovskaya, D. Ray, F. Anis, N. G. Johnson, I. A. Bocharova, M. Magrakvelidze, B. D. Esry, C. L. Cocke, I. V. Litvinyuk, et al., *Phys. Rev. Lett.* **103**, 153002 (2009).
- [11] A. Etches and L. B. Madsen, *J. Phys. B.* **43**, 155602 (2010).
- [12] C. B. Madsen and L. B. Madsen, *Phys. Rev. A* **76**, 043419 (2007).
- [13] E. V. van der Zwan, C. C. Chirilă, and M. Lein, *Phys. Rev. A* **78**, 033410 (2008).
- [14] M. Lewenstein, P. Balcou, M. Y. Ivanov, A. L’Huillier, and P. B. Corkum, *Phys. Rev. A* **49**, 2117 (1994).
- [15] A. Etches, M. B. Gaarde, and L. B. Madsen, *Phys. Rev. A* **84**, 023418 (2011).
- [16] M. B. Gaarde, J. L. Tate, and K. J. Schafer, *J. Phys. B* **41**, 132001 (2008).
- [17] M. B. Gaarde and K. J. Schafer, *Phys. Rev. A* **65**, 031406 (2002).
- [18] C. B. Madsen, A. S. Mouritzen, T. K. Kjeldsen, and L. B. Madsen, *Phys. Rev. A* **76**, 035401 (2007).



Bibliography

- [1] X. F. Li, A. L'Huillier, M. Ferray, L. A. Lompré, and G. Mainfray, "Multiple-harmonic generation in rare gases at high laser intensity," *Phys. Rev. A* 39, 5751 (1989).
- [2] M. Ferray, A. L'Huillier, X. F. Li, L. A. Lompre, G. Mainfray, and C. Manus, "Multiple-harmonic conversion of 1064 nm radiation in rare gases," *Journal of Physics B: Atomic, Molecular and Optical Physics* 21, L31 (1988).
- [3] E. A. Gibson, A. Paul, N. Wagner, R. Tobey, D. Gaudiosi, S. Backus, I. P. Christov, A. Aquila, E. M. Gullikson, D. T. Attwood, M. M. Murnane, and H. C. Kapteyn, "Coherent Soft X-ray Generation in the Water Window with Quasi-Phase Matching," *Science* 302, 95 (2003).
- [4] E. J. Takahashi, T. Kanai, K. L. Ishikawa, Y. Nabekawa, and K. Midorikawa, "Coherent Water Window X Ray by Phase-Matched High-Order Harmonic Generation in Neutral Media," *Phys. Rev. Lett.* 101, 253901 (2008).

Bibliography

- [5] T. Popmintchev, M.-C. Chen, D. Popmintchev, P. Arpin, S. Brown, S. Ališauskas, G. Andriukaitis, T. Balčiunas, O. D. Mücke, A. Pugzlys, A. Baltuška, B. Shim, S. E. Schrauth, A. Gaeta, C. Hernández-García, L. Plaja, A. Becker, A. Jaron-Becker, M. M. Murnane, and H. C. Kapteyn, “Bright Coherent Ultrahigh Harmonics in the keV X-ray Regime from Mid-Infrared Femtosecond Lasers,” *Science* 336, 1287 (2012).
- [6] P. Antoine, A. L’Huillier, and M. Lewenstein, “Attosecond Pulse Trains Using High-Order Harmonics,” *Phys. Rev. Lett.* 77, 1234 (1996).
- [7] G. Sansone, E. Benedetti, F. Calegari, C. Vozzi, L. Avaldi, R. Flammini, L. Poletto, P. Villoresi, C. Altucci, R. Velotta, S. Stagira, S. De Silvestri, and M. Nisoli, “Isolated Single-Cycle Attosecond Pulses,” *Science* 314, 443 (2006).
- [8] E. Goulielmakis, M. Schultze, M. Hofstetter, V. S. Yakovlev, J. Gagnon, M. Uiberacker, A. L. Aquila, E. M. Gullikson, D. T. Attwood, R. Kienberger, F. Krausz, and U. Kleineberg, “Single-Cycle Nonlinear Optics,” *Science* 320, 1614 (2008).
- [9] F. Krausz and M. Ivanov, “Attosecond physics,” *Rev. Mod. Phys.* 81, 163 (2009).
- [10] P. Zeitoun *et al.*, “A high-intensity highly coherent soft X-ray femtosecond laser seeded by a high harmonic beam,” *Nature* 431, 426 (2004).
- [11] G. Lambert *et al.*, “Injection of harmonics generated in gas in a free-electron laser providing intense and coherent extreme-ultraviolet light,” *Nature Physics* 4, 296 (2008).
- [12] S. Haessler, J. Caillat, and P. Salières, “Self-probing of molecules with high harmonic generation,” *Journal of Physics B: Atomic, Molecular and Optical Physics* 44, 203001 (2011).

Bibliography

- [13] P. H. Bucksbaum, “The Future of Attosecond Spectroscopy,” *Science* 317, 766 (2007).
- [14] M. Lein, “Molecular imaging using recolliding electrons,” *Journal of Physics B: Atomic, Molecular and Optical Physics* 40, R135 (2007).
- [15] P. B. Corkum, “Plasma perspective on strong field multiphoton ionization,” *Phys. Rev. Lett.* 71, 1994 (1993).
- [16] J. L. Krause, K. J. Schafer, and K. C. Kulander, “High-order harmonic generation from atoms and ions in the high intensity regime,” *Phys. Rev. Lett.* 68, 3535 (1992).
- [17] M. Lewenstein, P. Balcou, M. Y. Ivanov, A. L’Huillier, and P. B. Corkum, “Theory of high-harmonic generation by low-frequency laser fields,” *Phys. Rev. A* 49, 2117 (1994).
- [18] M. B. Gaarde, J. L. Tate, and K. J. Schafer, “Macroscopic aspects of attosecond pulse generation,” *Journal of Physics B: Atomic, Molecular and Optical Physics* 41, 132001 (2008).
- [19] E. Lorin, S. Chelkowski, and A. D. Bandrauk, “Attosecond pulse generation from aligned molecules—dynamics and propagation in H_2^+ ,” *New Journal of Physics* 10, 025033 (2008).
- [20] J. C. Baggesen and L. B. Madsen, “On the dipole, velocity and acceleration forms in high-order harmonic generation from a single atom or molecule,” *Journal of Physics B: Atomic, Molecular and Optical Physics* 44, 115601 (2011).
- [21] C. B. Madsen and L. B. Madsen, “Theoretical studies of high-order harmonic generation: Effects of symmetry, degeneracy, and orientation,” *Phys. Rev. A* 76, 043419 (2007).
- [22] M. W. Schmidt, K. K. Baldrige, J. A. Boatz, S. T. Elbert, M. S. Gordon, J. H. Jensen, S. Koseki, N. Matsunaga, K. A.

Bibliography

- Nguyen, S. Su, T. L. Windus, M. Dupuis, and J. A. Montgomery, "General atomic and molecular electronic structure system," *Journal of Computational Chemistry* 14, 1347 (1993).
- [23] B. K. McFarland, J. P. Farrell, P. H. Bucksbaum, and M. Gühr, "High Harmonic Generation from Multiple Orbitals in N₂," *Science* 322, 1232 (2008).
- [24] Z. Diveki, A. Camper, S. Haessler, T. Auguste, T. Ruchon, B. Carré, P. Salières, R. Guichard, J. Caillat, A. Maquet, and R. Taïeb, "Spectrally resolved multi-channel contributions to the harmonic emission in N₂," *New Journal of Physics* 14, 023062 (2012).
- [25] O. Smirnova, Y. Mairesse, S. Patchkovskii, N. Dudovich, D. Villeneuve, P. Corkum, and M. Ivanov, "High harmonic interferometry of multi-electron dynamics in molecules," *Nature* 460, 972 (2009).
- [26] E. P. Fowe and A. D. Bandrauk, "Nonlinear time-dependent density-functional-theory study of ionization and harmonic generation in CO₂ by ultrashort intense laser pulses: Orientational effects," *Phys. Rev. A* 81, 023411 (2010).
- [27] C. Vozzi, F. Calegari, E. Benedetti, J.-P. Caumes, G. Sansone, S. Stagira, M. Nisoli, R. Torres, E. Heesel, N. Kajumba, J. P. Marangos, C. Altucci, and R. Velotta, "Controlling Two-Center Interference in Molecular High Harmonic Generation," *Phys. Rev. Lett.* 95, 153902 (2005).
- [28] T. Kanai, S. Minemoto, and H. Sakai, "Quantum interference during high-order harmonic generation from aligned molecules," *Nature* 435, 470 (2005).
- [29] X. Zhou, R. Lock, W. Li, N. Wagner, M. M. Murnane, and H. C. Kaptelyn, "Molecular Recollision Interferometry in High Harmonic Generation," *Phys. Rev. Lett.* 100, 073902 (2008).

Bibliography

- [30] K. Kato, S. Minemoto, and H. Sakai, "Suppression of high-order-harmonic intensities observed in aligned CO₂ molecules with 1300-nm and 800-nm pulses," *Phys. Rev. A* 84, 021403 (2011).
- [31] Y.-C. Han and L. B. Madsen, "Minimum in the high-order harmonic generation spectrum from molecules: role of excited states," *Journal of Physics B: Atomic, Molecular and Optical Physics* 43, 225601 (2010).
- [32] M. Ammosov, N. Delone, and V. Krainov, "Tunnel ionization of complex atoms and of atomic ions in an alternating electromagnetic field," *Sov Phys JETP* 64, 1191 (1986).
- [33] C. B. Madsen and L. B. Madsen, "High-order harmonic generation from arbitrarily oriented diatomic molecules including nuclear motion and field-free alignment," *Phys. Rev. A* 74, 023403 (2006).
- [34] C. B. Madsen, A. S. Mouritzen, T. K. Kjeldsen, and L. B. Madsen, "Effects of orientation and alignment in high-order harmonic generation and above-threshold ionization," *Phys. Rev. A* 76, 035401 (2007).
- [35] M. Lein, "Attosecond Probing of Vibrational Dynamics with High-Harmonic Generation," *Phys. Rev. Lett.* 94, 053004 (2005).
- [36] S. Patchkovskii, "Nuclear Dynamics in Polyatomic Molecules and High-Order Harmonic Generation," *Phys. Rev. Lett.* 102, 253602 (2009).
- [37] S. Baker, J. S. Robinson, C. A. Haworth, H. Teng, R. A. Smith, C. C. Chirilă, M. Lein, J. W. G. Tisch, and J. P. Marangos, "Probing Proton Dynamics in Molecules on an Attosecond Time Scale," *Science* 312, 424 (2006).
- [38] S. Baker, J. S. Robinson, M. Lein, C. C. Chirilă, R. Torres, H. C. Bandulet, D. Comtois, J. C. Kieffer, D. M. Villeneuve,

Bibliography

- J. W. G. Tisch, and J. P. Marangos, “Dynamic Two-Center Interference in High-Order Harmonic Generation from Molecules with Attosecond Nuclear Motion,” *Phys. Rev. Lett.* 101, 053901 (2008).
- [39] H. Stapelfeldt and T. Seideman, “*Colloquium*: Aligning molecules with strong laser pulses,” *Rev. Mod. Phys.* 75, 543 (2003).
- [40] L. Holmegaard, J. H. Nielsen, I. Nevo, H. Stapelfeldt, F. Filsinger, J. Küpper, and G. Meijer, “Laser-Induced Alignment and Orientation of Quantum-State-Selected Large Molecules,” *Phys. Rev. Lett.* 102, 023001 (2009).
- [41] L. Holmegaard *et al.*, “Photoelectron angular distributions from strong-field ionization of oriented molecules,” *Nature Physics* 6, 428 (2010).
- [42] J. L. Hansen, L. Holmegaard, J. H. Nielsen, H. Stapelfeldt, D. Dimitrovski, and L. B. Madsen, “Orientation-dependent ionization yields from strong-field ionization of fixed-in-space linear and asymmetric top molecules,” *Journal of Physics B: Atomic, Molecular and Optical Physics* 45, 015101 (2012).
- [43] J. L. Hansen, L. Holmegaard, L. Kalthøj, S. L. Kragh, H. Stapelfeldt, F. Filsinger, G. Meijer, J. Küpper, D. Dimitrovski, M. Abu-samha, C. P. J. Martiny, and L. B. Madsen, “Ionization of one- and three-dimensionally-oriented asymmetric-top molecules by intense circularly polarized femtosecond laser pulses,” *Phys. Rev. A* 83, 023406 (2011).
- [44] D. Dimitrovski, M. Abu-samha, L. B. Madsen, F. Filsinger, G. Meijer, J. Küpper, L. Holmegaard, L. Kalthøj, J. H. Nielsen, and H. Stapelfeldt, “Ionization of oriented carbonyl sulfide molecules by intense circularly polarized laser pulses,” *Phys. Rev. A* 83, 023405 (2011).

Bibliography

- [45] S. De, I. Znakovskaya, D. Ray, F. Anis, N. G. Johnson, I. A. Bocharova, M. Magrakvelidze, B. D. Esry, C. L. Cocke, I. V. Litvinyuk, and M. F. Kling, "Field-Free Orientation of CO Molecules by Femtosecond Two-Color Laser Fields," *Phys. Rev. Lett.* 103, 153002 (2009).
- [46] J. Ullrich, R. Moshhammer, A. Dorn, R. Dörner, L. P. H. Schmidt, and H. Schmidt-Böcking, "Recoil-ion and electron momentum spectroscopy: reaction-microscopes," *Reports on Progress in Physics* 66, 1463 (2003).
- [47] S. Ramakrishna and T. Seideman, "Information Content of High Harmonics Generated from Aligned Molecules," *Phys. Rev. Lett.* 99, 113901 (2007).
- [48] S. Ramakrishna and T. Seideman, "High-order harmonic generation as a probe of rotational dynamics," *Phys. Rev. A* 77, 053411 (2008).
- [49] S. Ramakrishna, P. A. J. Sherratt, A. D. Dutoi, and T. Seideman, "Origin and implication of ellipticity in high-order harmonic generation from aligned molecules," *Phys. Rev. A* 81, 021802 (2010).
- [50] P. A. J. Sherratt, S. Ramakrishna, and T. Seideman, "Signatures of the molecular potential in the ellipticity of high-order harmonics from aligned molecules," *Phys. Rev. A* 83, 053425 (2011).
- [51] C. C. Chirilă and M. Lein, "Strong-field approximation for harmonic generation in diatomic molecules," *Phys. Rev. A* 73, 023410 (2006).
- [52] P. Salières, B. Carré, L. Le Déroff, F. Grasbon, G. G. Paulus, H. Walther, R. Kopold, W. Becker, D. B. Milošević, A. Sanpera, and M. Lewenstein, "Feynman's Path-Integral Approach for Intense-Laser-Atom Interactions," *Science* 292, 902 (2001).

Bibliography

- [53] A. D. Shiner, B. E. Schmidt, C. Trallero-Herrero, H. J. Wörner, S. Patchkovskii, P. B. Corkum, J.-C. Kieffer, F. Légaré, and D. M. Villeneuve, “Probing collective multi-electron dynamics in xenon with high-harmonic spectroscopy,” *Nature Physics* 7, 464 (2011).
- [54] S. Pabst, L. Greenman, D. A. Mazziotti, and R. Santra, “Impact of multichannel and multipole effects on the Cooper minimum in the high-order-harmonic spectrum of argon,” *Phys. Rev. A* 85, 023411 (2012).
- [55] S. Sukiasyan, S. Patchkovskii, O. Smirnova, T. Brabec, and M. Y. Ivanov, “Exchange and polarization effect in high-order harmonic imaging of molecular structures,” *Phys. Rev. A* 82, 043414 (2010).
- [56] D. A. Telnov and S.-I. Chu, “Effects of multiple electronic shells on strong-field multiphoton ionization and high-order harmonic generation of diatomic molecules with arbitrary orientation: An all-electron time-dependent density-functional approach,” *Phys. Rev. A* 80, 043412 (2009).
- [57] Z. Zhao, J. Yuan, and T. Brabec, “Multielectron signatures in the polarization of high-order harmonic radiation,” *Phys. Rev. A* 76, 031404 (2007).
- [58] J. Heslar, D. Telnov, and S.-I. Chu, “High-order-harmonic generation in homonuclear and heteronuclear diatomic molecules: Exploration of multiple orbital contributions,” *Phys. Rev. A* 83, 043414 (2011).
- [59] M. F. Ciappina, C. C. Chirilă, and M. Lein, “Influence of Coulomb continuum wave functions in the description of high-order harmonic generation with H_2^+ ,” *Phys. Rev. A* 75, 043405 (2007).
- [60] P. Salières, A. Maquet, S. Haessler, J. Caillat, and R. Taïeb, “Imaging orbitals with attosecond and Ångström resol-

Bibliography

- utions: toward attochemistry?," *Reports on Progress in Physics* 75, 062401 (2012).
- [61] M. Y. Ivanov, T. Brabec, and N. Burnett, "Coulomb corrections and polarization effects in high-intensity high-harmonic emission," *Phys. Rev. A* 54, 742 (1996).
- [62] O. Smirnova, M. Spanner, and M. Ivanov, "Coulomb and polarization effects in sub-cycle dynamics of strong-field ionization," *Journal of Physics B: Atomic, Molecular and Optical Physics* 39, S307 (2006).
- [63] O. Smirnova, A. S. Mouritzen, S. Patchkovskii, and M. Y. Ivanov, "Coulomb-laser coupling in laser-assisted photoionization and molecular tomography," *Journal of Physics B: Atomic, Molecular and Optical Physics* 40, F197 (2007).
- [64] A.-T. Le, R. D. Picca, P. D. Fainstein, D. A. Telnov, M. Lein, and C. D. Lin, "Theory of high-order harmonic generation from molecules by intense laser pulses," *Journal of Physics B: Atomic, Molecular and Optical Physics* 41, 081002 (2008).
- [65] A.-T. Le, R. R. Lucchese, S. Tonzani, T. Morishita, and C. D. Lin, "Quantitative rescattering theory for high-order harmonic generation from molecules," *Phys. Rev. A* 80, 013401 (2009).
- [66] J. Higuette, H. Ruf, N. Thiré, R. Cireasa, E. Constant, E. Cormier, D. Descamps, E. Mével, S. Petit, B. Pons, Y. Mairesse, and B. Fabre, "High-order harmonic spectroscopy of the Cooper minimum in argon: Experimental and theoretical study," *Phys. Rev. A* 83, 053401 (2011).
- [67] J. Levesque, Y. Mairesse, N. Dudovich, H. Pépin, J.-C. Kieffer, P. B. Corkum, and D. M. Villeneuve, "Polarization State of High-Order Harmonic Emission from Aligned Molecules," *Phys. Rev. Lett.* 99, 243001 (2007).

Bibliography

- [68] X. Zhou, R. Lock, N. Wagner, W. Li, H. C. Kapteyn, and M. M. Murnane, “Elliptically Polarized High-Order Harmonic Emission from Molecules in Linearly Polarized Laser Fields,” *Phys. Rev. Lett.* 102, 073902 (2009).
- [69] M. Lein, N. Hay, R. Velotta, J. P. Marangos, and P. L. Knight, “Interference effects in high-order harmonic generation with molecules,” *Phys. Rev. A* 66, 023805 (2002).
- [70] M. Born and E. Wolf, *Principles of Optics: Electromagnetic Theory of Propagation, Interference and Diffraction of Light*, 7 ed. (Cambridge University Press, 1999).
- [71] H. J. Wörner, J. B. Bertrand, P. Hockett, P. B. Corkum, and D. M. Villeneuve, “Controlling the Interference of Multiple Molecular Orbitals in High-Harmonic Generation,” *Phys. Rev. Lett.* 104, 233904 (2010).
- [72] H. J. Wörner, H. Niikura, J. B. Bertrand, P. B. Corkum, and D. M. Villeneuve, “Observation of Electronic Structure Minima in High-Harmonic Generation,” *Phys. Rev. Lett.* 102, 103901 (2009).
- [73] S. Minemoto, T. Umegaki, Y. Oguchi, T. Morishita, A.-T. Le, S. Watanabe, and H. Sakai, “Retrieving photorecombination cross sections of atoms from high-order harmonic spectra,” *Phys. Rev. A* 78, 061402 (2008).
- [74] A. Etches, C. B. Madsen, and L. B. Madsen, “Inducing elliptically polarized high-order harmonics from aligned molecules with linearly polarized femtosecond pulses,” *Phys. Rev. A* 81, 013409 (2010).
- [75] S. Odžak and D. B. Milošević, “Ellipticity and the offset angle of high harmonics generated by homonuclear diatomic molecules,” *Journal of Physics B: Atomic, Molecular and Optical Physics* 44, 125602 (2011).

Bibliography

- [76] S. Odžak and D. B. Milošević, “Interference effects in high-order harmonic generation by homonuclear diatomic molecules,” *Phys. Rev. A* 79, 023414 (2009).
- [77] S.-F. Zhao, C. Jin, A.-T. Le, T. F. Jiang, and C. D. Lin, “Analysis of angular dependence of strong-field tunneling ionization for CO₂,” *Phys. Rev. A* 80, 051402 (2009).
- [78] S.-F. Zhao, C. Jin, A.-T. Le, and C. D. Lin, “Effect of an improved molecular potential on strong-field tunneling ionization of molecules,” *Phys. Rev. A* 82, 035402 (2010).
- [79] A.-T. Le, R. R. Lucchese, and C. D. Lin, “Polarization and ellipticity of high-order harmonics from aligned molecules generated by linearly polarized intense laser pulses,” *Phys. Rev. A* 82, 023814 (2010).
- [80] A.-T. Le and C. Lin, “Polarisation states of high harmonic generation from aligned molecules,” *Journal of Modern Optics* 58, 1158 (2011).
- [81] P. Antoine, B. Piraux, and A. Maquet, “Time profile of harmonics generated by a single atom in a strong electromagnetic field,” *Phys. Rev. A* 51, R1750 (1995).
- [82] O. E. Alon, V. Averbukh, and N. Moiseyev, “Selection Rules for the High Harmonic Generation Spectra,” *Phys. Rev. Lett.* 80, 3743 (1998).
- [83] D. Dimitrovski, C. P. J. Martiny, and L. B. Madsen, “Strong-field ionization of polar molecules: Stark-shift-corrected strong-field approximation,” *Phys. Rev. A* 82, 053404 (2010).
- [84] M. Abu-samha and L. B. Madsen, “Photoelectron angular distributions from polar molecules probed by intense femtosecond lasers,” *Phys. Rev. A* 82, 043413 (2010).

Bibliography

- [85] H. Li, D. Ray, S. De, I. Znakovskaya, W. Cao, G. Laurent, Z. Wang, M. F. Kling, A. T. Le, and C. L. Cocke, "Orientation dependence of the ionization of CO and NO in an intense femtosecond two-color laser field," *Phys. Rev. A* 84, 043429 (2011).
- [86] J. Wu, L. P. H. Schmidt, M. Kunitski, M. Meckel, S. Voss, H. Sann, H. Kim, T. Jahnke, A. Czasch, and R. Dörner, "Multiorbital Tunneling Ionization of the CO Molecule," *Phys. Rev. Lett.* 108, 183001 (2012).
- [87] E. Hasović, M. Busuladžić, W. Becker, and D. B. Milošević, "Dressed-bound-state molecular strong-field approximation: Application to above-threshold ionization of heteronuclear diatomic molecules," *Phys. Rev. A* 84, 063418 (2011).
- [88] A. Etches, M. B. Gaarde, and L. B. Madsen, "Laser-induced bound-state phases in high-order harmonic generation," *submitted* (2012).
- [89] J. Itatani, J. Levesque, D. Zeidler, H. Niikura, H. Pépin, J. Kieffer, P. Corkum, and D. Villeneuve, "Tomographic imaging of molecular orbitals," *Nature* 432, 867 (2004).
- [90] S. Haessler *et al.*, "Attosecond imaging of molecular electronic wavepackets," *Nature Physics* 6, 200 (2010).
- [91] C. Vozzi, M. Negro, F. Calegari, G. Sansone, M. Nisoli, S. De Silvestri, and S. Stagira, "Generalized molecular orbital tomography," *Nature Physics* 7, 822 (2011).
- [92] A. Etches, M. B. Gaarde, and L. B. Madsen, "Two-center minima in harmonic spectra from aligned polar molecules," *Phys. Rev. A* 84, 023418 (2011).
- [93] P. M. Paul, E. S. Toma, P. Breger, G. Mullot, F. Augé, P. Balcou, H. G. Muller, and P. Agostini, "Observation of

Bibliography

- a Train of Attosecond Pulses from High Harmonic Generation,” *Science* 292, 1689 (2001).
- [94] Y. Mairesse, A. de Bohan, L. J. Frasinski, H. Merdji, L. C. Dinu, P. Monchicourt, P. Breger, M. Kovačev, R. Taïeb, B. Carré, H. G. Muller, P. Agostini, and P. Salières, “Attosecond Synchronization of High-Harmonic Soft X-rays,” *Science* 302, 1540 (2003).
- [95] N. Wagner, X. Zhou, R. Lock, W. Li, A. Wüest, M. Murnane, and H. Kapteyn, “Extracting the phase of high-order harmonic emission from a molecule using transient alignment in mixed samples,” *Phys. Rev. A* 76, 061403 (2007).
- [96] B. K. McFarland, J. P. Farrell, P. H. Bucksbaum, and M. Gühr, “High-order harmonic phase in molecular nitrogen,” *Phys. Rev. A* 80, 033412 (2009).
- [97] M. Lein, N. Hay, R. Velotta, J. P. Marangos, and P. L. Knight, “Role of the Intramolecular Phase in High-Harmonic Generation,” *Phys. Rev. Lett.* 88, 183903 (2002).
- [98] O. Smirnova, S. Patchkovskii, Y. Mairesse, N. Dudovich, D. Villeneuve, P. Corkum, and M. Y. Ivanov, “Attosecond Circular Dichroism Spectroscopy of Polyatomic Molecules,” *Phys. Rev. Lett.* 102, 063601 (2009).
- [99] S. Odžak and D. B. Milošević, “Molecular high-order harmonic generation: analysis of a destructive interference condition,” *Journal of Physics B: Atomic, Molecular and Optical Physics* 42, 071001 (2009).
- [100] B. B. Augstein and C. F. de Morisson Faria, “Influence of asymmetry and nodal structures on high-harmonic generation in heteronuclear molecules,” *Journal of Physics B: Atomic, Molecular and Optical Physics* 44, 055601 (2011).

Bibliography

- [101] T. Kanai, S. Minemoto, and H. Sakai, “Ellipticity Dependence of High-Order Harmonic Generation from Aligned Molecules,” *Phys. Rev. Lett.* 98, 053002 (2007).
- [102] M. Busuladžić, A. Gazibegović-Busuladžić, D. B. Milošević, and W. Becker, “Angle-Resolved High-Order Above-Threshold Ionization of a Molecule: Sensitive Tool for Molecular Characterization,” *Phys. Rev. Lett.* 100, 203003 (2008).
- [103] M. Busuladžić, A. Gazibegović-Busuladžić, D. Milošević, and W. Becker, “Strong-field approximation for ionization of a diatomic molecule by a strong laser field. II. The role of electron rescattering off the molecular centers,” *Phys. Rev. A* 78, 033412 (2008).
- [104] M. Okunishi, R. Itaya, K. Shimada, G. Prümper, K. Ueda, M. Busuladžić, A. Gazibegović-Busuladžić, D. B. Milošević, and W. Becker, “Two-Source Double-Slit Interference in Angle-Resolved High-Energy Above-Threshold Ionization Spectra of Diatoms,” *Phys. Rev. Lett.* 103, 043001 (2009).
- [105] X. Zhu, Q. Zhang, W. Hong, P. Lan, and P. Lu, “Two-center interference in high-order harmonic generation from heteronuclear diatomic molecules,” *Opt. Express* 19, 436 (2011).
- [106] C. F. d. M. Faria, “High-order harmonic generation in diatomic molecules: A quantum-orbit analysis of the interference patterns,” *Phys. Rev. A* 76, 043407 (2007).
- [107] P. von den Hoff, I. Znakovskaya, S. Zherebtsov, M. Kling, and R. de Vivie-Riedle, “Effects of multi orbital contributions in the angular-dependent ionization of molecules in intense few-cycle laser pulses,” *Applied Physics B: Lasers and Optics* 98, 659 (2010).

Bibliography

- [108] X. M. Tong, Z. X. Zhao, and C. D. Lin, “Theory of molecular tunneling ionization,” *Phys. Rev. A* 66, 033402 (2002).
- [109] C. Jin, A.-T. Le, and C. D. Lin, “Analysis of effects of macroscopic propagation and multiple molecular orbitals on the minimum in high-order harmonic generation of aligned CO₂,” *Phys. Rev. A* 83, 053409 (2011).
- [110] S.-F. Zhao, C. Jin, R. R. Lucchese, A.-T. Le, and C. D. Lin, “High-order-harmonic generation using gas-phase H₂O molecules,” *Phys. Rev. A* 83, 033409 (2011).
- [111] C. Jin, A.-T. Le, and C. D. Lin, “Medium propagation effects in high-order harmonic generation of Ar and N₂,” *Phys. Rev. A* 83, 023411 (2011).
- [112] C. Jin, A.-T. Le, and C. D. Lin, “Retrieval of target photorecombination cross sections from high-order harmonics generated in a macroscopic medium,” *Phys. Rev. A* 79, 053413 (2009).
- [113] M. A. Lysaght, L. R. Moore, L. A. A. Nikolopoulos, J. S. Parker, H. W. Hart, and K. T. Taylor, “*Ab Initio* Methods for Few- and Many-Electron Atomic Systems in Intense Short-Pulse Laser Light,” in *Quantum Dynamic Imaging*, edited by A. D. Bandrauk and M. Ivanov CRM Series in Mathematical Physics p. 107 Springer New York 2011.
- [114] A. Scrinzi, “Infinite-range exterior complex scaling as a perfect absorber in time-dependent problems,” *Phys. Rev. A* 81, 053845 (2010).
- [115] L. Tao and A. Scrinzi, “Photo-electron momentum spectra from minimal volumes: the time-dependent surface flux method,” *New Journal of Physics* 14, 013021 (2012).
- [116] G. Engel, T. Calhoun, E. Read, T. Ahn, T. Mančal, Y. Cheng, R. Blankenship, and G. Fleming, “Evidence

Bibliography

- for wavelike energy transfer through quantum coherence in photosynthetic systems,” *Nature* 446, 782 (2007).
- [117] W. C. Henneberger, “Perturbation Method for Atoms in Intense Light Beams,” *Phys. Rev. Lett.* 21, 838 (1968).
- [118] F. Morales, M. Richter, S. Patchkovskii, and O. Smirnova, “Imaging the Kramers-Henneberger atom,” *Proceedings of the National Academy of Sciences* 108, 16906 (2011).

English summary

When a molecule is submitted to a very intense laser pulse it emits coherent bursts of light in each optical half-cycle of the laser field. This process is known as high-order harmonic generation because the spectrum consists of many peaks at energies corresponding to an integer amount of laser photons. The harmonics contain information about the wave function of the loosest bound electron on an Ångström length scale and attosecond time scale. However, accurate theoretical models are needed in order to extract this information. In this thesis the most widely used model of high-order harmonic generation is extended to polar molecules by including the laser-induced Stark shift of each molecular orbitals. The Stark shift is shown to have a major influence on the relative strength of harmonic bursts in neighbouring half-cycles, as well as leaving an imprint on the phase of the harmonics. Surprisingly, the dominating first-order Stark phase turns out to be nearly independent of the laser intensity.

Dansk resumé

Når et molekyle udsættes for en meget intens laserpuls, udsender den kohærente lysglimt i hver af laserens optiske halvcykler. Denne proces går under navnet høj harmonisk generation, fordi spektret består af en lang række af toppe ved energier, der svarer til et helt antal laserfotoner. Høj harmonisk stråling indeholder information om den løsest bundne elektrons bølgefunktion på en Ångström længdeskala, og attosekund tidsskala. For at afkode denne information er det nødvendigt med detaljerede teoretiske modeller. I denne afhandling udvides den mest anvendte model af høj harmonisk generation til polære molekyler ved at inkorporere de molekylære orbitalers laserinducerede Stark-skift. Stark-skiftet viser sig både at have en stor indflydelse på den relative styrke af lysglimtene, samt fasen af de individuelle harmoniske. Overraskende nok er den dominerende førsteordens Stark-fase næsten uafhængig af laserintensiteten.
